Beslier, M.-O., Whitmarsh, R.B., Wallace, P.J., and Girardeau, J. (Eds.)
Proceedings of the Ocean Drilling Program, Scientific Results Volume 173

11. Magnetostratigraphy and Biostratigraphy of Cenozoic Sediments Recovered from the Iberia Abyssal Plain[1]

Xixi Zhao,[2] Bryan C. Ladner,[3] Kristeen Roessig,[3]
Sherwood W. Wise Jr.,[3] and Elspeth Urquhart[4]

ABSTRACT

We have conducted an integrated paleomagnetic and biostratigraphic study on the Cenozoic sedimentary sequences of the southern Iberia Abyssal Plain margin, focusing on Ocean Drilling Program (ODP) Sites 897, 898, 900, 1067, 1068, and 1069. Reliable magnetostratigraphy from these six sites is presented in this paper. Sedimentary sections from Holes 897C, 898A, 900A, 1067A, 1068A, and 1069A have recorded a pattern of magnetic polarity reversals that correlates well with the known magnetic polarity timescale for the past 56 m.y. The polarity patterns from the Pliocene–Pleistocene turbidite sequence at the Leg 149 sites show that a reliable magnetostratigraphy can be established from the early Pliocene to Holocene, including the Gilbert/Gauss boundary (3.58 m.y.) through the Matuyama/Brunhes boundary (0.78 m.y.). On the basis of distinct intervals of magnetic reversal zones and biostratigraphic datums, five magnetozones (C21n–C25n) can be recognized at the three Leg 173 sites that range from middle Eocene to late Paleocene in age. The magnetostratigraphy of the Iberia sections allows the determination of sedimentation rates and better constraints on the timing of deformation. Combining the age and average inclination information available from the magnetostratigraphy, we also present paleolatitudes vs. time for the Iberia drill sites.

[1]Zhao, X., Ladner, B.C., Roessig, K., Wise, S.W., Jr., and Urquhart, E., 2001. Magnetostratigraphy and biostratigraphy of Cenozoic sediments recovered from the Iberia Abyssal Plain. *In* Beslier, M.-O., Whitmarsh, R.B., Wallace, P.J., and Girardeau, J. (Eds.), *Proc. ODP, Sci. Results*, 173, 1–73 [Online]. Available from World Wide Web: <http://www-odp.tamu.edu/publications/173_SR/VOLUME/CHAPTERS/SR173_11.PDF>. [Cited YYYY-MM-DD]
[2]Institute of Tectonics, University of California, Santa Cruz, Santa Cruz CA 95064, USA. **xzhao@es.ucsc.edu**
[3]Department of Geology, Florida State University, Tallahassee FL 32306, USA.
[4]Department of Geological Sciences, University College London, Gower Street, London WC1E 6BT, United Kingdom.

Initial receipt: 19 May 2000
Acceptance: 3 May 2001
Web publication: 18 July 2001
Ms 173SR-016

INTRODUCTION

Deep-sea basins are one of the least-known sedimentary environments, despite covering a little less than one-quarter of the Earth's surface (McKenzie, 1978). Abyssal plains within the deep ocean basins are important because they may provide records of major tectonic events in the erosional and depositional history of a continental margin. The use of deep-sea drilling techniques to investigate the geological evolution of the ocean basins and their margins depends critically on an accurate knowledge of the geological ages of the sediments encountered. Without such knowledge, comparisons of contemporaneous paleoenvironments in different regions cannot be made, and the recognition of important geological and tectonic events, represented by such features as angular unconformities, sedimentary hiatuses, and changes in sedimentation rates, becomes impossible. Biostratigraphy and magnetostratigraphy are two principal techniques for chronostratigraphic analysis of long continuous sedimentary sequences. Among them, biostratigraphy is the most widely used technique for determining the relative ages of deep-sea sediments, and its contribution to our current understanding of the geological evolution of ocean basins cannot be overemphasized. However, this technique does suffer certain limitations. In particular, it requires the presence of suitable conditions for the existence and preservation of ancient marine organisms and time resolution depends upon the identification of particular assemblages of rapidly evolving species. Marine biostratigraphic zonations generally use first and last appearance datums of planktonic microfossils for subdividing geologic time and correlating sedimentary sections, but the relative abundance of the datums is often complicated by geographic and environmental factors or masked in the sedimentary record by dissolution effects. This can lead to local difficulties in identifying boundaries of biostratigraphic zones and in ascribing a precise synchroneity to chronostratigraphic horizons.

Geomagnetic polarity transitions, on the other hand, are the most frequent, best-dated, and globally synchronous geophysical phenomena. Magnetostratigraphy is a tool of great promise for precise temporal correlation and accurate dating in sediments. It is based on the fact that the Earth's magnetic field has occasionally reversed polarity and that many sedimentary rocks retain a magnetic imprint of the field at the time they were deposited. Because the length of time for the geomagnetic field to flip from one polarity state to the other is only a few thousand years, the boundaries between magnetozones (stratigraphic zones of single polarity) in sections of magnetized rocks are extremely sharp, much sharper than between typical biostratigraphic zones. Moreover, because the entire field of the Earth reverses within this geologically short time, magnetozones are essentially synchronous all over the globe. Finally, because the time between successive reversals is a random variable following very nearly a Poisson distribution (Merrill et al., 1996), the pattern of thicknesses of several magnetozones in each part of a steadily deposited section is a distinctive fingerprint (analogous to the zebra-stripe bar codes used in libraries and supermarkets) that can be correlated between distant sections and matched to the established geomagnetic polarity timescale (GPTS). This scale, which has been established independently by radiometric dating and refined by cross-checking among multiple records, provides dates for reversals that occurred during the last 150 m.y. of the Earth's history (e.g., Harland et

al., 1990; Cande and Kent, 1992, 1995; Channell et al., 1995; Berggren et al., 1995). Today, a fairly well-resolved magnetic polarity sequence has been extended back to 300 Ma. (Opdyke and Channell, 1996). Although magnetostratigraphic dating offers certain important advantages over micropaleontological dating, it is itself subject to other limitations. For example, it is first necessary to demonstrate that the remanent magnetization of the sediment is a stable primary magnetization acquired at or close to the time of deposition. Second, the pattern of magnetic reversals recorded in a particular sedimentary sequence depends on both the reversal frequencies at the time of deposition and on the sedimentation rate. In the case of slow sedimentation rates at times of high reversal frequency, certain magnetic polarity events may be too short in duration to be recorded at all and the occurrence of sedimentary hiatuses will considerably complicate the identification of particular magnetic polarity intervals. However, if the approximate age of the sediment is known from biostratigraphic information, it should be possible to focus on a particular part of the established polarity timescale and thus to identify specific reversals in the sedimentary sequence. The combination of magnetic and biostratigraphic studies may then allow much more precise dating than from paleontological information alone.

The Ocean Drilling Program (ODP) and its predecessor, the Deep Sea Drilling Project (DSDP), have provided a quantum leap in our understanding of marine geology and key information about the processes that have been operating on the deep-sea basins of the world. The general pattern of geomagnetic field polarity reversal during the Cenozoic and late Mesozoic, largely resulting from the past 15 yr of the ODP, is now well documented (Cande and Kent, 1995). However, the precise correlation between the GPTS and biostratigraphic zonations is still incompletely established. The only completely satisfactory means of achieving such a correlation is to undertake combined paleomagnetic and biostratigraphic studies on the same sedimentary sequences. The purpose of this synthesis is to present the results of such work, conducted on sedimentary cores drilled at ODP Legs 149 and 173 sites from the Iberia Abyssal Plain, off the west coast of Portugal. Postcruise research has included magnetostratigraphic, biostratigraphic, and sedimentologic analyses of samples taken from these cores (de Kaenel and Villa, 1996; Gervais, 1996; Liu, 1996; Liu et al., 1996; Milkert et al., 1996; Zhao et al., 1996, **Chap. 8,** this volume; Ladner and Wise, **Chap. 5,** this volume; McGonigal and Wise, **Chap. 4,** this volume). We first summarize and discuss the paleomagnetic polarity patterns of the sediments recovered from Sites 897, 898, and 900 of Leg 149 and Sites 1067, 1068, and 1069 of Leg 173, focusing on the portions that provided the most readily interpretable data. We subsequently consolidate and expand the preliminary interpretations of the polarity sequence, based on the conjunction of the lithostratigraphy and biostratigraphy and the geomagnetic polarity timescale of Cande and Kent (1995), and present a revised magnetostratigraphy for these sites. We then use the magnetostratigraphy to estimate the sedimentation rates and the times at which significant changes in these rates occurred. Finally, we estimate paleolatitudes at which the sediments were deposited using the age and average inclination information available from the magnetostratigraphy. Such information is important in evaluating the recent geological evolution of the Iberia Abyssal Plain.

BACKGROUND INFORMATION AND SITE SETTING

The Iberia Abyssal Plain, which lies between 39°N and 41°N, has an unusually wide ocean–continent transition zone (OCT) (up to 130 km) and a 300-km-long narrow margin-parallel peridotite ridge. In 1993, ODP Leg 149 drilled a west-to-east transect of five sites in the OCT west of Portugal. Leg 173 is a sequel to Leg 149, during which a total of five sites were drilled in 1997 (Fig. F1). The main results of Leg 149 and Leg 173 suggest that the basement in the OCT of the southern Iberia Abyssal Plain is made of peridotites over an east-west width of at least 95 km. Results from Leg 173 further suggest that the mantle rocks were unroofed in the continental breakup zone very close to the landward edge of the OCT and that the zone of mantle exposure in the OCT between the continental crust and the true oceanic crust is even more widespread than previously thought (Whitmarsh, Beslier, Wallace, et al., 1998). Because the major target of Leg 173 was the structural basement of the OCT, only ~150 m of sediments above the basement was cored during Leg 173. However, the sediments recovered during Leg 173 represent an opportunity to extend, for the first time, the direct correlation of the biostratigraphic and magnetostratigraphic timescales from the Pliocene into the Eocene and Paleocene, complementing the magnetostratigraphic results from Leg 149 sites.

The tectonic history of the Iberia Abyssal Plain and the six site locations (Fig. F2) that are relevant to this paper are documented in detail in appropriate papers and the Legs 149 and 173 site report chapters (see Sawyer, Whitmarsh, Klaus, et al., 1994, and Whitmarsh, Beslier, Wallace, et al., 1998, for Legs 149 and 173 sites, respectively). Thus, they will be only briefly summarized here. Site 897 is situated over a north-south basement ridge, which had been linked to a peridotite ridge drilled west of Galicia Bank 140 km to the north (Fig. F1). Cores were obtained from three holes, which penetrated up to 694 m of Pleistocene to Lower Cretaceous sediments (Fig. F2). At Site 898, situated over an elongate basement high, cores were obtained from a single hole that penetrated 342 m of Pleistocene to upper Oligocene sediments. Site 900 was situated over the crest of a north-south-trending basement high that was expected to be part of the Iberia continental crust thinned during Early Cretaceous rifting. Drilling and coring at this site recovered 749 m of Paleocene to Pleistocene contourites, turbidites, and pelagic/hemipelagic sediments (Fig. F2). Site 1067 lies near the northern edge of the southern Iberia Abyssal Plain. A total of 115.8 m of middle Eocene to Paleocene sediments was drilled before basement rocks were encountered. The cored interval is very similar to sediments of the same age recovered at Site 900, some 800 m to the west. Site 1068 is located on the west flank of the same north-south-trending basement high as Sites 1067 and 900. A 139-m-thick sedimentary succession was cored in Hole 1068A, which ranges in age from middle Eocene to Maastrichtian. Two lithostratigraphic subunits are recognized, both of which show gentle tilting (~5°). Site 1069 is situated in a relatively flat-topped north-south basement ridge. Seismic data suggest that the basement is a possible continental fault block titled toward the continent. A 147-m-thick sedimentary succession was cored at Site 1069, whose age ranges from the middle Eocene to late Campanian. At the latter three sites, calcareous microfossils are common and generally well preserved. Planktonic fora-

F1. Bathymetric chart of the western Iberia margin, p. 27.

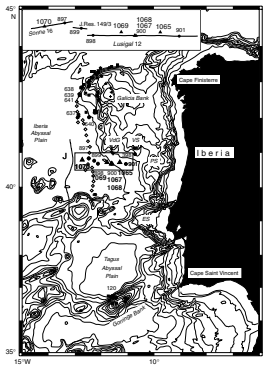

F2. Summaries of stratigraphic successions, Legs 149 and 173, p. 28.

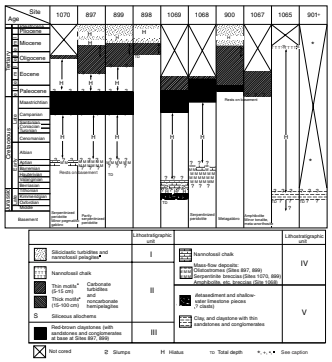

minifers are variable in preservation and abundance but are generally consistent with ages determined using calcareous nannofossils.

A major characteristic of the seismic reflection profiles obtained off much of western Iberia is an angular unconformity caused by onlap of mainly Pliocene–Pleistocene turbidites onto gently folded middle Miocene and older strata. The folding is the result of a northwest-southeast compressional phase in the Betic Mountains of southern Spain (Maufret et al., 1989). This regional unconformity was recognized at all sites and dated as middle Miocene based on preliminary biostratigraphic data. The end of the hiatus was more variable and probably depended on the amount of uplift at each site (Shipboard Scientific Party, 1994a, 1994b, 1994c). A regional stratigraphic marker bed was also recognized in three drilled sites of Leg 173 (Shipboard Scientific Party, 1998a, 1998b, 1998c) and one site (Site 900) of Leg 149 (Shipboard Scientific Party, 1994c) and was tentatively dated as early Eocene in age biostratigraphically. This bed appears to be synchronous at these sites and thus provides a proxy stratigraphic marker for correlation between the sedimentary records of the OCT zone in the southern Iberia Abyssal Plain and the Cenozoic stratigraphic framework.

LABORATORY AND ANALYTICAL METHODS

Paleomagnetic Sampling

During Legs 149 and 173, >1600 discrete paleomagnetic samples were taken for shipboard and shore-based magnetostratigraphic and rock magnetic studies. In the case of soft unconsolidated sediments, paleomagnetic samples were taken by pushing nonmagnetic cubes into the split working halves. In order to reduce the deformation/disturbance of the sediment, the core was carefully cut using a thin stainless steel spatula before pressing the plastic sampling boxes into the sediment. In lithified sediments, 2.5-cm cylindrical samples were drilled from the core sections using a water-cooled nonmagnetic drill bit attached to the standard drill press or cube-shaped samples were cut by diamond saw. In all cases, the uphole direction was carefully recorded on the sample by means of an orientation arrow before removal from the core section and only sediments showing no visible signs of deformation were sampled. All samples were kept in a relatively cold temperature and low-field environment to inhibit water loss and prevent viscous remanence acquisition.

Magnetic Measurement Procedure

Magnetic directions at these sites were obtained by both shipboard pass-through cryogenic magnetometer measurement and onshore progressive alternating-field (AF) and thermal demagnetization experiments on >1500 discrete samples. The paleomagnetic data presented in this paper are of two different types: those obtained using the shipboard pass-through cryogenic magnetometer and those derived from onshore analysis of discrete samples. In the shipboard pass-through system, magnetic measurements were performed by passing continuous archive-half core sections through a 2G cryogenic magnetometer and were taken at intervals of either 5 or 10 cm along the core and after AF demagnetization at 10 and 15 mT. Magnetic measurements of discrete samples in shore-based studies were performed with a 2G cryogenic

magnetometer housed in a field-free room of the paleomagnetic laboratory at the University of California at Santa Cruz (UCSC). Both standard thermal and AF demagnetization experiments were done to evaluate the directional stability and coercivity/unblocking temperature spectra of each sample. Bulk magnetic susceptibility was also measured after every demagnetization step to detect whether chemical changes were affecting the magnetization during progressive heating. Magnetization directions were determined by principal component analysis (Kirschvink, 1980), the distribution of paleomagnetic directions at each site was calculated using Fisher (1953) statistics, and site mean directions of all demagnetized data were derived by giving unit weight to each mean sample direction. A few representative samples were also selected for a set of rock magnetic measurements to examine their mineralogical characteristics. These rock magnetic measurements were performed at the Institute for Rock Magnetism, University of Minnesota, and include (1) high-field (1 T) Curie temperature determinations, (2) low-temperature (10 K) cycling of saturation isothermal remanent magnetization, and (3) measurement of hysteresis loop parameters.

Because of the rotary technique used for drilling both Legs 149 and 173 cores, relative rotation frequently occurs between different segments of sediment within the core. This may cause apparent changes in the declination of stable remanent magnetization. Consequently, in this study the magnetic polarity has been assigned on the basis of the inclination of the stable remanent magnetization alone. Because all sites are situated at moderate latitudes in the Northern Hemisphere, positive (downward directed) inclinations are taken to signify a normal polarity and negative (upward directed) inclination signifies reversed polarity. In this study, we adhere to the chronostratigraphic nomenclature and geochronology of Cande and Kent (1995) as the GPTS. We correlate polarity zones with the GPTS in the manner that appears most consistent with both magnetic and biostratigraphic data. In naming the various polarity intervals, we use the familiar proper names for the Pliocene–Pleistocene magnetic chrons (Brunhes, Matuyama, Gauss, and Gilbert) and subchrons (e.g., Jaramillo and Olduvai).

PALEOMAGNETIC AND ROCK MAGNETIC RESULTS

General View

Continuous and undisturbed Cenozoic sequences of cores of sufficient length to allow the identification of geologically useful magnetic polarity sequences were obtained from Sites 897, 898, 900, 1067, 1068, and 1069. Within the six sites where a magnetostratigraphy can be constructed there are considerable variations in demagnetization behavior among the various lithologies, but the most common features can be summarized as follows. A pervasive remagnetization imparted by the coring process is commonly encountered, as noted during previous legs (e.g., Ade-Hall and Johnson, 1976; Gee et al., 1989; Zhao et al., 1994). This remagnetization is characterized by natural remanent magnetization (NRM) inclinations that are strongly biased toward vertical values (+90°) in many cores. This remagnetization most severely affected the external portions of the cores (presumably because the outside of the core is physically closer to the magnetized core barrel). When present, this drilling-induced component generally shows a steep downward di-

rection and can be removed at initial stages of demagnetization. As shown in Figure F3, the NRM inclinations observed from Section 149-897C-61R-1 are biased toward steep positive values, indicating the presence of drilling-induced remagnetization. Upon demagnetization to 15 mT, a shift toward a negative inclination and a significant decrease in intensity were observed. The reversed polarity of magnetization was also confirmed by progressive AF demagnetization on three discrete samples from this section (squares in Fig. F3). Because the maximum level of AF demagnetization on the ship's cryogenic magnetometer was not always able to remove these overprints, the pass-through measurements generally show a more intense remagnetization than do discrete sample measurements. Therefore, the majority of the paleomagnetic results presented in this paper were obtained from extensive shore-based measurements on discrete samples carried out in the "field-free" paleomagnetic laboratory at UCSC.

Whenever possible, demagnetization was continued until an unambiguous and reliable determination of polarity of the stable component of magnetization had been achieved. Figure F4 illustrates the stability behavior of several samples from nannofossil clay and ooze. Sample 149-900A-14R-1, 15–17 cm (Fig. F4A), demonstrates the removal of a normal component of magnetization close to the present geomagnetic field inclination and the isolation of a more stable reversed component that is univectorially decaying toward the origin of the vector plots (Zijderveld, 1967). Sample 149-900A-10R-2, 35–37 cm (Fig. F4B), on the other hand, shows a reversed secondary component before isolating the more stable normal polarity of the characteristic remanent magnetization (ChRM). An example of demagnetization behavior of a sample during thermal demagnetization is also illustrated in Figure F4C. A secondary component of magnetization was removed at low temperatures (300°C), and the ChRM component having higher unblocking temperatures could be identified. These demagnetization behaviors are typical of the majority of samples from all six sites. Demagnetization of discrete samples sometimes also showed antipodal relative declinations within the same physically continuous piece of core section. An example is given by two samples from Core 149-900A-10R (Fig. F5). After demagnetization at 40 mT, the reversal indicated by the difference in polarity of inclination is confirmed by the near 180° change in declination. This positive "antipodal test" is perhaps the most compelling argument for isolating the primary ChRM, although this test is not sufficient by itself. The inclination values of ChRM are moderate downward or upward, which are consistent with the expected inclinations for these sites. This information may imply that the ChRM of these sediments are free of a secondary component of magnetization and represent the primary magnetization when these sediments were deposited.

The response of the ChRM to AF and thermal demagnetization suggests that the ChRM in most samples is carried by fine (i.e., single domain to pseudo-single domain) low-Ti titanomagnetite grains. For some red-brown claystone samples, the fact that the magnetization persists to temperature treatments of up to 650°C indicates that hematite is most probably the carrier of the ChRM. We conducted several rock magnetic analyses on representative samples to further characterize the magnetic minerals and understand their rock magnetic properties. Hysteresis loops generated for representative red-brown claystone samples display "wasp-waisted" behaviors (Fig. F6). Wasp-waistedness is considered indicative of a bimodal distribution of grains with contrasting coercivity (Jackson, 1990; Roberts et al., 1995; Tauxe et al., 1996). Curie tempera-

F3. Remanent magnetization before and after 15-mT AF demagnetization, p. 29.

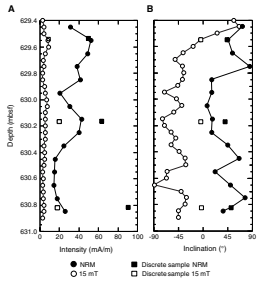

F4. Vector end point diagrams of demagnetization for nannofossil clay and nannofossil ooze, p. 30.

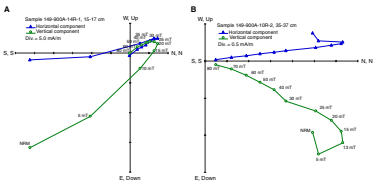

F5. Vector end point diagrams of demagnetization for samples from Core 149-900A-10R, p. 32.

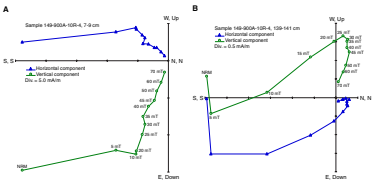

F6. Hysteresis loop for samples showing hematite, p. 33.

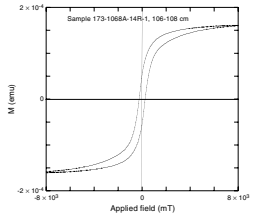

ture determinations, acquisition of isothermal remanent magnetization (IRM) and backfield demagnetization of saturation IRM, hysteresis loop parameters, and low-temperature demagnetization of these representative samples all corroborate the demagnetization behavior. It is worth pointing out that although the shipboard AF demagnetization of sediments at both Legs 149 and 173 sites revealed initial polarity patterns, it was only the subsequent shore-based thermal and detailed AF demagnetization that was able to resolve a high-coercivity/unblocking temperature component, which improved the quality of the magnetostratigraphy.

Site 897 (Hole 897C)

Sampling and Stability Tests

A total of 330 oriented paleomagnetic samples (6-cm³ plastic cubes or 10-cm³ minicores) were collected from Cenozoic sediments from this hole at a spacing of at least at one sample per 150-cm section. Each of these 330 samples was subjected to progressive AF or thermal demagnetization to verify the magnetostratigraphic results from the cryogenic magnetometer and to understand the magnetic behavior of the sediments during stepwise demagnetization. Figure F7 illustrates the response to AF demagnetization of two samples from nannofossil chalk oozes. High stability showed by the normally magnetized Sample 149-897C-4R-1, 34–36 cm (Fig. F7A), and reversely magnetized Sample 11R-6, 37–39 cm (Fig. F7B), is common in a high proportion of the samples from Hole 897C. These samples maintain an inclination close to the theoretically predicted value for the latitude of this site (59°), indicating that they may represent the primary ChRM.

F7. Vector end point diagrams of demagnetization, Site 897, p. 34.

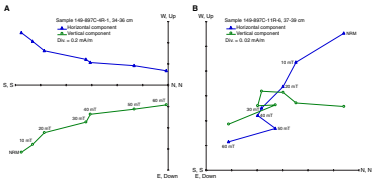

Magnetic Polarity Record for Hole 897C

As shown in Table T1 and Figure F8, a number of clearly defined magnetic reversals may be discerned on the basis of changes in sign of inclinations of the cores from Hole 897C. Without exception, each of the major polarity zones is defined by several samples of the same polarity. On the basis of micropaleontological studies, the uppermost 180 m of sediment at Site 897 is known to be of Pleistocene age (Liu et al., 1996; Gervais, 1996). Therefore, the normal polarity of Cores 1R through 7R suggests that these sediments were deposited during the Brunhes Chron (i.e., age <0.78 Ma), which agrees well with the biostratigraphic age markers (see Liu et al., 1996; Gervais, 1996). The first evidence for a reversed magnetization occurs at 118.93 meters below seafloor (mbsf) in Core 8R, which corresponds to the Brunhes/Matuyama Chron boundary (0.78 Ma) and biostratigraphic Subzone NN19h and Zone N23. Samples between 128.72 and 137.40 mbsf show normal polarity, indicating that the Jaramillo Subchron (0.99–1.07 Ma) was recorded in these samples. Biostratigraphic Subzone NN19f (0.88–1.07 Ma) is also placed in this depth interval. Below this depth, the dominantly reversed polarity correlates well with the Matuyama reversed polarity chron. This dominantly reversed polarity sequence extends to a depth of 292.8 mbsf. Biostratigraphic data suggest that sediments below a depth of 292.4 mbsf (Core 26R, 93–94 cm) may be of early Pliocene age. This information is in good agreement with paleomagnetic observations and suggests that the shift of polarity from reversed to normal at ~292 mbsf should correspond to the Matuyama/

T1. Magnetic stratigraphy, Site 897, p. 56.

F8. Magnetic inclination, inferred polarity, and biostratigraphic zones, Site 897, p. 35.

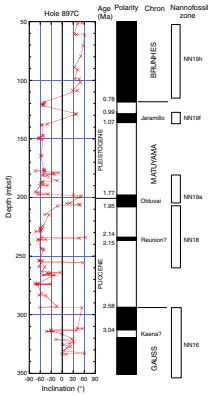

Gauss boundary (2.58 Ma). Within the sequence assigned to the Matuyama reversed chron, two apparently separate thin normal polarity zones are present in the depth ranges of 198.79–207.33 and 234.14–235.66 mbsf. The upper of these polarity zones is well defined on the basis of seven separate samples and appears to correspond well to the position of the Olduvai Subchron (1.77–1.95 Ma). Key nannofossil and planktonic foraminiferal markers around this depth also suggest that sediments span the Pliocene/Pleistocene boundary (NN19a and N22), which is in good agreement with the paleomagnetic data. The underlying thin normal polarity zone at 234.14 m is based on only two samples with high magnetic stability, but it is quite possible that they represent the short Reunion Subchron (2.14–2.15 Ma). Below the Matuyama/Gauss boundary, there is a dominantly normal polarity sequence, extending down at least to 333.95 mbsf (Table T1). This dominantly normal polarity sequence should correspond to the Gauss normal chron. Unfortunately, sediments below 333.95 mbsf are too weakly magnetized to be measured reliably. The NRM intensity is essentially of the same order as the noise level of the cryogenic magnetometer and the sample holder. Consequently, this weak magnetization prevents us from constructing a magnetostratigraphy below this depth.

The paleomagnetic and biostratigraphic datums are summarized in Table T2, and the main features of the magnetostratigraphic interpretation along with the inferred biostratigraphic zones at Site 897 are presented in Figure F8. It is clear from Table T2 and Figure F8 that the paleomagnetic and paleontological age determinations for the Pleistocene to lower Pliocene sequence at Hole 897C are compatible with each other, but the resolution of the paleomagnetic data is significantly greater. This allows a more precise determination of sedimentation rates and a better definition of the times at which significant changes in sedimentation rate occurred.

T2. Paleomagnetic and biostratigraphic datums, Site 897, p. 57.

Paleomagnetically Determined Sedimentation Rates for Hole 897C

The Pleistocene and Pliocene sediments cored at Hole 897C have yielded a detailed magnetic polarity stratigraphy (Fig. F8) from which relatively precise sedimentation rates can be calculated. The Brunhes/Matuyama (0.78 Ma), Jaramillo (0.99–1.07 Ma), Olduvai (1.77–1.95 Ma), and Matuyama/Gauss (2.58 Ma) Chrons are well determined at depths of 108.8, 128.7–137.4, 198.2–207.3, and 292.88 mbsf, respectively. One thin normal polarity zone at depth 234.1 mbsf is based on two samples but may possibly represent the Reunion Subchron (2.14–2.15 Ma). These calibration points allow the determination of relatively precise sedimentation accumulation rate values and the assignment of absolute ages to the biostratigraphic zonal boundaries identified in Hole 897C. The lower Pliocene to Holocene sediment accumulation rates at Site 897 exhibit alternating high and low rates. Sedimentation rates for the late Pliocene (50.7 m/m.y.) and early Pleistocene (90.3 m/m.y.) show markedly reduced deposition compared to the relative high accumulation rates during the lower Pliocene interval (135.8 m/m.y.) and the upper Pleistocene to Holocene (152.4 m/m.y.). Based on the "correlation" shown in Figure F9, a mean sedimentation accumulation rate of 92.3 m/m.y. is derived for most of the Pleistocene–Pliocene. Furthermore, if the identification of the Olduvai Subchron is correct, a short hiatus or a decrease in accumulation rate is inferred within the interval 1.77–1.95 Ma. It is worth pointing out that it was the paleomag-

F9. Depth vs. age curve for Hole 897C, p. 36.

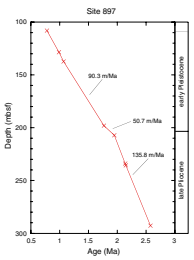

netic data that suggested the existence of a hiatus around the Pleistocene/Pliocene boundary, which could not have been identified from the available paleontological information alone.

Site 898 (Hole 898A)

Paleomagnetic Stability Tests and General Polarity Sequences for Site 898

At Site 898, multiple samples were taken from each 1.5-m core section recovered, yielding a total of 266 samples. As with Hole 897C, each sample was separately subjected to progressive AF demagnetization, although only 154 samples were used to determine the magnetostratigraphy (Table T3). In addition, the entire Section 12H-2 was specially chosen as a U-channel sample (105.70–107.20 mbsf in Table T3), which provides a unique opportunity to study a geomagnetic polarity transition in an abyssal plain setting.

The whole-core pass-through measurements from cores recovered with the advanced hydraulic piston corer at Site 898 were of high quality and agree well with the discrete sample data. The magnetic behavior for Cores 1H through 14H is very straightforward. After removal of a "soft" overprint component of magnetization, a well-established demagnetization stable end point is defined by a linear trend through the origin of the vector plot (Fig. F10). The stable components of remanent magnetization for Cores 1H through 3H are all of normal polarity. Biostratigraphic ages in these cores range from 0.3 to 0.8 Ma (see Sawyer, Whitmarsh, Klaus, et al., 1994, p. 122). Thus, in conjunction with the biostratigraphic data, we can assign these cores to the Brunhes Chron (<0.78 Ma).

The first evidence for a polarity reversal was found in Core 4H at a depth of 29.06 mbsf. This is shown by both discrete sample measurement and by the whole-core pass-through measurement with changes of ~180° in declination between normal and reversed intervals (see "Paleomagnetism" section in Shipboard Scientific Party, 1994b). Thus, this magnetic polarity shift (from normal to reversed) represents the Brunhes/Matuyama boundary (0.78 Ma). The next distinctive polarity shift (from reversed to normal) occurs in Core 11H at 101.74 mbsf and is well recorded in the U-channel sample from Section 12H-2 (see Table T3; Fig. F11). According to the sequence of magnetic polarity zones, this polarity shift may represent the onset of the Jaramillo Subchron (0.99–1.07 Ma). However, biostratigraphic data suggest that sediments below 95.75 mbsf may be of middle Pleistocene age (NN19d) (see Liu et al., 1996). This polarity shift should correspond to the Cobb Mountain Subchron at ~1.1 Ma (Mankinen et al., 1978; Mankinen and Grommé, 1982; Clement and Kent, 1987; Clement and Martinson, 1992; Spell and McDougall, 1992). As the age of the Cobb Mountain Subchron is estimated to be 1100 ± 20 ka (Mankinen and Grommé, 1982; Spell and McDougall, 1992), this information suggests that the sediment sequence between 101.74 and 106.44 mbsf was deposited at <30 ka. This would imply an abruptly high sedimentation rate (157 m/m.y.) during this interval compared to those for the rest of the Pleistocene. In view of this apparently anomalous sedimentation rate, (which is not observed in other Leg 149 sites) and the fact that the age difference between the Jaramillo and Cobb Mountain Subchron is very small (0.02 m.y.), we prefer to adhere to the sequence of magnetic polarity zones and correlate this polarity change with the Jaramillo Subchron.

T3. Magnetic stratigraphy, Site 898, p. 58.

F10. Vector end point diagrams of demagnetization, Site 898, p. 37.

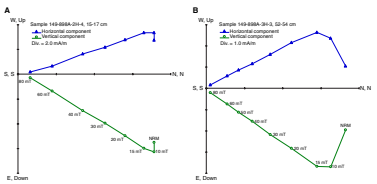

F11. Magnetic inclination, inferred polarity, and biostratigraphic zones, Site 898, p. 39.

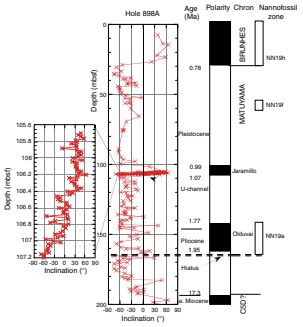

Between 106.46 and 163.18 mbsf, progressive demagnetization revealed only reversed magnetization from cores recovered in this interval except for a very short normal polarity interval (at 143.85–161.82 mbsf) (Fig. F11). The observed reversed polarity is in excellent agreement with the biostratigraphic age estimate (nannofossil Subzone NN19a) (Table T4), which corresponds to a period of expected normal polarity. Therefore, this normal polarity interval may be correlated with the Olduvai Subchron. The sedimentary hiatus below 163.18 mbsf (Core 18X) introduces a gap in the magnetostratigraphic record and complicates the identification of particular polarity chrons. However, magnetic measurements reveal that a shift of polarity from reversed to normal occurs at a depth of 197.03 mbsf (Fig. F11). Below this depth, the inclinations are dominantly normal between 197.03 and 206.86 mbsf, suggesting that this interval corresponds to a period of predominantly normal polarity. On the basis of foraminiferal assemblages, this interval is placed at the Zones N7/N6 boundary. Thus, the shift of polarity from reversed to normal found at 197.03 mbsf in Core 22X might correspond to Chron C5D (17.31–17.65 Ma). Between a depth of 209.73 and 338.5 mbsf, NRM intensities for Cores 23X through 36X are very weak and the data are highly scattered. Although magnetic measurements also suggest several polarity reversals were recorded in these cores, these polarity signals may not be reliable because of the weak magnetization of most of the sediments. The magnetostratigraphy and biostratigraphic zones are presented in Figure F11.

T4. Paleomagnetic and biostratigraphic datums, Site 898, p. 60.

Paleomagnetically Determined Sedimentation Rates for Hole 898A

Table T4 summarizes the paleomagnetic and biostratigraphic datums in Hole 898A. Similar to the reversal patterns found at Site 897, the Pleistocene and Pliocene sediments cored in Hole 898A have preserved records for the (1) Brunhes/Matuyama (0.78 Ma), (2) Jaramillo (0.99–1.07 Ma), and (3) Olduvai (1.77–1.95 Ma) at depths of 29.06, 101.74–106.88, and 143.85–161.82 mbsf, respectively. From this polarity stratigraphy, relatively precise sedimentation rates can be calculated. The paleomagnetic mean sedimentation rate at Site 898 for the age interval 0.78–1.77 Ma is 115.9 m/m.y. and is slightly lower (99.8 m/m.y.) for the period 1.77–1.95 Ma (Fig. F12). These estimates are comparable to those of at Site 897 (Fig. F8) and also to those estimated from a turbidite study (Milkert et al., 1996). We were not able to determine sedimentation rates for the sediments below 163.18 mbsf because of the presence of a hiatus and the absence of any reliable chronostratigraphic events. It is significant to note that the short hiatus at about the Pleistocene/Pliocene boundary is again inferred in the paleomagnetic records of Site 898. The geological implication is discussed further in a later section.

F12. Depth vs. age curve for Hole 898A, p. 40.

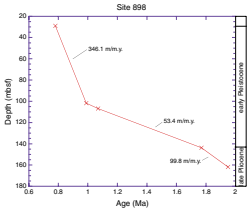

Site 900 (Hole 900A)

Magnetic Properties and Stability Tests

A total of 521 discrete samples were collected from cores in Hole 900A for shore-based measurements. A U-channel sample was also taken from Core 10R for a detailed polarity transition study. The quality of the paleomagnetic data from Site 900 depends strongly on the lithology of the recovered material; thus, the discussion here of magnetic

properties at Site 900 is organized on the basis of lithology. Recovered materials from Cores 1R through 4R are mud-dominated turbidites. These cores were too mechanically disturbed by drilling to allow meaningful measurements. Cores 5R through 17R are mainly nannofossil clay and ooze and have a strong magnetic signal (NRM intensities typically in the range 1–10 mA/m) that was easily measured. The magnetic behavior of these sediments is relatively straightforward, with easily identified ChRM on the orthogonal demagnetization diagrams (Fig. F13). As shown in Figure F13, although the remanence is still dominated by a single component of magnetization in the majority of cases, several samples did display a multicomponent nature with a characteristic component isolated after removal of a secondary component of the opposite polarity.

Except for two short intervals, the sediments from 181.5 to 748.9 mbsf were characterized by weak magnetic remanence. We could not measure the discrete samples taken from these sediments accurately, even in a shore-based field-free laboratory. The magnetic directions of these sediments often become very noisy and inconsistent. Therefore, it was not possible to determine a stable polarity for sediments recovered from this interval.

F13. Vector end point diagrams of demagnetization, Site 900, p. 41.

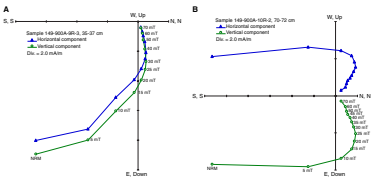

T5. Magnetic stratigraphy, Site 900, p. 61.

Magnetic Polarity Sequences at Site 900

Table T5 summarizes the paleomagnetic results from Hole 900A. Because biostratigraphic samples between depth interval 12.0 and 65.5 mbsf have been assigned ages in the range from 0.8 to 2.6 Ma, the observed predominantly negative inclination in this interval suggests that these sediments were deposited within the Matuyama Chron (0.78–2.58 Ma). This match must be the case because the Matuyama is the only reversed chron of this particular age. Between 21.76 and 26.62 mbsf, the cores have been assigned to nannofossil Subzone NN19f (0.92–1.10 Ma). Therefore, the first shift in polarity from normal to reversed at a depth of 21.08 mbsf would correspond to the onset of the Jaramillo Subchron (0.99 Ma) rather than to the Brunhes/Matuyama boundary (0.78 Ma). In other words, Hole 900A contains only a partial record of the Jaramillo Subchron and no record of the Brunhes/Matuyama boundary. The biostratigraphic data also suggest that sediments around 43.9–48.0 mbsf may be of late Pliocene age (Subzone NN19a and Zones N23/N22). This information suggests that the well-defined record of a normal interval (47.00–48.15 mbsf) corresponds to the Olduvai normal polarity subchron. As the biostratigraphic data place cores at a depth of 65.5 mbsf to 2.6 Ma (within Zone NN16), the shift in polarity from reversed to normal at 64.55 mbsf may represent the Matuyama/Gauss boundary (2.58 Ma). Like Hole 898A, the Reunion Subchron is not observed in Hole 900A. Finally, the lower boundaries of both nannofossil Zone NN15 and foraminiferal Zone N19 have been placed at about 89 mbsf, which would suggest that the sediments around this depth were deposited within the Gilbert Chron (early Pliocene). This biostratigraphically inferred chronostratigaphic event plays a crucial role in the interpretation of the magnetic zones identified in the lower Pliocene.

Although biostratigraphic age markers are not well defined below a depth of 89.39 mbsf, the magnetic polarity patterns identified from depth interval 76.9–141.85 mbsf allow tentative correlations of the magnetic zones with the GPTS. Within the Gauss Chron, the inclinations of the U-channel sample in Core 149-900A-10R at a depth of 77.1

mbsf changed from reversed to normal, which probably recorded the transition of the Mammoth Subchron (3.22–3.33 Ma). The Kaena Subchron (3.04–3.11 Ma) appears not to be recorded in Hole 900A. Within the Gilbert reversed chron, four thin normal polarity zones between 84.2 and 95.6 mbsf show a good correlation with the Cochiti (4.18–4.29 Ma), Nunivak (4.48–4.62 Ma), Sidufjall (4.80–4.89 Ma), and Thvera (4.98–5.23 Ma) Subchrons at depth intervals of 84.2–84.4, 87.1–87.5, 89.3–90.0, and 95.2–95.6 mbsf, respectively. The Gilbert/C3A Chron boundary (5.83 Ma) occurs at a depth of 113.8 mbsf, and the shift in polarity from reversed to normal at 134.29 mbsf may correspond to the Chron C3A/C4 boundary (7.27 Ma). Similar to the Gilbert Chron, the two thin normal zones between 113.8 and 115.8 mbsf, the three normal zones between 121.9 and 132.7 mbsf, and the three normal zones between 134.3 and 145.0 mbsf may be correlated with the corresponding normal polarity intervals in Epochs 5, 6, and 7, respectively. The magnetostratigraphic and biostratigraphic zones at Hole 900A are summarized in Table **T6,** and the interpretation of the magnetostratigraphy is presented in Figure **F14.**

Paleomagnetically Determined Sedimentation Rates at Site 900

As indicated in Figure **F15**, about four separate straight line segments may be fitted to the paleomagnetic correlation points for Hole 900A (Table **T6**). This depth-age plot shows a change in slope (5.9 m/m.y.) near 48 mbsf, above which sedimentation rates are 37.0 m/m.y. and below which sedimentation rates vary from 23.0 to ~7.2 m/m.y. Between the lower Pliocene at 84.2 mbsf and the uppermost Miocene at 95.2 mbsf is another possible unconformity (Fig. **F15**). According to this interpretation, two significant sedimentary hiatuses are present: one is close to the Pliocene/Pleistocene boundary in an identical position to that proposed at Sites 897 and 898; the other is in the interval dated at 4.18–4.89 Ma at ~90 mbsf. It is important to note the absence of direct paleontological evidence for these hiatuses, especially for the proposed Pliocene–Pleistocene hiatus, because all standard upper Pliocene and Pleistocene calcareous nannoplankton and planktonic foraminifer zones appear to be present at these sites (Liu et al., 1996; Gervais, 1996). The average sedimentation rates at Site 900 are significantly lower than those of Sites 897 and 898 for the same age range. This may be due to the fact that Site 900 is located near the foot of the Portuguese continental rise adjacent to the Iberia Abyssal Plain. Sediments carried by the turbidity currents may merely bypass the shelf, flow downslope, and come to rest at the abyssal plains (e.g., at Sites 898 and 897). This interpretation agrees with shipboard geological observations, which suggest that compared with Sites 897 and 898, much more hemipelagic sediment but fewer turbidites were found in the cores recovered from Hole 900A (Shipboard Scientific Party, 1994c). On the other hand, the comparatively abrupt changes at a depth of 48 mbsf may suggest the additional influence of other factors. For example, they may be associated with the onset of the Arctic glaciation or increased detrital input resulting from the worldwide regression to the commencement of this glaciation (Weaver et al., 1986).

T6. Paleomagnetic and biostratigraphic datums, Site 900, p. 63.

F14. Magnetic inclination, inferred polarity, and biostratigraphic zones, Site 900, p. 43.

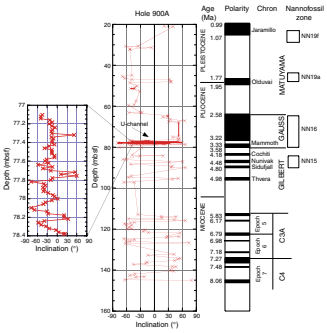

F15. Depth vs. age curve for Hole 900A, p. 44.

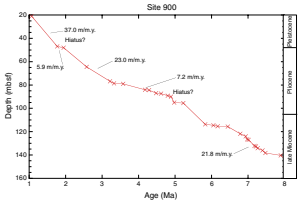

Site 1067 (Hole 1067A)

Magnetic Properties and Polarity Sequences at Site 1067

Approximately 116 m of claystone was cored in Hole 1067A before crystalline bedrock was encountered. The sediments recovered from this interval (Cores 1R through 13R; 648.0–763.8 mbsf) belong to a single lithostratigraphic subunit that consists of claystone and calcareous claystone and sandy siltstone. The top of the cored section was dated as middle Eocene. The NRM intensities and magnetic susceptibilities are similar to sediments of the same age from Leg 149, Site 900, 800 m to the west. The colors of the sediments from the upper 75 m of this cored interval, composed predominantly of greenish gray to light gray claystone and silty claystone, are noticeably different from those from the lower 40 m, which are predominantly brownish red to red claystone and silty claystone (see Shipboard Scientific Party, 1998a). Correspondingly, the upper sediments have lower NRM intensities (~10^{-4}A/m) and magnetic susceptibilities (~5 to 25 × 10^{-5} SI units) than the lower sediments (~10^{-3} A/m and ~15 to >40 × 10^{-5} SI units, respectively). It appears that these hemipelagic sediments were brown when first deposited, but subsequent chemical reduction has locally turned them green (Shipboard Scientific Party, 1998a). Exceptionally, the reddish brown (5Y 4/4) sediments (Core 12R; 744.5–754.2 mbsf) at the base of lithostratigraphic Subunit IIB are not weakly magnetized and also display higher values of magnetic susceptibility. Interestingly, a similar phenomenon was observed at Leg 149, Site 900. Core 149-900A-77R, also at the base of the Subunit IIB (720.0 mbsf), has the same age (early Eocene), rock type, and color and the same characteristic peaks in NRM intensity and volume susceptibility (Shipboard Scientific Party, 1994c; Liu, 1996). Furthermore, this characteristic brown bed and the associated peaks in NRM intensity and volume susceptibility are also observed at Sites 1068 and 1069 (Table T7) with the same age determination. The magnetic susceptibilities of the dark brown bed at these sites are typically an order of magnitude higher than in the overlying sediments, and NRM intensities are as much as two orders of magnitude higher than those for sediments both above and below. Thus, they provide a useful basis for correlation of this change between sites and present a discernible magnetic boundary among the Leg 173 drill sites.

Pass-through measurements of the archive halves of the cores at Site 1067 yielded dominantly positive inclinations (normal polarity). The only evidence for a possible reversed chron or subchron occurs at the tops of Cores 10R and 11R (734.8–744.5 mbsf). Further measurements and progressive demagnetization results from corresponding discrete samples succeeded in substantiating these polarity changes and revealed additional detail in the polarity patterns. Thirty-nine additional discrete samples, taken from the working half of the core, were progressively AF and thermally demagnetized to determine directional stability and to verify the reliability of the measurements from the archive half. All samples were separately subjected to AF and thermal demagnetization (Table T8). Figure F16 exhibits typical demagnetization behavior of these sediments during AF and thermal demagnetization. Samples from this site displayed similar responses to demagnetization, as would be expected from the uniform sedimentary facies.

A combination of magnetostratigraphy and biostratigraphy provides a preliminary chronostatigraphic framework for the Hole 1067A sedimentary sequences (Table T9). The stratigraphically highest polarity

T7. Eocene marker bed observations, p. 64.

T8. Magnetic stratigraphy, Site 1067, p. 65.

F16. Vector end point diagrams of demagnetization, Site 1067, p. 45.

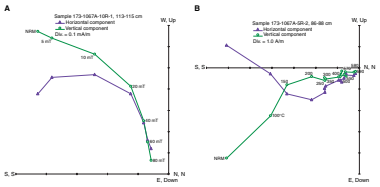

T9. Paleomagnetic and biostratigraphic datums, Site 1067, p. 66.

change at Site 1067 occurs at a depth of 661.10 mbsf. Because the uppermost 40 m of sediment at Site 1067 is known to be of middle Eocene age (Shipboard Scientific Party, 1998a) and because the boundary between biostratigraphic Subzones CP14a and CP13c is placed at a depth of 659 mbsf, this polarity change from normal (above) to reversed (below) is likely the "C20n/C20r" (43.8 Ma) contact. Subsequently, the normal polarity of Cores 6R through 9R suggests that these sediments were deposited during Chron C21n (i.e., 46.3–47.9 Ma), which agrees well with the biostratigraphic age markers (CP13a–CP12b). Key nannofossil markers for the lower Eocene sediments are also in excellent agreement with the paleomagnetic data (Table T9). Especially, the characteristic brown bed (Core 12R) has been used as an anchor point in the correlation. Thus, the presently available paleomagnetic data suggest that five magnetozones (C20n–C24n) can be recognized at Site 1067 that range from middle to early Eocene in age (42.5–53.35 Ma). The magnetostratigraphic and biostratigraphic zones in Hole 1067A are summarized in Table T9, and the interpretation of the magnetostratigraphy is presented in Figure F17.

F17. Magnetic inclination, inferred polarity, and biostratigraphic zones, Site 1067, p. 46.

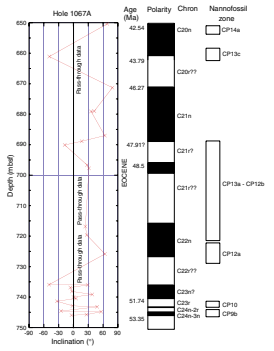

F18. Depth vs. age curve for Hole 1067A, p. 47.

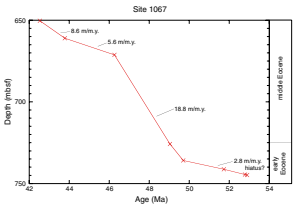

Paleomagnetically Determined Sedimentation Rates at Site 1067

If the correlation with the GPTS shown in Figure F17 and Table T9 is taken as at least approximately correct, then sedimentation vs. time can be determined for Site 1067. The estimated mean sedimentation rates from the magnetostratigraphy of Site 1067 are shown in Figure F18. The average sedimentation rates are significantly lower than those of the Pliocene–Pleistocene sequence determined from Leg 149 sites, reflecting the paleoceanographic history of Site 1067 during the Eocene. The sediment accumulation rate plot shows a change in slope (5.6 m/m.y.) near 670 mbsf, above which rates are 8.6 m/m.y. and below which rates are 18.8 m/m.y. There is a sharp decrease in sediment accumulation rate around 740 mbsf. A possible unconformity or short hiatus is also indicated at close to the Eocene/Paleocene boundary at ~745 mbsf, which is similar to the one inferred from paleontological evidence (Shipboard Scientific Party, 1998a). Sedimentation rates were also unusually low in the upper Paleocene and some of the lower Eocene sections cored at DSDP sites in the western North Atlantic (Tucholke and Mountain, 1986). The low sedimentation rates there were probably affected by the action of abyssal contour-following currents, which intermittently caused extensive seafloor erosion along the continental margins (Tucholke and McCoy, 1986). Low rates during the early Eocene would have also been affected by high eustatic sea level, which would have lowered pelagic carbonate accumulations in the deep sea (Wise and van Hinte, 1987; Olsson and Wise, 1987).

Site 1068 (Hole 1068A)

Paleomagnetic Stability Tests and General Polarity Sequences for Site 1068

Results from the pass-through cryogenic magnetometer measurements indicate that a number of magnetic polarity reversals may be discerned on the basis of changes in sign of the inclinations of Cores 1R through 15R (711.3–855.9 mbsf). A total of 141 discrete paleomagnetic samples from these sediments were subjected to progressive AF or ther-

mal demagnetization to verify the magnetostratigraphic results from the pass-through cryogenic magnetometer and to understand the magnetic behavior during stepwise demagnetization (Table T10). Figure F19 illustrates the response to AF and thermal demagnetization for four representative samples from these sediments. After removal of a random component of magnetization by demagnetization, the characteristic component was quickly revealed. The inclination of this final high-temperature component has a value close to the expected inclination at the site from the Paleocene to Eocene (59°). Because of this and because of the high magnetic stability, we interpret the characteristic component as representing a record of the paleomagnetic field close in age to the deposition of these sediments at Site 1068.

A useful magnetic polarity pattern was obtained in Hole 1068A, encompassing an age range from middle Eocene to the end of the Cretaceous Long Normal (~121 Ma). Work on the Cretaceous sequence is still in progress and will be presented elsewhere. Polarity interpretations are relatively straightforward for the middle Eocene and upper Paleocene portions of the section and corroborate the biostratigraphic information. The available paleomagnetic data suggest that five magnetozones (C21n–C25n) that range in age from 46.26 to 56.39 Ma can be recognized at Site 1068. The characteristic brown bed was also encountered in Core 8R with sharp peaks in downhole magnetic susceptibility and intensity. Available biostratigraphic data suggest that this bed is synchronous with those at Sites 1067 and 1069 (calcareous nannofossil Subzone CP9b [NP11] or the *Discoaster binodosus* Subzone) (see Shipboard Scientific Party, 1998b; McGonigal and Wise, **Chap. 4,** this volume). The normal polarity intervals exhibited by samples from this bed appear to have the right pattern and spacing to correspond to Chron C24n. The magnetostratigraphic and biostratigraphic zones in Hole 1068A are summarized in Table T11, and the interpretation of the magnetostratigraphy is presented in Figure F20.

Paleomagnetically Determined Sedimentation Rates at Site 1068

Figure F21 illustrates sediment accumulation vs. time curve for Site 1068, which is similar to that for Site 1067. The paleomagnetic-suggested mean sedimentation rates at Site 1068 are 6.2 m/m.y. for the interval 47.91–49.71 Ma, a rather high 16.5 m/m.y. between 49.71 and 53.35 Ma, and a lower rate (4.7 m/m.y.) for a period of 53.35–55.90 Ma. These estimates are comparable to those at Site 1067 (Fig. F18) and are also consistent with those inferred from the biostratigraphy (Shipboard Scientific Party, 1998b). It is significant that the possible short hiatus at about the Eocene/Paleocene boundary is again inferred in the paleomagnetic records of Site 1068.

Site 1069 (Hole 1069A)

Magnetic Polarity Sequences at Site 1069

Magnetic measurements were taken at 5-cm intervals on the archive halves of cores from Hole 1069A using the pass-through cryogenic magnetometer. After measuring the NRMs, sections were progressively AF demagnetized using 10-mT steps, starting at 10 and ending at 60 mT. Fifty-eight additional discrete samples, taken from the working halves of the core, were progressively AF and thermally demagnetized to deter-

T10. Magnetic stratigraphy, Site 1068, p. 67.

F19. Vector end point diagrams of demagnetization, Site 1068, p. 48.

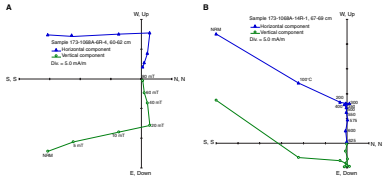

T11. Paleomagnetic and biostratigraphic datums, Site 1068, p. 69.

F20. Magnetic inclination, inferred polarity, and biostratigraphic zones, Site 1068, p. 50.

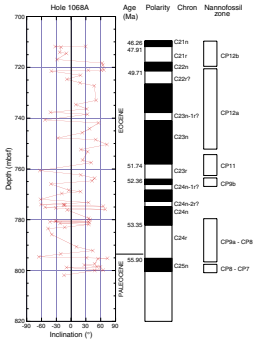

F21. Depth vs. age curve for Hole 1068A, p. 51.

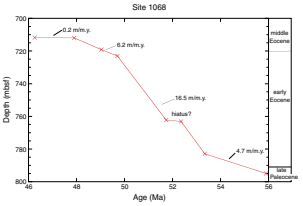

mine directional stability and to check the reliability of the measurements from the archive halves (Table T12). Lower Eocene sediments in Core 5R (757–767 mbsf) were too fractured to obtain minicores, but the inclinations in the pass-through measurements show both normal and reversed polarity and become less steep during progressive AF demagnetization (see fig. 19 of Shipboard Scientific Party, 1998c, p. 246). These possible polarity reversals thus may be tentatively used for constructing a magnetostratigraphy for this interval. Figure F22 exhibits typical AF and thermal demagnetization behavior of sediments from Hole 1069A. Thermal demagnetization methods proved to be more effective for determining stable magnetic directions of the sediments.

The characteristic brown bed and the associated peaks in NRM intensity and volume susceptibility, previously observed at Leg 173 (Holes 1067A and 1068A) and during Leg 149 at Site 900 (Shipboard Scientific Party, 1994c), were also observed in Hole 1069A. This intensity and susceptibility spike is found in Core 7R at a depth of ~776 mbsf. This further suggests that this brown bed shows promise as a stratigraphic marker for correlation of the lower Eocene sediments of the Iberia Abyssal Plain. The significance of this observation to the sediment mineralogy or regional paleoceanographic conditions is discussed in a later section.

As with Site 1068, five magnetozones (C21n–C25n) have been identified at Site 1069. Among them, Chron C23n was not well determined and the polarity changes are suggested by the pass-through measurements, as mentioned above. The magnetostratigraphic and biostratigraphic zones in Hole 1069A are summarized in Table T13, and the interpretation of the magnetostratigraphy is presented in Figure F23.

Paleomagnetically Determined Sedimentation Rates at Site 1069

The paleomagnetically estimated mean sedimentation rates at Site 1069 are shown in Figure F24, which are generally similar to those at Sites 1067 and 1068. Low sedimentation rates (6.4–8.8 m/m.y.) are evident for most age intervals except for near the middle/lower Eocene boundary, where the sedimentation rate is higher (15.5 m/m.y.). The low sedimentation rates at Site 1069 were likely affected by the action of abyssal contour-following currents that can cause extensive seafloor erosion along the continental margins (Tucholke and McCoy, 1986) and by high eustatic sea level, which would have lowered pelagic carbonate accumulations in the deep sea (Wise and van Hinte, 1987; Olsson and Wise, 1987), as mentioned previously.

Paleolatitudes

By assuming an axial geocentric dipole, the inclination of the time-averaged magnetic field recorded in the sediments can be used to calculate the paleolatitude at which the sediments were deposited. However, there are several problems in estimating paleolatitudes based on inclination results from ODP drill cores. These include undetected core disturbances, undetected tectonic dips or local rotations, effects of secondary overprinting, and compaction and possible depositional inclination errors in marine sediments. Because the component of drilling-induced magnetization (inclinations >70°) has the tendency to make normal polarity magnetization steeper and reversed polarity magnetization shallower, we excluded those samples with inclinations

T12. Magnetic stratigraphy, Site 1069, p. 70.

F22. Vector end point diagrams of demagnetization, Site 1069, p. 52.

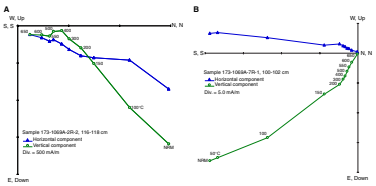

T13. Paleomagnetic and biostratigraphic datums, Site 1069, p. 71.

F23. Magnetic inclination, inferred polarity, and biostratigraphic zones, Site 1069, p. 54.

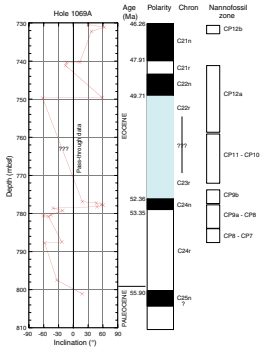

F24. Depth vs. age curve for Hole 1069A, p. 55.

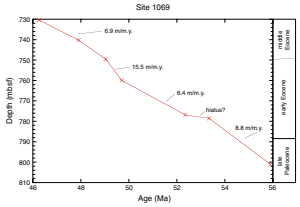

>+70° or <–10° from the mean calculation. We have employed the technique developed by McFadden and Reid (1982) to estimate true mean inclinations from our core data. This technique, coupled with our age information, allows us to estimate Fisher means and confidence limits over a given time intervals. Using estimated average inclinations from the six drill sites, we have also calculated paleolatitudes for the Iberia sites. The results are summarized in Table T14.

T14. Paleolatitudes for Iberia drilled sites, p. 72.

The paleolatitudes calculated from the averaged inclinations suggest that the Iberia sites were located at 24°N during the Eocene and ~27°N during the Pliocene–Pleistocene. The calculated paleolatitude for the Eocene is similar to previously published estimates of 28°N for the age interval 37–66 Ma (Van der Voo, 1993), indicating that there is no inclination error in these sediments. However, the 26°N mean paleolatitude for the Pliocene and Pleistocene is a significant departure from today's 40°N value at drilling sites and is surprising. We will return to this puzzle in the discussion section below.

DISCUSSION

The characteristic magnetization observed in Holes 897C, 898A, and 900A of Leg 149 and Holes 1067A, 1068A, and 1069A of Leg 173 is of both normal and reversed polarities. Fairly complete magnetostratigraphies were obtained from these six sites for the upper Paleocene to Eocene and for the Pliocene to Pleistocene.

As we emphasized in the beginning section, before establishing the magnetostratigraphy one has to demonstrate that the remanent magnetization of the sediment is the stable primary magnetization acquired at or close to the time of deposition. The precise time at which sediments acquire their magnetization is always difficult to evaluate, and there is still no universally applicable test that allows a distinction to be made between depositional remanent magnetization acquired at the time of deposition and chemical remanent magnetization (CRM) acquired as a result of the growth of new magnetic minerals during diagenesis. Although the possibility of magnetic grains carrying a CRM cannot be completely ruled out, there is some indirect evidence to suggest this is unlikely in these particular sediments. As shown in Table T15, application of the reversal test on the mean normal and reversed inclinations of the six sites yields positive results for Sites 898, 900, 1067, and 1069; the two polarity inclinations are not statistically different from each other at the 95% confidence level (McFadden and McElhinny, 1990). The positive results from this mean inclination reversal test indicate that the ChRM is a record of the paleomagnetic field close to the time of formation of these sediments.

T15. Reversal test results using inclination statistics, p. 73.

Further evidence that the magnetization of these sediments was acquired close to their time of deposition is the fact that patterns of magnetic reversals have been identified that can be matched with the established polarity timescale. If the magnetization had been introduced as a result of the variable processes of diagenesis at significantly different times from the initial deposition, then such a close match would be unlikely. Finally, most of the observed magnetostratigraphy from the characteristic directions is in excellent agreement with that to be expected from the stratigraphic position of the sequence deduced from the biostratigraphic data. On these grounds, it is argued that the characteristic directions of magnetization observed from these sedi-

ments are most likely the original primary magnetization acquired when the sediments were deposited.

As with most applications of magnetostratigraphy, one of the greatest problems is the correct matching of the observed sequence of magnetic polarity zones with the appropriate part of the GPTS. At Sites 897 and 898, this matching is usually straightforward and unambiguous, as the observed polarity sequence is defined from the sedimentary succession that is more or less continuous up to recent time. Thus, in the two sites illustrated in Figures **F8** and **F11,** the youngest normal polarity zone can correlated confidentially with the Brunhes normal chron, the preceding dominantly reversed polarity zone with the Matuyama reversed chron, and so on through the sequence. For Site 900, the available sedimentary section is not continuous through the present; hence, the interpretation of the paleomagnetic record is less straightforward. However, available biostratigraphic data from this site can assist in deciding which observed magnetic polarity zone or set of zones should be correlated with which magnetic chron on the GPTS, such as the match with the Matuyama reversed chron. For Sites 1067, 1068, and 1069, the available biostratigraphic data are well documented, which assists in magnetic correlation. Especially, the characteristic brown bed (with sharp peaks in downhole magnetic susceptibility and intensity) is synchronous at all three Leg 173 sites, as suggested by the biostratigraphic data. This bed has been used as an anchor point in the correlation for the three Leg 173 sites. This combined paleomagnetic, biostratigraphic, and sedimentologic study has demonstrated the potential value of providing the essential link between the biostratigraphic and geomagnetic polarity timescales.

The patterns of magnetic polarity reversals identified at Sites 897, 898, and 900 correlate well with the known magnetic polarity timescale for the past 5 m.y. and allow the determination of accurate sedimentation rates for these sites (Figs. **F9, F12, F15**). These sedimentation rate values are not corrected for compaction; consequently, part of the apparent series of increases in accumulation rates for the interval 2–2.5 Ma at Sites 897 and 898 may be attributed to this cause. The identification of the early Pleistocene hiatus at all three sites suggests the occurrence of a contemporaneous oceanographic event, the influence of which may have been sufficiently widespread to affect much of the Iberia Abyssal Plain and is probably associated with Pleistocene glaciation (Weaver et al., 1986).

The combined results from Sites 1067, 1068, and 1069 extend the Pliocene magnetostratigraphy obtained from Leg 149 sites into the Eocene/Paleocene. The correlation of polarity among the sites using the biostratigraphic zonation and the brown bed for control is quite good. Because nearly all intervals are represented by multiple samples, it would appear that the continuity of sedimentation and sampling density at each site was adequate to record and identify each polarity interval, albeit minimally in a few places. Low sedimentation rates are evident for most of the successions except for near the middle/lower Eocene boundary. A possible short hiatus at about the Paleocene/Eocene boundary is inferred at the paleomagnetic records of Sites 1067, 1068, and 1069, as well as from planktonic foraminiferal data at Site 900 (Gervais, 1996). This short hiatus probably reflects the action of abyssal contour-following currents, which intermittently caused extensive seafloor erosion along the continental margins in the Northern Atlantic Ocean (Tucholke and McCoy, 1986). Interestingly, there is an apparent coincidence in time between this short hiatus and known as-

pects of the paleobiogeography, climate changes, and tectonic evolution of the northern Atlantic. A major benthic faunal turnover occurred near the Paleocene/Eocene boundary (Tjalsma and Lohmann, 1983). Marked climatic warming episodes were also recorded during the late Paleocene and early Eocene (Berggen and Olsson, 1986). In the early Eocene (magnetic Chron C24 = 52.4–55.9 Ma), a change from a two- to three-plate geometry occurred when spreading began along the incipient Reykjanes Ridge and in the Norwegian-Greenland Sea, resulting in the separation of Greenland and Eurasia (Berggen and Olsson, 1986). The Iberia-Africa plate rotated counterclockwise with respect to Europe since Anomaly 21. This led to the initial opening of King's Trough and continued a complex shear/thrust geometry along the northern Iberia margin (Pyrenean Orogeny) (Tucholke and McCoy, 1986). However, the detailed "causality chains" (e.g., from tectonic events [rotation and rifting] to paleoceanographic events [deep-water currents and redistribution of benthic faunal fossils] to sedimentary processes) are still poorly understood. Improved methods of detecting the cause-and-effect relationships between these events are needed.

As can be seen from Tables **T1, T3, T5, T8, T10,** and **T12,** we present here the magnetic polarity stratigraphy determined for only a small portion of the total recovered section in the Cenozoic. The paleomagnetic results from other portions cannot be interpreted with confidence because of the weak magnetization. As mentioned previously, there is a magnetic boundary where NRM intensity sharply decreases at the three Leg 149 sites. In Hole 897C, this magnetic boundary occurs at a depth of 334 mbsf, in Hole 898A it occurs at 197 mbsf, and in Hole 900A at 146 mbsf. In all three cases, this change is reasonably well defined stratigraphically within the middle Miocene nannofossil Zones NN5–NN8 (de Kaenel and Villa, 1996), indicating that it may represent a synchronous event at the three sites. It is also significant to note that at all three holes this abrupt decrease in NRM intensity also correlates precisely with a sharp reduction in magnetic susceptibility (see Shipboard Scientific Party, 1994a, 1994b, 1994c). Both the NRM intensity and magnetic susceptibility are parameters that likely reflect variations in type and amount of magnetic minerals within the sediments. Because the NRM intensity may also be a function of other factors, such as geomagnetic field intensity at the time of deposition and secondary magnetization acquired during drilling or storage, susceptibility is a more useful index of magnetic mineral content. In this study, there is a high probability that both parameters reflect variations in the proportion of terrigenous magnetite owing to changes in source area, sediment supply rate, or rate of dissolution of the nonmagnetic component (calcareous and siliceous). Because the dominant magnetic mineral in these sediments is magnetite, most likely of detrital origin, this sharp decrease in susceptibility and NRM intensity appears to represent an abrupt reduction in the rate of supply of terrigenous material in the middle Miocene. Preliminary shipboard data also indicate that at these depths where the both NRM intensity and susceptibility decrease, there is also a transition from oxidized iron phased in the Miocene brown clays to reduced iron phases in the upper Oligocene-age green and gray clays (Shipboard Scientific Party, 1994a, 1994b, 1994c). The suggested boundary between oxidized and reduced iron phases corresponds to the top of a region of high sulfate concentration, which is apparent in the interstitial water analyses (see "Inorganic Geochemistry" sections in Shipboard Scientific Party, 1994a, 1994b, 1994c). The diminished supply of terrigenous material at the end of the early Miocene may reflect

the occurrence of an important oceanographic or tectonic event at this time, which resulted in a change in circulation patterns, sediment supply routes, or source areas within the Iberia Abyssal Plain. This interpretation is fully consistent with the middle Miocene regional unconformity found in much of western Iberia. This unconformity is believed to be the result of a northwest-southeast compressional folding in the Betic Mountains of southern Spain (Mauffret et al., 1989).

Another magnetic boundary is in the lower Eocene characteristic brown bed that was recognized at Sites 1067, 1068, and 1069 (Table T7). This magnetic boundary (strong NRM intensity and susceptibility) not only provides a proxy stratigraphic marker for correlation between the sedimentary records of drilled sites during Leg 173, but also reveals a paleogeographic event that is synchronous at the three sites. At sea, we have noted a similar bed that has also been reported in the Bermuda Rise Formation at Site 603 during DSDP Leg 93 (Shipboard Scientific Party, 1987). Section 93-603B-16-3 is very similar to the characteristic brown bed encountered at Leg 173 sites, composed of lower Eocene reddish brown radiolarian claystone interbedded with black bands that contain greater amounts of Mn and Fe oxides. We are still unable to relate the significance of this observation to the sediment mineralogy or regional paleoceanographic conditions. However, we note that there is an apparent coincidence of an extraterrestrial impact on the North Atlantic continental shelf in early Eocene time (Jansa and Pe-Piper, 1987). The diameter of the impactor (perhaps a stony meteorite or a cometary nucleus) is estimated to be 2–3 km with whole-rock K-Ar isotope dates of 49.9–55.8 Ma (Jansa and Pe-Piper, 1987). Nevertheless, not much physical evidence for the event has been found in the surrounding sedimentary record. For example, sediment slumping specifically triggered by the seismic shock or by the massive tsunamis that would be expected has yet to be identified.

As mentioned, the estimated 26°N mean paleolatitude for the Pliocene and Pleistocene is a significant departure from today's 40°N value at the drilling site. The low paleolatitudes for the last 5 m.y. are so anomalous that we are obliged to consider carefully any hypotheses that might account for our results. Although there is evidence for a plate kinematic "fine structure" that occurred in the Atlantic Ocean during the last 10 m.y. (Vogt, 1986), resolution of possible plate motion variability at 1- to 10-m.y. scales has improved slowly and little progress has been made even on separating causes from effects. In light of this, it is tempting to accept the conservative "null" hypothesis that there has been no significant change in "present" plate motion speed. For the last 5-m.y. time interval, lithosphere plate motions are probably negligible.

We must be aware of two possibilities: (1) sediment dewatering and compaction can shallow the inclination of magnetization and (2) second-order tectonic movements can affect the interpretation of the results obtained. Lithologies that undergo substantial compaction (e.g., claystone) are probably more susceptible to inclination error through compaction. Such an inclination error has been demonstrated by sedimentation experiments in a known laboratory field (King, 1955) and also has been observed in natural sedimentary rocks. For example, upper Miocene to Pliocene marls from Sicily (Italy) show well-determined normal and reversed directions but are too shallow by ~20° with respect to the expected field direction (Linssen, 1991). On the other hand, analysis of magnetostratigraphic records from 52 deep-sea sediment cores collected from a wide variety of locations containing the Brunhes/Matuyama boundary (0.78 Ma) shows fundamental agreement of the

observed mean inclination and argues that no inclination error exceeding ~5° is present (Opdyke and Henry, 1969).

Although the first possibility cannot altogether be ruled out and a depositional inclination error can be suspected in our data set (as some of the sediments are slump or turbidite deposits), examinations of our data have not revealed inclinations that systematically shallow downcore (see Tables **T1, T3, T5;** Figs. **F8, F11, F14**). This observation demonstrates a lack of inclination error, although more systematic studies are needed. Future studies on variations in magnetic properties and grain size as a function of depth would be useful to examine this possibility.

For the second possibility, we are not sure whether the Pliocene sediments were significantly tilted after deposition. This problem clearly will affect the measured values of inclination. Although the hypothesis of undetected tectonic dips would account for the shallow inclinations naturally, it would be difficult for this hypothesis to explain the rather good agreement between estimated inclinations from the underlying Paleocene–Eocene cores and the expected values for the age interval 37–66 Ma (Van der Voo, 1993). More significant effects could arise from local undetected rotations. Although vertical-axis rotations cause changes to occur in declination only, if such rotations are also accompanied by block faulting then it is possible that changes in inclination can also occur (e.g., see McElhinny et al., 1996). Thus, one possible paleomagnetic interpretation of the shallow inclination result would be to propose that some tectonic rotation of the Iberia sites has occurred since Pliocene time. Again, this interpretation would not explain why the underlying Paleocene and Eocene sediments did not rotate.

Of course, one can always suspect that the agreement between estimated and expected Paleocene and Eocene paleolatitudes is merely coincidence. There is no geological evidence for such a rotation or for faulting activity in the drilled site. Therefore, it would require detailed seafloor mapping across a wide area in the region and much more careful work to confirm this interpretation.

To sum up, we have failed to find a satisfactory explanation for the shallow inclination results. Tectonic effects, although not certain, are likely explanations but may not be the only cause. This discussion highlights the difficulty of studying the magnetization of young marine sediments. Much more additional work is needed to prove or disprove various possibilities and constrain the magnetic interpretation.

CONCLUSIONS

The excellent agreement between the magnetostratigraphic dating and the biostratigraphic dating supports the contention that the magnetic remanence of the samples is primary. Sedimentary sections from Holes 897C, 898A, 900A, 1067A, 1068A, and 1069A have recorded a pattern of magnetic polarity reversals that correlates well with the known magnetic polarity timescale for the past 56 m.y. The polarity patterns from the Pliocene–Pleistocene turbidite sequence at the Leg 149 sites show that a reliable magnetostratigraphy can be established from the lower Pliocene to Holocene, including the Gilbert/Gauss boundary (3.58 Ma) through the Matuyama/Brunhes boundary (0.78 Ma). On the basis of distinct intervals of magnetic reversal zones and biostratigraphic datums, five magnetozones (C21n–C25n) that range in age from middle Eocene to late Paleocene can be recognized at the three Leg 173 sites. Paleomagnetic correlation within the Iberia margin Ceno-

zoic sequence is as promising as ever, especially now that a consistent magnetostratigraphy is emerging. The magnetostratigraphy of the Iberia sections allows the determination of accurate sedimentation rates and better constraints on the timing of deformation. Two short but significant hiatuses in the lower Pleistocene sections and at the Paleocene/Eocene boundary, respectively, were also recognized. These hiatuses may represent oceanographic events that affected a significant part of the Iberia Abyssal Plain region. It is clear from this study that the combination of paleomagnetic and biostratigraphic studies on the same deep-sea sediment cores can provide important information that has considerable relevance to understanding the evolution of continental margins.

ACKNOWLEDGMENTS

We thank the Legs 149 and 173 shipboard scientists, the crews of the *JOIDES Resolution,* the ODP staff, the Sedco crew, and the Catermar staff for their help and good company during Legs 149 and 173. We also wish to express our appreciation to the shore-based ODP staff members for all of their pre- and postcruise efforts. We thank John King and Yohan Guyodo for very constructive suggestions and helpful comments on the original manuscript. X.Z. extends special thanks to the paleomagnetism group of the Institute for Rock Magnetism at the University of Minnesota for support and fruitful discussions. Financial support for various parts of this research was provided by two grants to X.Z. from the U.S. Science Support Program of the Joint Oceanographic Institution, Inc., and the National Science Foundation grants EAR 97-06439 and EAR 9805444.

REFERENCES

Ade-Hall, J.M., and Johnson, H.P., 1976. Paleomagnetism of basalts, Leg 34. *In* Yeats, R.S., Hart, S.R., et al., *Init. Repts. DSDP,* 34: Washington (U.S. Govt. Printing Office), 513–532.

Berggren, W.A., Kent, D.V., Swisher, C.C., III, and Aubry, M.-P., 1995. A revised Cenozoic geochronology and chronostratigraphy. *In* Berggren, W.A., Kent, D.V., Aubry, M.-P., and Hardenbol, J. (Eds.), *Geochronology, Time Scales and Global Stratigraphic Correlation.* Spec. Publ.—Soc. Econ. Paleontol. Mineral. (Soc. Sediment. Geol.), 54:129–212.

Berggren, W.A., and Olsson, R.K., 1986. North Atlantic Mesozoic and Cenozoic paleobiogeography. *In* Vogt, P.R., and Tucholke, B.E. (Eds.), *The Geology of North America* (Vol. M): Geol. Soc. Am., 565–587.

Cande, S.C., and Kent, D.V., 1992. A new geomagnetic polarity time scale for the Late Cretaceous and Cenozoic. *J. Geophys. Res.,* 97:13917–13951.

————, 1995. Revised calibration of the geomagnetic polarity timescale for the Late Cretaceous and Cenozoic. *J. Geophys. Res.,* 100:6093–6095.

Channell, J.E.T., Erba, E., Nakanishi, M., and Tamaki, K., 1995. Late Jurassic–Early Cretaceous time scales and oceanic magnetic anomaly block models. *In* Berggren, W.A., et al. (Eds.), *Geochronology, Time Scales and Global Stratigraphic Correlation.* Spec. Publ.—Soc. Econ. Paleontol. Mineral., 54:51–63.

Clement, B.M., and Kent, D.V., 1987. Short polarity intervals within the Matuyama: transitional field records from hydraulic piston core sites from the North Atlantic. *Earth Planet. Sci. Lett.,* 81:253–264.

Clement, B.M., and Martinson, D.G., 1992. A quantitative comparison of two paleomagnetic records of the Cobb Mountain Subchron from North Atlantic deep-sea sediments. *J. Geophys. Res.,* 97:1735–1752.

de Kaenel, E., and Villa, G., 1996. Oligocene–Miocene calcareous nannofossils biostratigraphy and paleoecology from the Iberia Abyssal Plain. *In* Whitmarsh, R.B., Sawyer, D.S., Klaus, A., and Masson, D.G. (Eds.), *Proc. ODP, Sci. Results,* 149: College Station, TX (Ocean Drilling Program), 79–145.

Fisher, R.A., 1953. Dispersion on a sphere. *Proc. R. Soc. London A,* 217:295–305.

Gee, J., Staudigel, H., and Tauxe, L., 1989. Contribution of induced magnetization to magnetization of seamounts. *Nature,* 342:170–173.

Gervais, E., 1996. Cretaceous to Quaternary planktonic foraminiferal biostratigraphy of the Iberia Abyssal Plain. *In* Whitmarsh, R.B., Sawyer, D.S., Klaus, A., and Masson, D.G. (Eds.), *Proc. ODP, Sci. Results,* 149: College Station, TX (Ocean Drilling Program), 165–192.

Harland, W.B., Armstrong, R.L., Cox, A.V., Craig, L.E., Smith, A.G., and, Smith, D.G., 1990. *A Geologic Time Scale 1989:* Cambridge (Cambridge Univ. Press).

Jackson, M., 1990. Diagenetic sources of stable remanences in remagnetized Paleozoic cratonic carbonates: A rock magnetic study, *J. Geophys. Res.,* 95:2753–2761.

Jansa, L.F., and Pe-Piper, G., 1987. Identification of an underwater extraterrestrial impact crater, *Nature,* 327:612–614.

King, R.F., 1955. The remanent magnetism of artificially deposited sediments. *Mon. Not. R. Astron. Soc., Geophys. Suppl.,* 7:115–134.

Kirschvink, J.L., 1980. The least-squares line and plane and the analysis of palaeomagnetic data. *Geophys. J. R. Astron. Soc.,* 62:699–718.

Linssen, J., 1991. Properties of Pliocene sedimentary geomagnetic reversal records from the Mediterranean, *Geol. Ultraiectina,* 80.

Liu, L., 1996. Eocene calcareous nannofossils from the Iberia Abyssal Plain, *In* Whitmarsh, R.B., Sawyer, D.S., Klaus, A.,and Masson, D.G. (Eds.), *Proc. ODP, Sci. Results,* 149: College Station, TX (Ocean Drilling Program), 61–78.

Liu, L., Maiorano, P., and Zhao, X., 1996. Pliocene–Pleistocene calcareous nannofossils from the Iberia Abyssal Plain. *In* Whitmarsh, R.B., Sawyer, D.S., Klaus, A., and

Masson, D.G. (Eds.), *Proc. ODP, Sci. Results,* 149: College Station, TX (Ocean Drilling Program), 147–164.

Mankinen, E.A., Donnelly, J.M., and Grommé, C.S., 1978. Geomagnetic polarity event recorded at 1.1 m.y. B.P. on Cobb Mountain, Clear Lake volcanic field, California. *Geology,* 6:653–656.

Mankinen, E.A., and Grommé, C.S., 1982. Paleomagnetic data from the Coso Range, California, and the current status of the Cobb Mountain normal geomagnetic event. *Geophys. Res. Lett.,* 9:1279–1282.

Mauffret, A., Mougenot, D., Miles, P.R., and Malod, J.A., 1989. Cenozoic deformation and Mesozoic abandoned spreading centre in the Tagus abyssal plain (west of Portugal): results of a multichannel seismic survey. *Can. J. Earth Sci.,* 26:1101–1123.

McElhinny, M.W., McFadden, P.L., and Merrill, R.T., 1996. The time-averaged paleomagnetic field 0–5 Ma. *J. Geophys. Res.,* 101:25007–25027.

McFadden, P.L., and McElhinny, M.W., 1990. Classification of the reversal test in palaeomagnetism. *Geophys. J. Int.,* 103:725–729.

McFadden, P.L., and Reid, A.B., 1982. Analysis of paleomagnetic inclination data. *Geophys. J. Roy. Astro. Soc.,* 67:307–319.

McKenzie, D., 1978. Some remarks on the development of sedimentary basins. *Earth Planet. Sci. Lett.,* 40:25–32.

Merrill, R.T., McElhinny, M.W.,and McFadden, P.L., 1996. *The Magnetic Field of the Earth: Paleomagnetism, the Core and the Deep Mantle:* San Diego (Academic).

Milkert, D., Weaver, P.P.E., and Liu, L., 1996. Pleistocene and Pliocene turbidites from the Iberia Abyssal Plain. *In* Whitmarsh, R.B., Sawyer, D.S., Klaus, A., and Masson, D.G. (Eds.), *Proc. ODP, Sci. Results,* 149: College Station, TX (Ocean Drilling Program), 281–294.

Olsson, R.K., and Wise, S.W., 1987. Upper Maestrichtian to middle Eocene stratigraphy of the New Jersey slope and coastal plain. *In* van Hinte, J.E., Wise, S.W., Jr., et al., *Init. Repts. DSDP,* 93 (Pt. 2): Washington (U.S. Govt. Printing Office), 1343–1365.

Opdyke, N.D., and Channell, J.E.T., 1996. *Magnetic Stratigraphy:* New York (Academic Press).

Opdyke, N.D., and Henry, K.W., 1969. A test of the dipole hypothesis, *Earth Planet. Sci. Lett.,* 6: 139–151.

Roberts, A.P., Cui, Y.L., and Verosub, K.L., 1995. Wasp-waisted hysteresis loops: mineral magnetic characteristics and discrimination of components in mixed magnetic systems. *J. Geophys. Res.,* 100:17,909–17,924.

Sawyer, D.S., Whitmarsh, R.B., Klaus, A., et al., 1994. *Proc. ODP, Init. Repts.,* 149: College Station, TX (Ocean Drilling Program).

Shipboard Scientific Party, 1987. Site 603. *In* van Hinte, J.E., Wise, S.W., Jr., et al., *Init. Repts. DSDP,* 93, Pt. 2: Washington (U.S. Govt. Printing Office), 25–276.

————, 1994a. Site 897. *In* Sawyer, D.S., Whitmarsh, R.B., Klaus, A., et al., *Proc. ODP, Init. Repts.,* 149: College Station, TX (Ocean Drilling Program), 41–113.

————, 1994b. Site 898. *In* Sawyer, D.S., Whitmarsh, R.B., Klaus, A., et al., *Proc. ODP, Init. Repts.,* 149: College Station, TX (Ocean Drilling Program), 115–146.

————, 1994c. Site 900. *In* Sawyer, D.S., Whitmarsh, R.B., Klaus, A., et al., *Proc. ODP, Init. Repts.,* 149: College Station, TX (Ocean Drilling Program), 211–262.

————, 1998a. Site 1067. *In* Whitmarsh, R.B., Beslier, M.-O., Wallace, P.J., et al., *Proc. ODP, Init. Repts.,* 173: College Station, TX (Ocean Drilling Program), 107–161.

————, 1998b. Site 1068. *In* Whitmarsh, R.B., Beslier, M.-O., Wallace, P.J., et al., *Proc. ODP, Init. Repts.,* 173: College Station, TX (Ocean Drilling Program), 163–218.

————, 1998c. Site 1069. *In* Whitmarsh, R.B., Beslier, M.-O., Wallace, P.J., et al., *Proc. ODP, Init. Repts.,* 173: College Station, TX (Ocean Drilling Program), 219–263.

Spell, T.L., and McDougall, I., 1992. Revisions to the age of the Brunhes-Matuyama boundary and the Pleistocene geomagnetic polarity timescale. *Geophys. Res. Lett.,* 19:1181–1184.

Tauxe, L., Mullender, T.A.T., and Pick, T., 1996. Potbellies, wasp-waists, and superparamagnetism in magnetite hysteresis, *J. Geophys. Res.,* 101:571–583.

Tjalsma, R.C., and Lohmann, G.P., 1983. Paleocene-Eocene bathyal and abyssal benthic foraminifera from the Atlantic Ocean. *Micropaleontol. Spec. Publ.,* 4.

Tucholke, B.E., and McCoy, F.W., 1986. Paleogeographic and paleobathymetric evolution of the North Atlantic Ocean. *In* Vogt, P.R, and Tucholke, B.E. (Eds.), *The Western North Atlantic Region.* Geol. Soc. Am., Geol. of North Am. Ser., 589–602.

Tucholke, B.E., and Mountain, G.S., 1986. Tertiary paleoceanography of the western North Atlantic Ocean. *In* Vogt, P.R., and Tucholke, B.E. (Eds.), *The Western North Atlantic Region.* Geol. Soc. Am., Geol. of North Am. Ser., 631–650.

Van der Voo, R., 1993. *Paleomagnetism of the Atlantic, Tethys and Iapetus Oceans:* Cambridge (Cambridge Univ. Press).

Vogt, P.R., 1986. Magnetic anomalies and crustal magnetization. *In* Vogt, P.R., and Tucholke, B.E. (Eds.), *The Geology of North America* (Vol. M): Boulder (Geol. Soc. Am.), 220–256.

Weaver, P.P.E., Searle, R.C., and Kuijpers, A., 1986. Turbidite deposition and the origin of the Madeira Abyssal Plain. *In* Summerhayes, C.P., and Shackleton, N.J. (Eds.), *North Atlantic Palaeoceanography.* Spec. Publ. Geol. Soc. London, 21:131–143.

Whitmarsh, R.B., Beslier, M.-O., Wallace, P.J., et al., 1998. *Proc. ODP, Init. Repts.,* 173: College Station, TX (Ocean Drilling Program).

Wise, S.W., Jr., and van Hinte, J.E., 1987. Mesozoic-Cenozoic depositional environments revealed by Deep-Sea Drilling Project Leg 93 drilling on the continental rise off the Eastern United States: cruise summary. *In* van Hinte, J.E., Wise, S.W., Jr., et al., *Init. Repts. DSDP,* 93 (Pt. 2): Washington (U.S. Govt. Printing Office), 1367–1423.

Zhao, X., Milkert, D., Liu, L., and Kanamatsu, T., 1996. Magnetostratigraphy of Cenozoic sediments recovered from the Iberia Abyssal Plain. *In* Whitmarsh, R.B., Sawyer, D.S., Klaus, A., and Masson, D.G. (Eds.), *Proc. ODP, Sci. Results,* 149: College Station, TX (Ocean Drilling Program), 315–334.

Zhao, X., Roperch, P., and Stokking, L., 1994. Magnetostratigraphy of the North Aoba Basin. *In* Greene, H.G., Collot, J-Y., Stokking, L.B., et al., *Proc. ODP, Sci. Results,* 134: College Station, TX (Ocean Drilling Program), 457–474.

Zijderveld, J.D.A., 1967. AC demagnetization of rocks: analysis of results. *In* Collinson, D.W., Creer, K.M., and Runcorn, S.K. (Eds.), *Methods in Palaeomagnetism:* New York (Elsevier), 254–286.

Figure F1. Contoured regional bathymetric chart of the western Iberia margin. Contours are at 500-m intervals. The rectangular inset in the center of the chart shows the locations of Leg 149 (solid circle) and Leg 173 (solid triangles with bold numbers) sites. J = magnetic anomaly J. PS, VS, and VdG = Porto, Vigo, and Vasco da Gama Seamounts, respectively. ES = Estremadura Spur. Solid circles outside the inset = sites drilled during earlier legs. Solid squares and crosses = rock samples obtained by submersible and dredge, respectively. Diamonds = the location of the crest of the peridotite ridge. The top inset is a composite of seismic tracks showing the relative locations of Leg 149, Leg 173, and other drill sites.

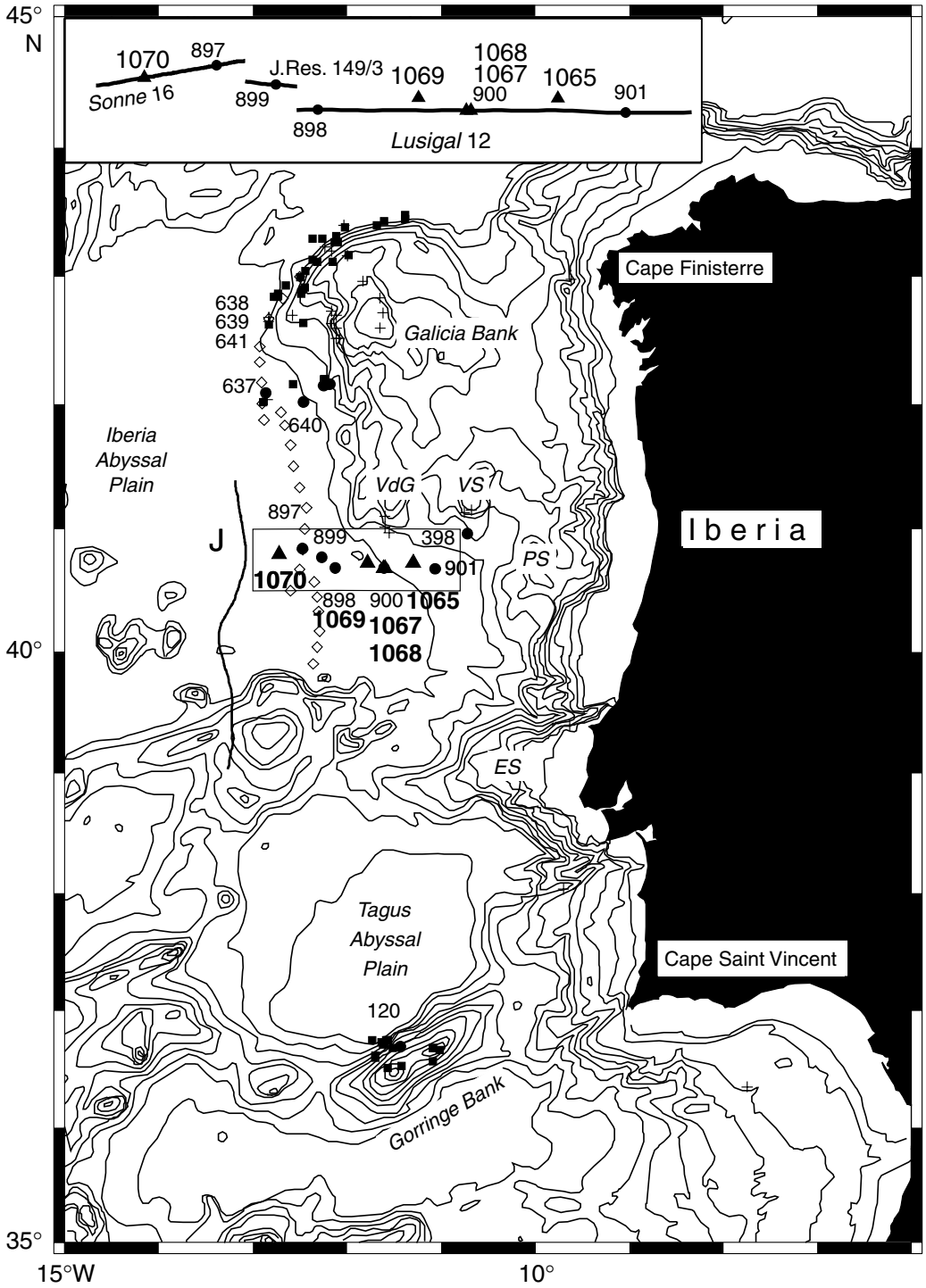

Figure F2. Simplified summaries of stratigraphic successions cored at Leg 149 and Leg 173 sites. * = a wash core recovered Miocene nannofossil ooze and a 5-mm-thick layer of gray clay of Aptian age. Solid square = nannofossil pelagites dominate at Site 900. Solid circles = "motifs"; refers to types of upward-darkening sequences shown in the "Site 1068" (Shipboard Scientific Party, 1998b) and "Site 1069" (Shipboard Scientific Party, 1998c) chapters of the Leg 173 *Initial Results* volume. The cross-hatched symbols on the summary chart indicate that both thin (Motif 2) and thick (Motif 1) sequences are present (Whitmarsh, Beslier, Wallace, et al., 1998).

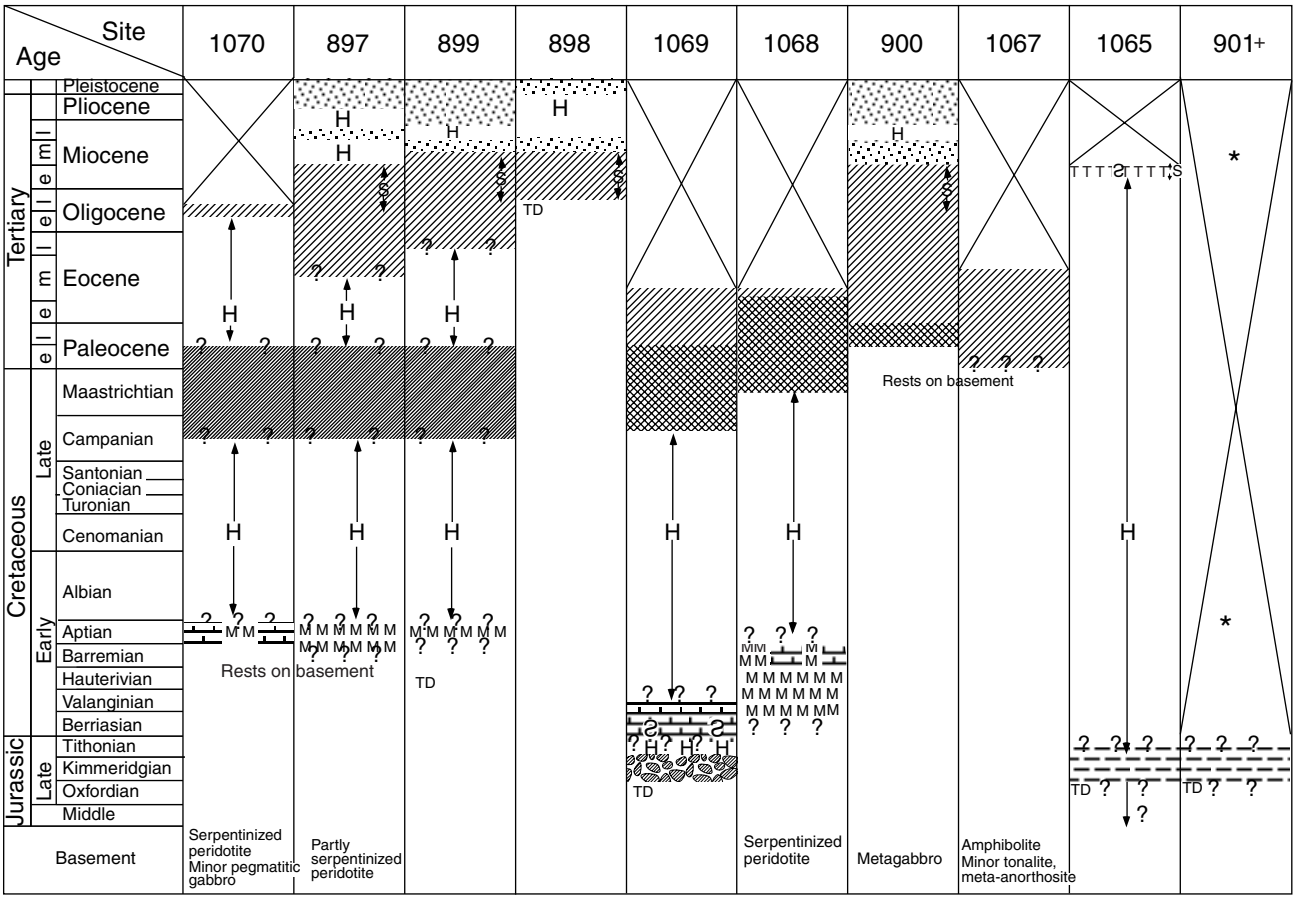

	Lithostratigraphic unit		Lithostratigraphic unit
Siliciclastic turbidites and nannofossil pelagites▪	I	Nannofossil chalk	IV
Nannofossil chalk	II	Mass-flow deposits: Olistostromes (Sites 897, 899) Serpentinite breccias (Sites 1070, 899) Amphibolite, etc. breccias (Site 1068)	IV
Thin motifs• (5-15 cm) Thick motifs• (15-100 cm) Carbonate turbidites and noncarbonate hemipelagites	II	Metasediment and shallow-water limestone pieces (? clasts)	V
S Siliceous allochems	II	Clay, and claystone with thin sandstones and conglomerates	V
Red-brown claystones (with sandstones and conglomerates at base at Sites 897, 899)	III		

Not cored ƨ Slumps H Hiatus TD Total depth *, +, •, ▪ See caption

Figure F3. Remanent magnetization before and after 15-mT AF demagnetization as a function of subbottom depth. (**A**) Intensity and (**B**) inclination of archive halves and discrete samples from Section 149-897C-61R-1 are shown. The NRM inclinations are biased toward high positive inclinations, suggesting that drilling-induced magnetization is present. AF demagnetization to 15 mT can effectively remove this drilling-induced magnetization, as indicated by changes in inclination and intensity.

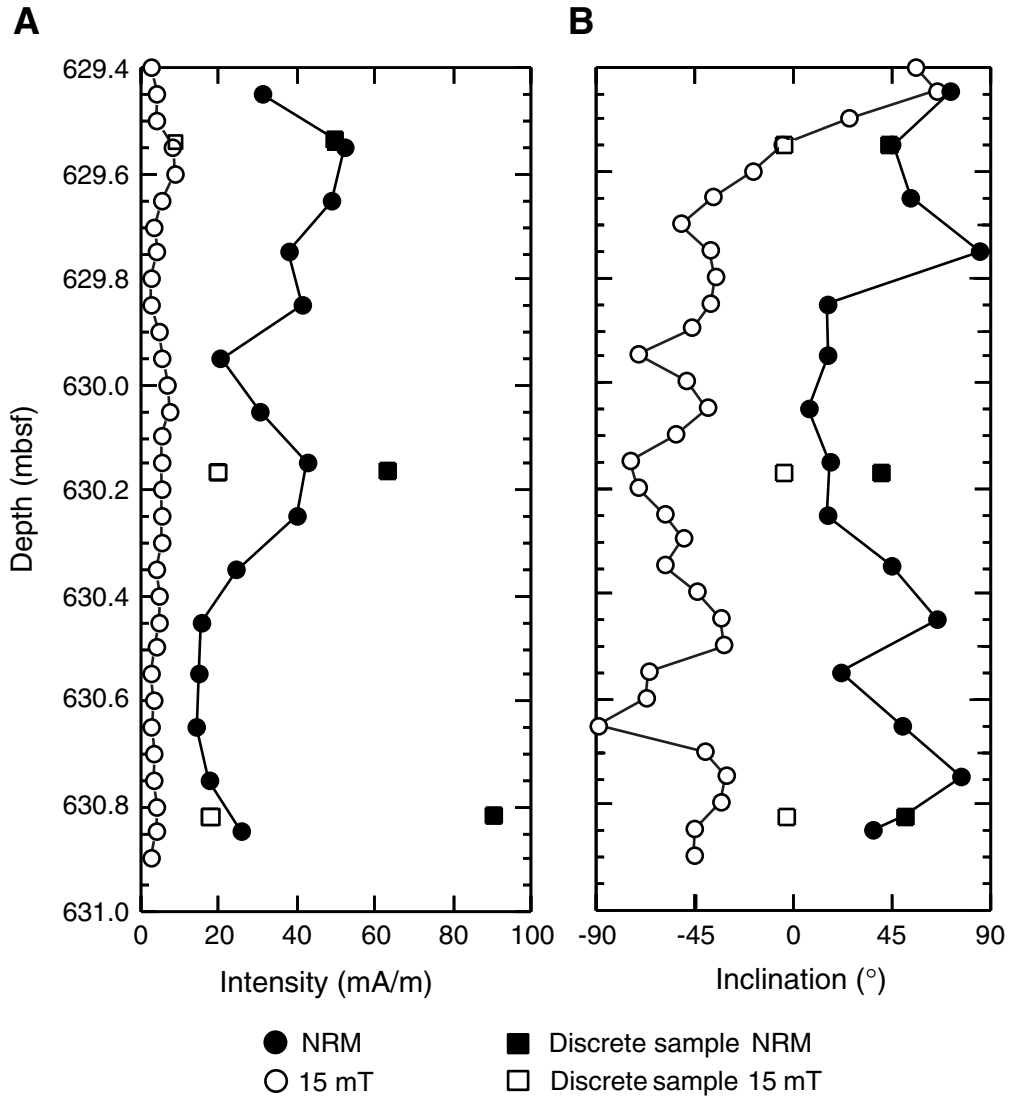

Figure F4. Representative vector end point diagrams showing the results of thermal and AF demagnetization for samples of nannofossil clay and nannofossil ooze. Crosses and circles = projection of the magnetization vector end point on the horizontal and vertical planes, respectively. Sample (**A**) 149-900A-14R-1, 15–17 cm, shows the removal of a normal component of magnetization close to the present geomagnetic field inclination and isolation of a more stable reversed component that is univectorially decaying toward the origin of the vector plot and (**B**) 149-900A-10R-2, 35–37 cm, exhibits a reversed secondary component before isolation of the more stable normal polarity of ChRM. (Continued on next page.)

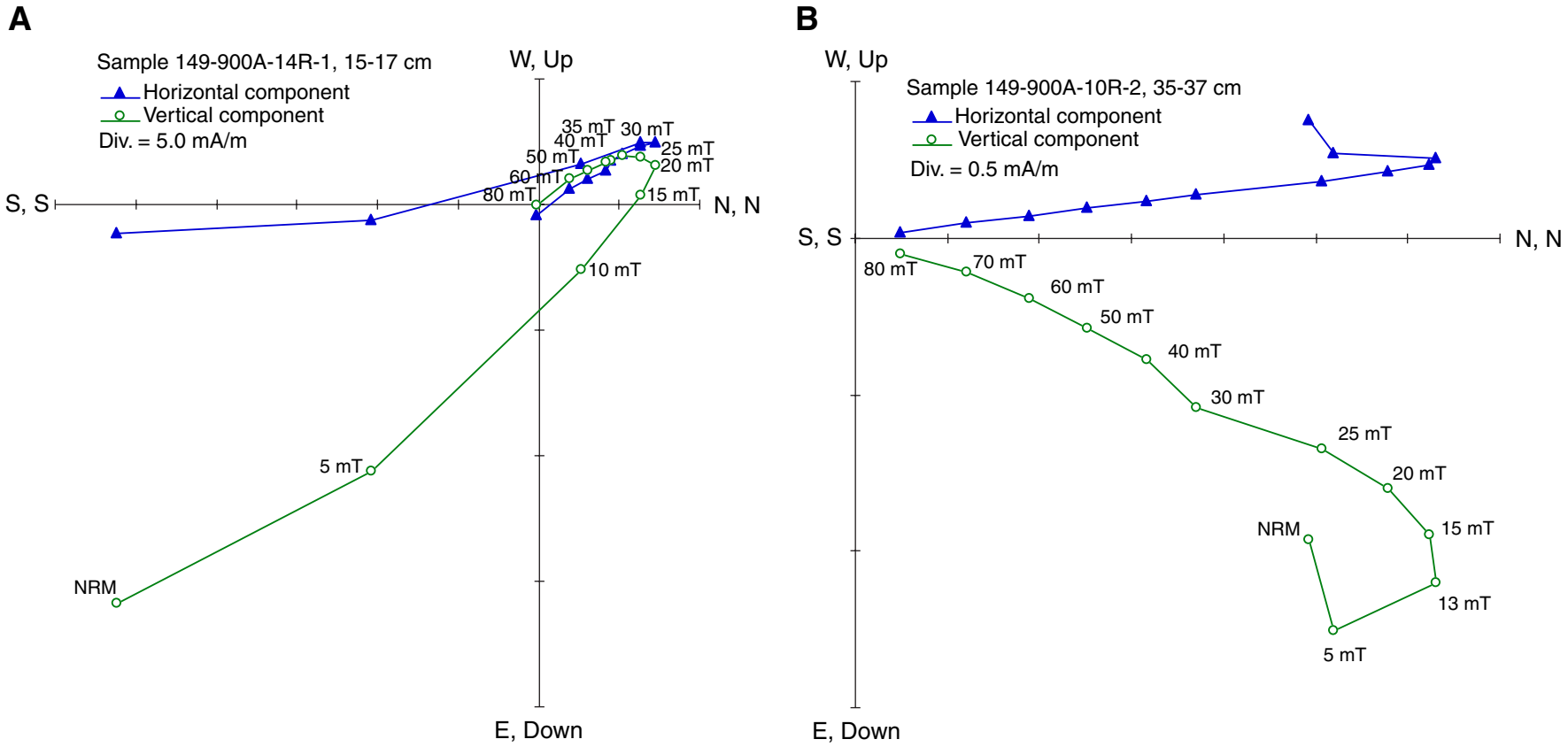

Figure F4 (continued). Demonstrations of the demagnetization behavior of samples during thermal demagnetization. Sample (C) 149-900A-49R-2, 60–62 cm, shows normal polarity of ChRM and (D) 149-900A-49R-7, 26–28 cm, shows reversed polarity of ChRM.

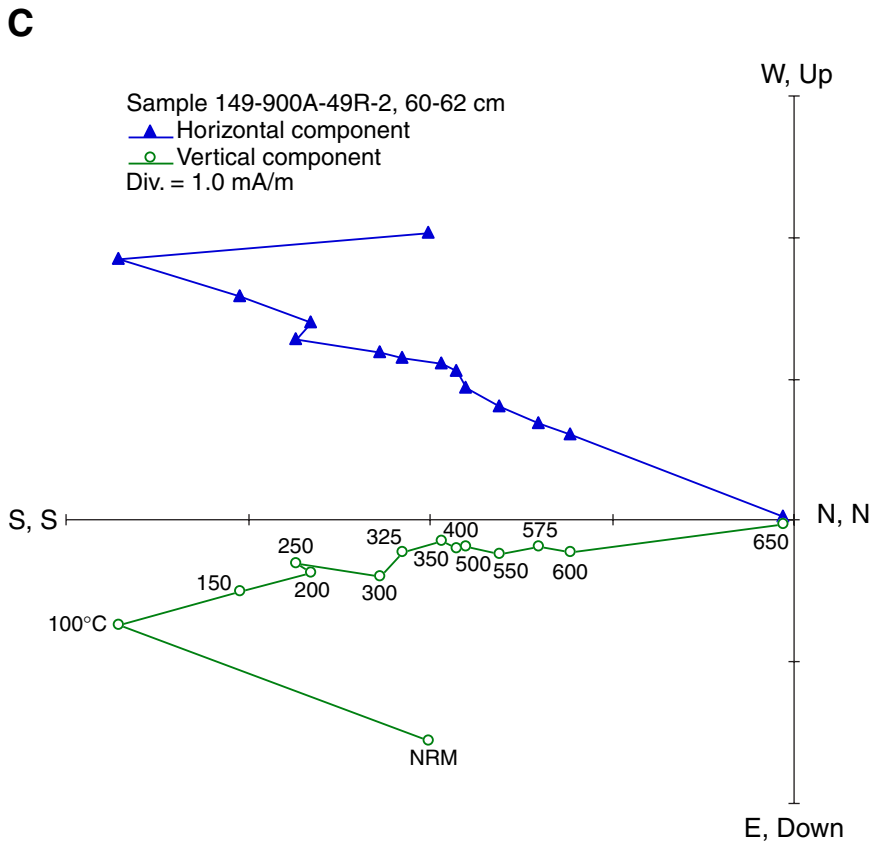

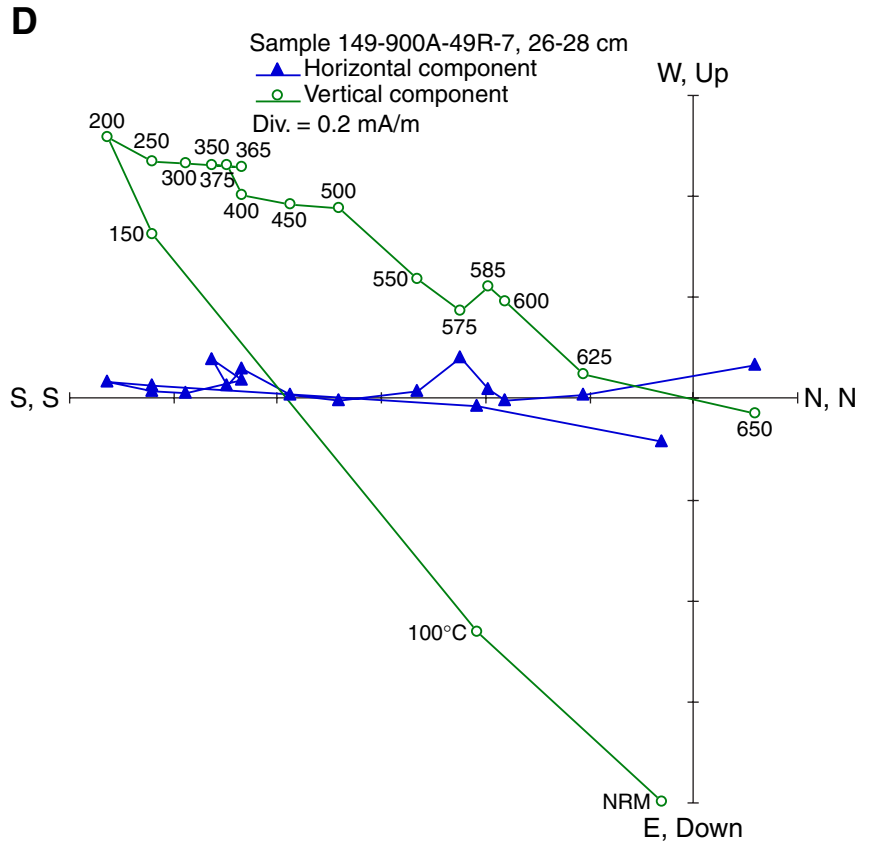

Figure F5. Representative vector end point diagrams showing the results of AF demagnetization for Samples (**A**) 149-900A-10R-4, 7–9 cm, and (**B**) 149-900A-10R-4, 139–141 cm. Crosses and circles = projection of the magnetization vector end point on the horizontal and vertical planes, respectively. Note that both samples were taken from same piece of continuous core section, and, after demagnetization at 40 mT, the reversal indicated by the difference in polarity of inclination is confirmed by the nearly 180° declination, adding confidence to the polarity determination.

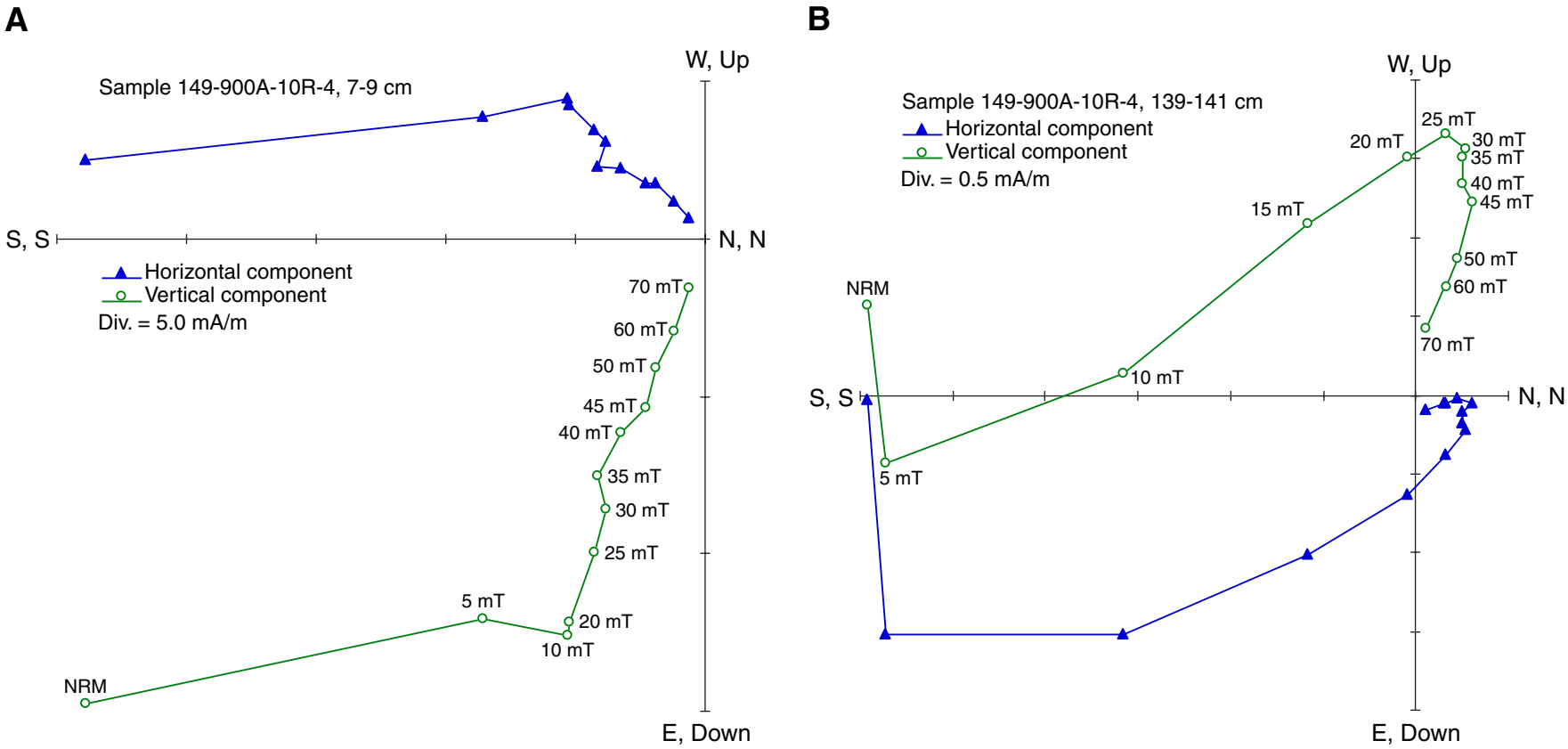

Figure F6. Representative hysteresis loop for samples showing hematite. Data is after slope correction (1 emu = 10^{-3} Am^2, SI).

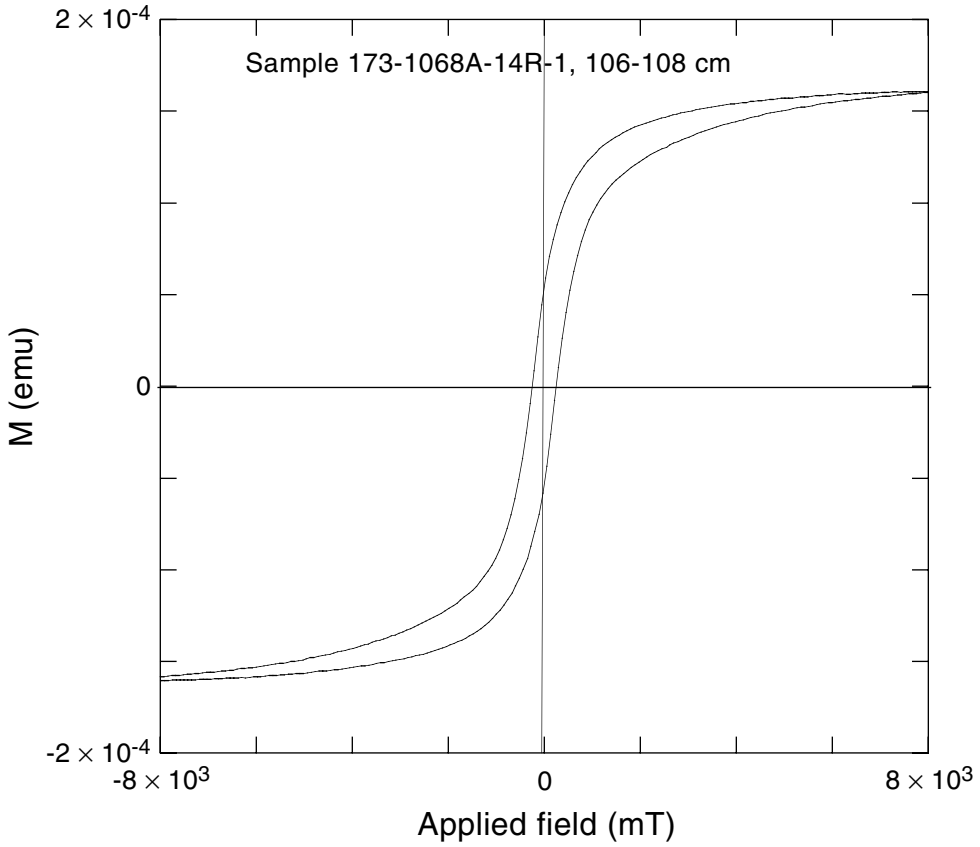

Figure F7. Representative vector end point diagrams showing the results of AF demagnetization for samples from Site 897. Crosses and circles = projection of the magnetization vector end point on the horizontal and vertical planes, respectively. Sample (**A**) 149-897C-4R-1, 34–36 cm, shows normal polarity and (**B**) 149-897C-11R-6, 37–39 cm, shows reversed polarity of ChRM.

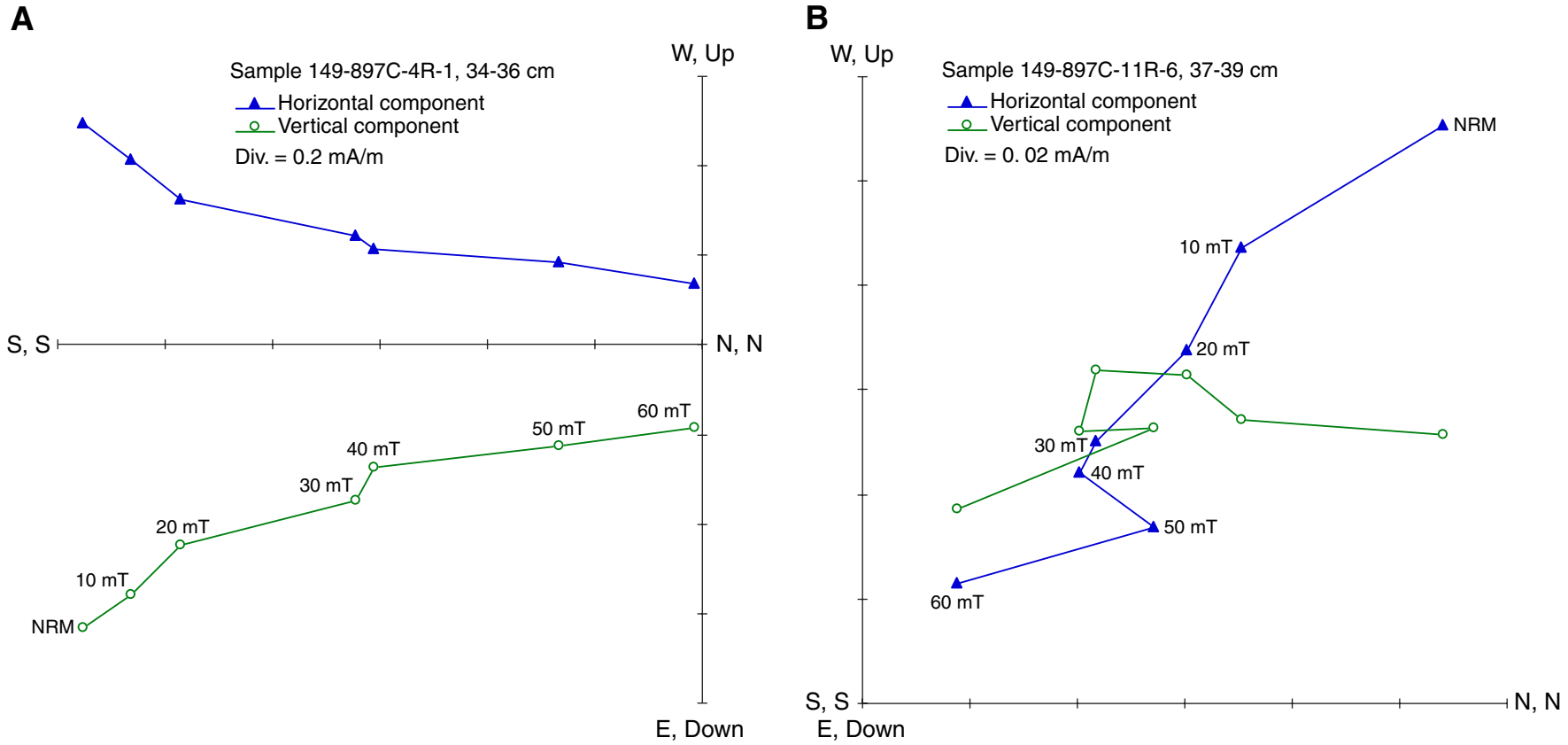

Figure F8. Downhole variation of stable magnetic inclination, inferred polarity, and biostratigraphic zones for Cenozoic sediments at Site 897. Black bands = normal polarity, white bands = reversed polarity.

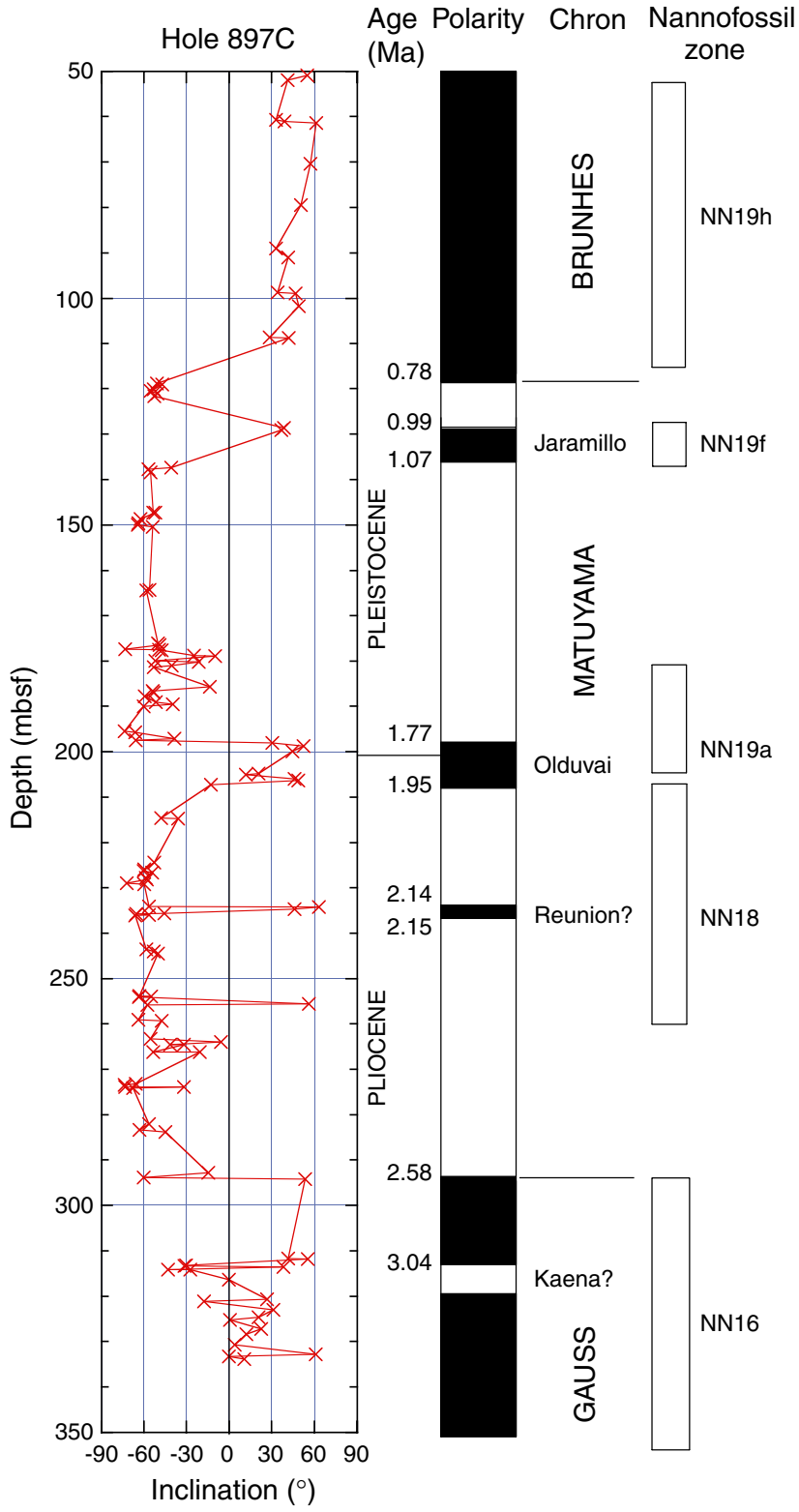

Figure F9. Depth vs. age curve for Hole 897C. The paleomagnetic data points are listed in Table T2, p. 57. Note the short hiatus or a decrease in sedimentation rate inferred within the interval 1.77–1.95 Ma.

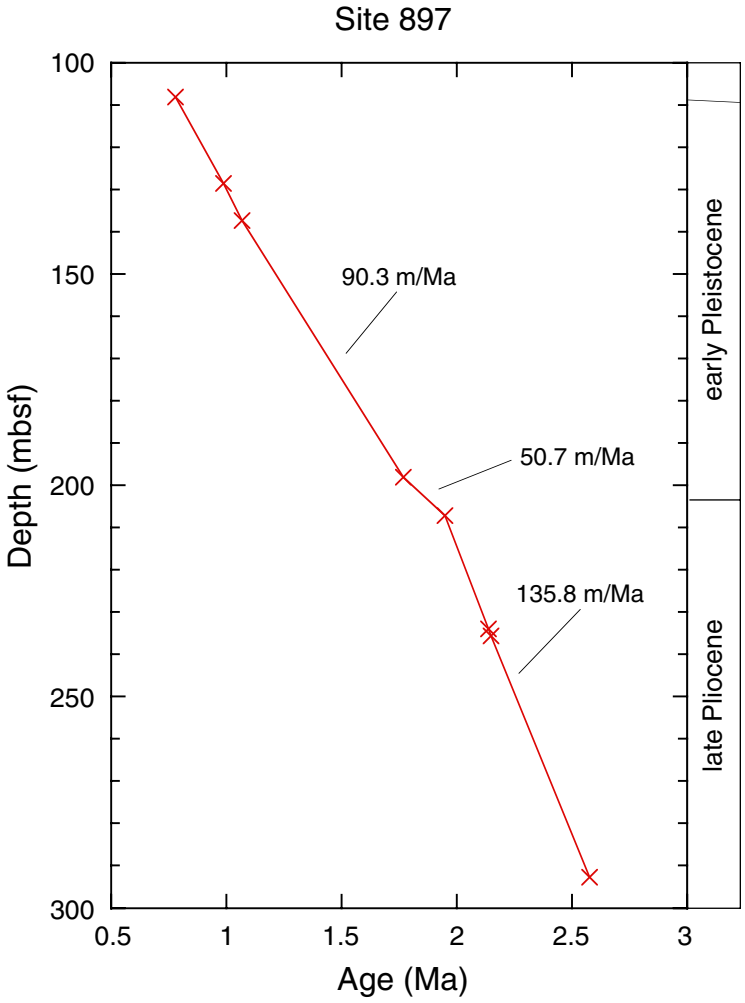

Figure F10. Representative vector end point diagrams showing the results of AF demagnetization for samples from Site 898. Crosses and circles = projection of the magnetization vector end point on the horizontal and vertical planes, respectively. Samples (**A**) 149-898A-2H-4, 15–17 cm, and (**B**) 149-898A-3H-3, 52–54 cm, show normal polarity of ChRM. (Continued on next page.)

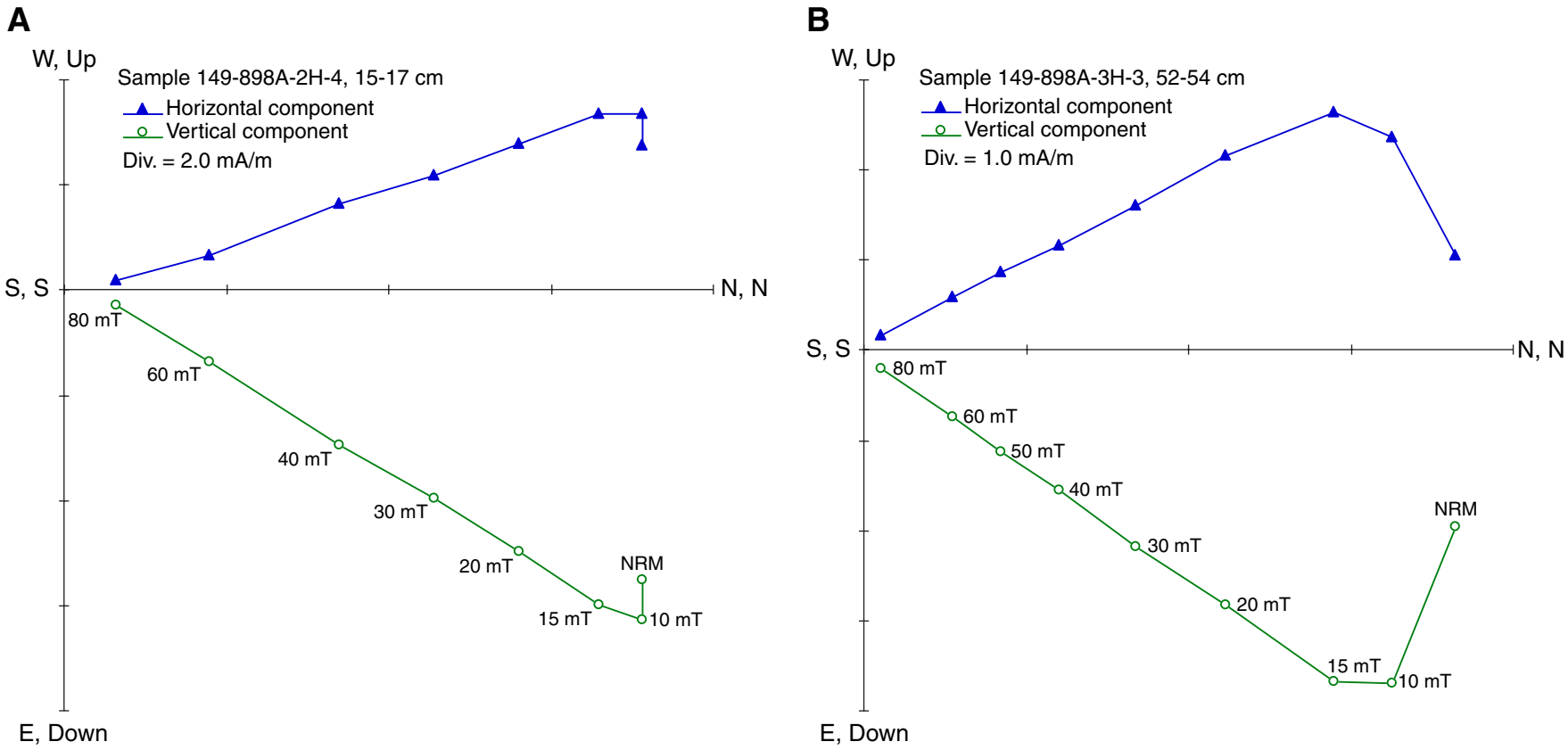

Figure F10 (continued). Samples (**C**) 149-898A-4H-6, 89–91 cm, and (**D**) 149-898A-5H-2, 10–12 cm, show reversed polarity of ChRM.

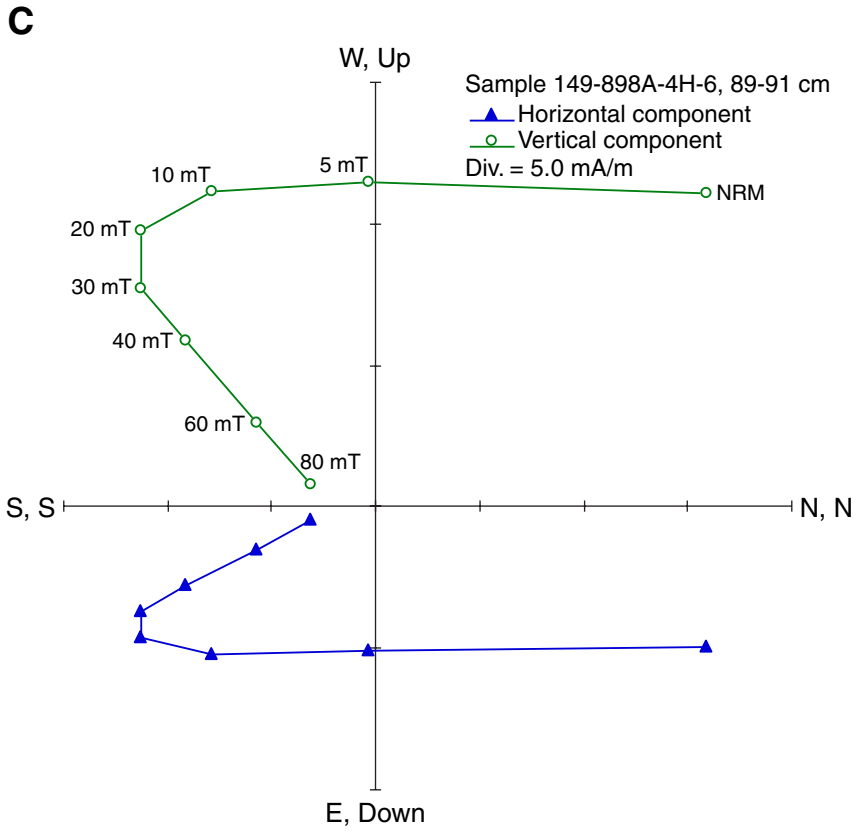

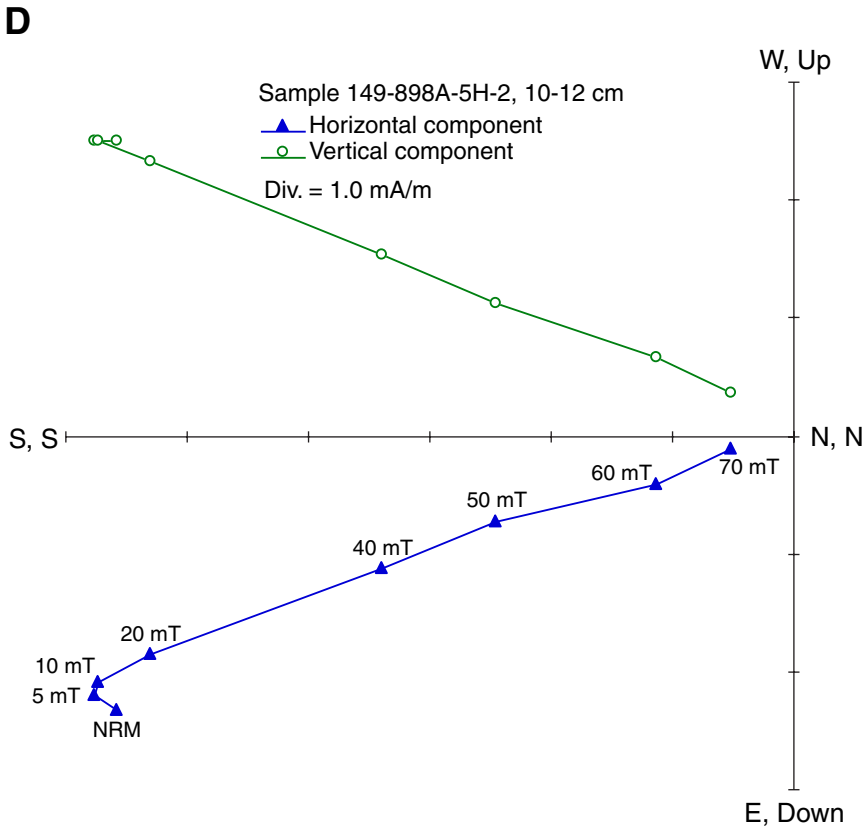

Figure F11. Downhole variation of stable magnetic inclination, inferred polarity, and biostratigraphic zones for Cenozoic sediments at Site 898. Black bands = normal polarity, white bands = reversed polarity.

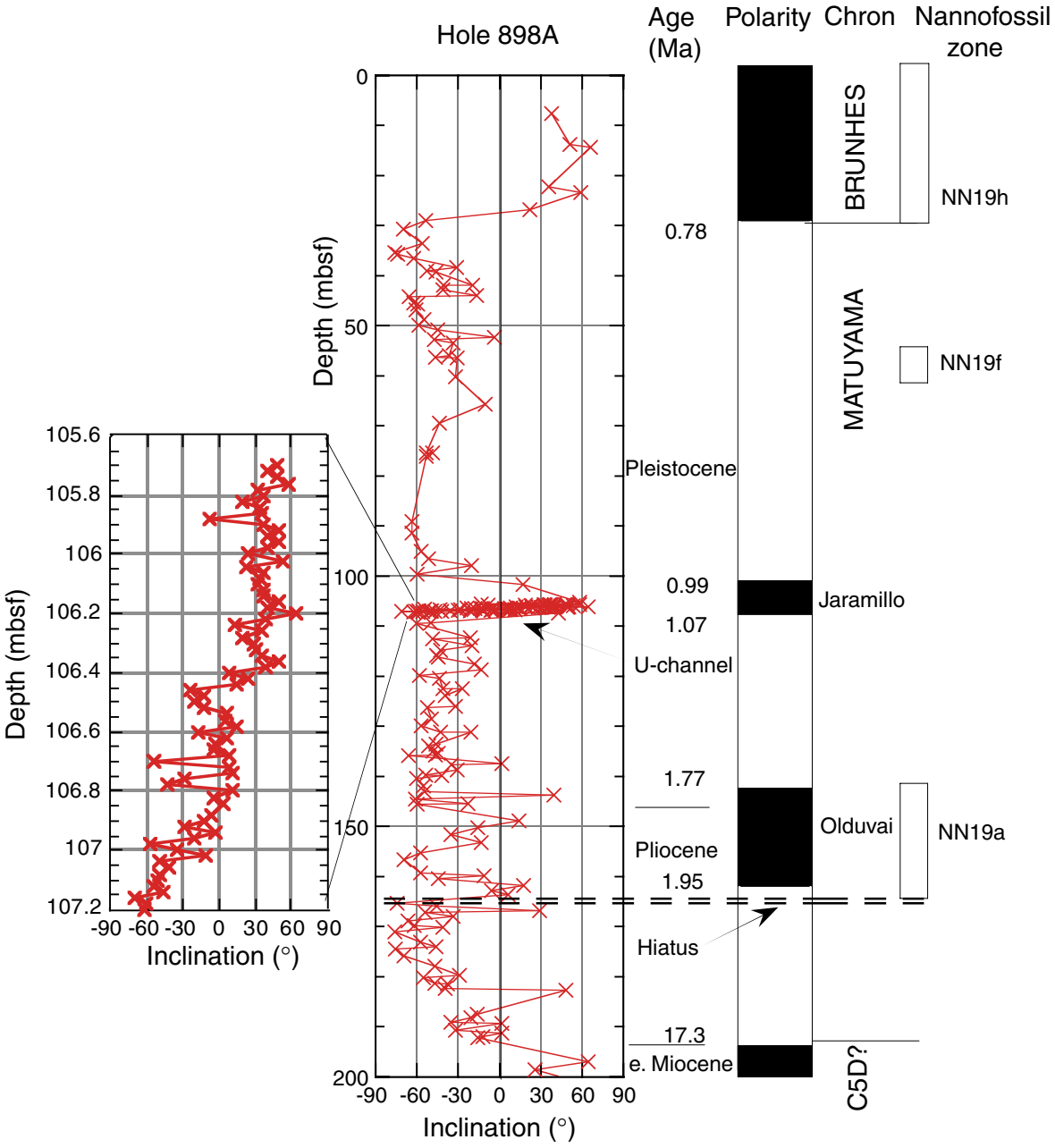

Figure F12. Depth vs. age curve for Hole 898A. The paleomagnetic data points are listed in Table T4, p. 60. Note the short hiatus or a decrease in sedimentation rate again inferred within the interval 1.0–1.8 Ma.

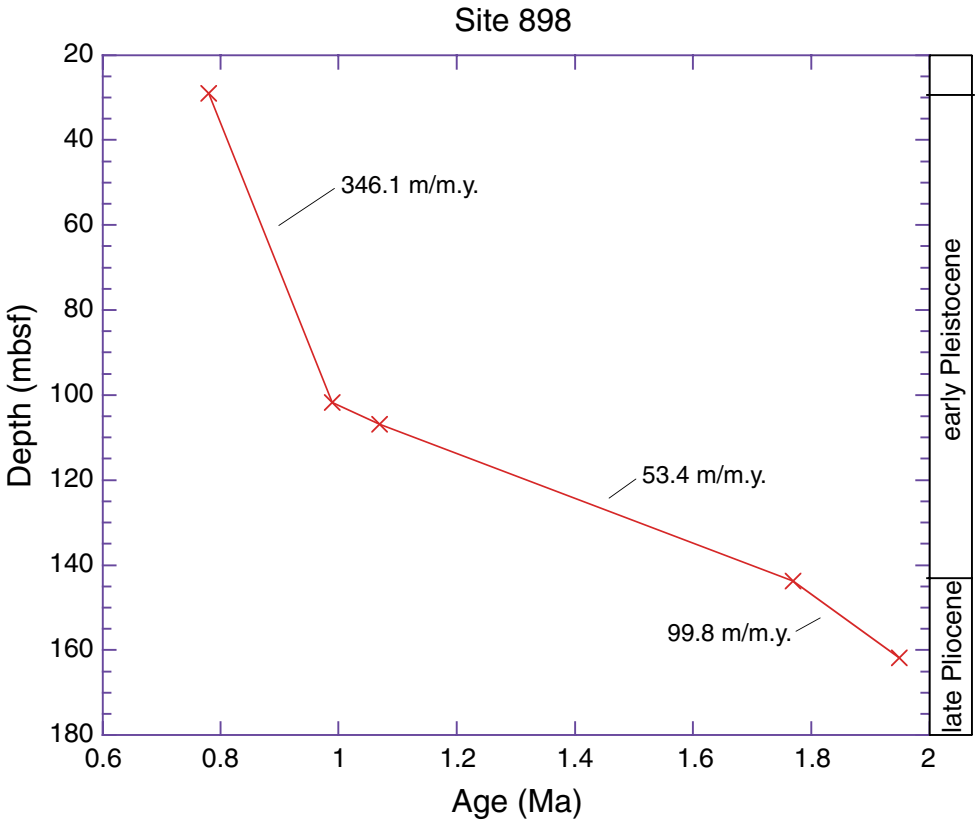

Figure F13. Representative vector end point diagrams showing the results of AF demagnetization for samples from Site 900. Crosses and circles = projection of the magnetization vector end point on the horizontal and vertical planes, respectively. Samples (**A**) 149-900A-9R-3, 35–37 cm, and (**B**) 149-900A-10R-2, 70–72 cm, show normal polarity of ChRM. (Continued on next page.)

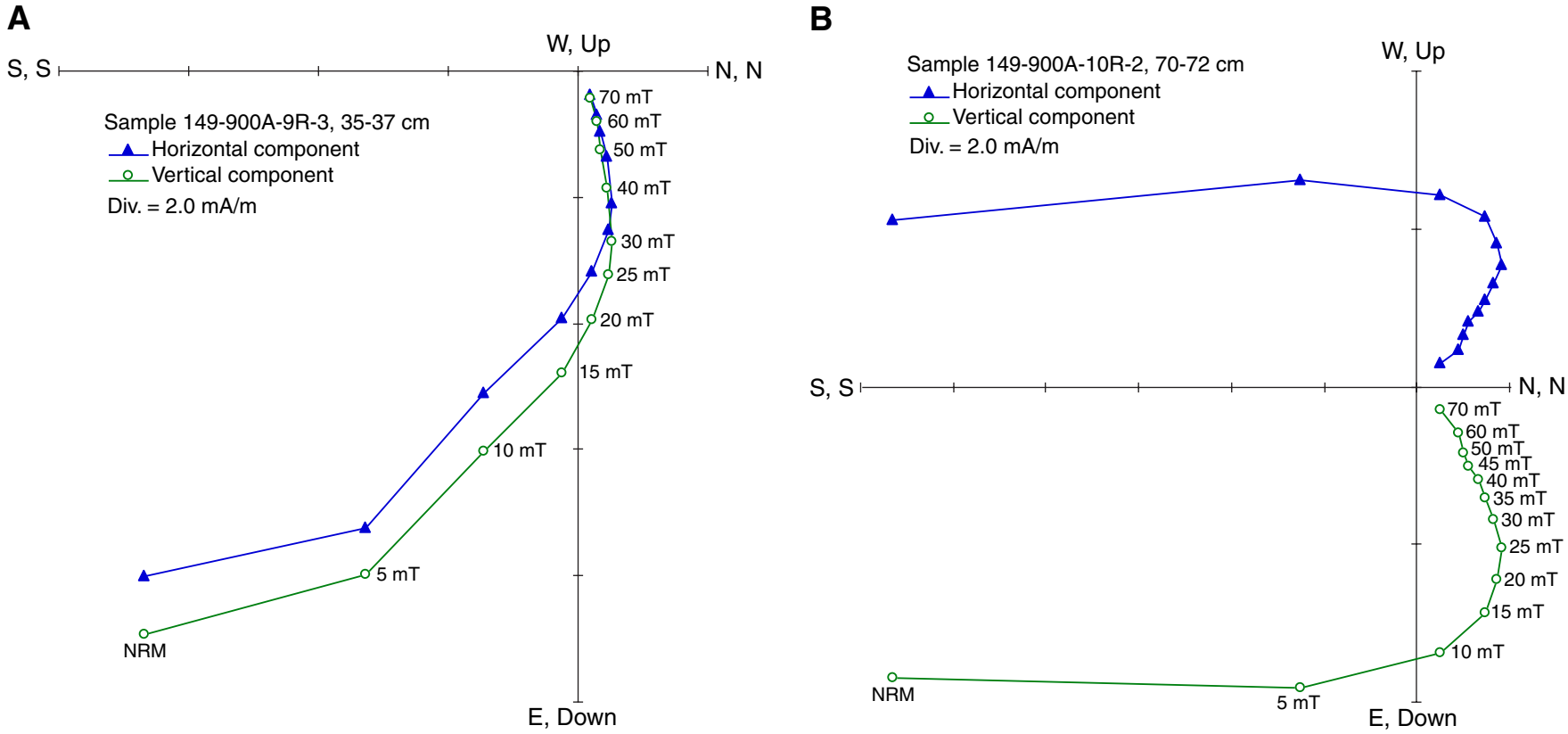

Figure F13 (continued). Samples (**C**) 149-900A-10R-5, 7–9 cm, and (**D**) 149-900A-14R-5, 107–109 cm, show reversed polarity of ChRM.

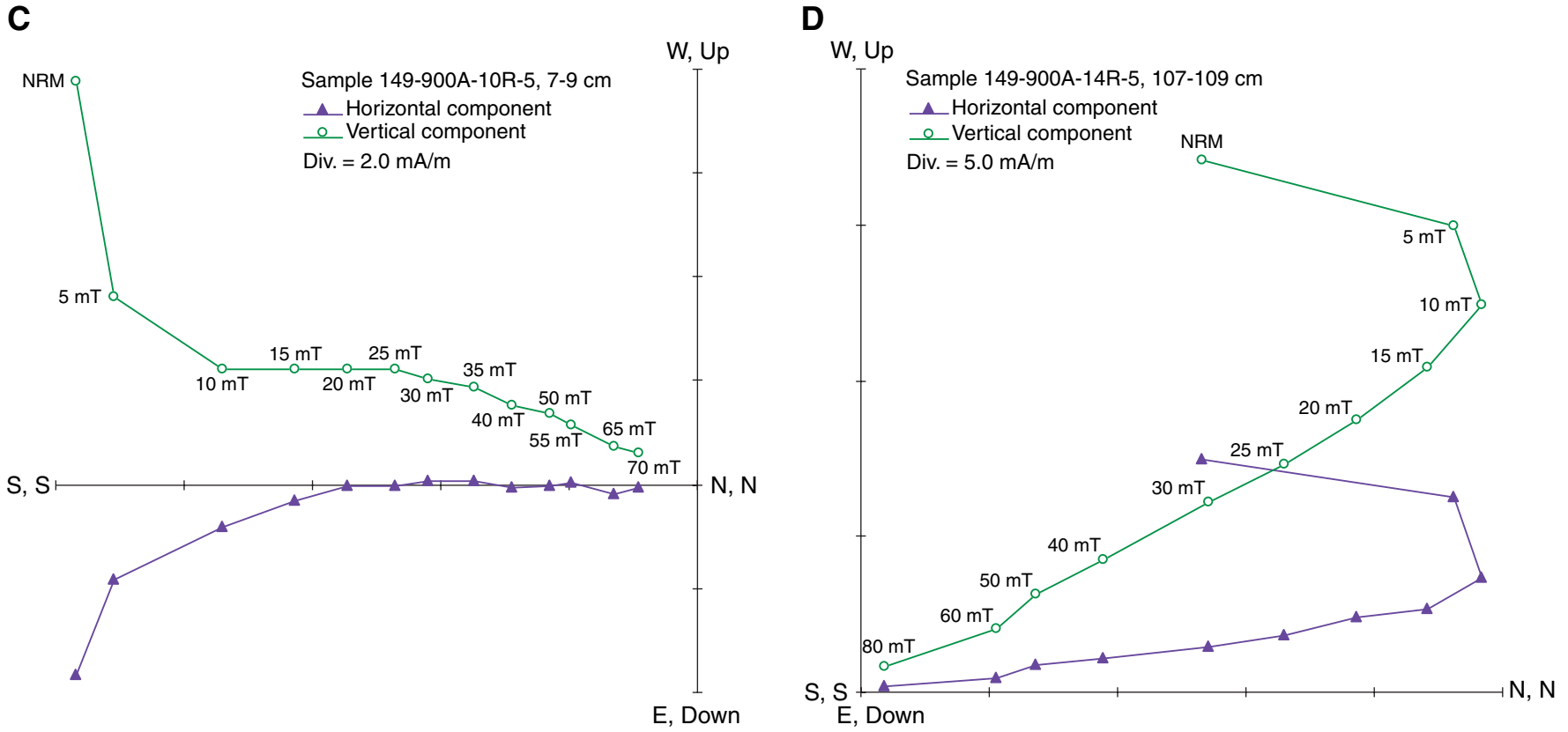

Figure F14. Downhole variation of stable magnetic inclination, inferred polarity, and biostratigraphic zones for Cenozoic sediments at Site 900. Black bands = normal polarity, white bands = reversed polarity.

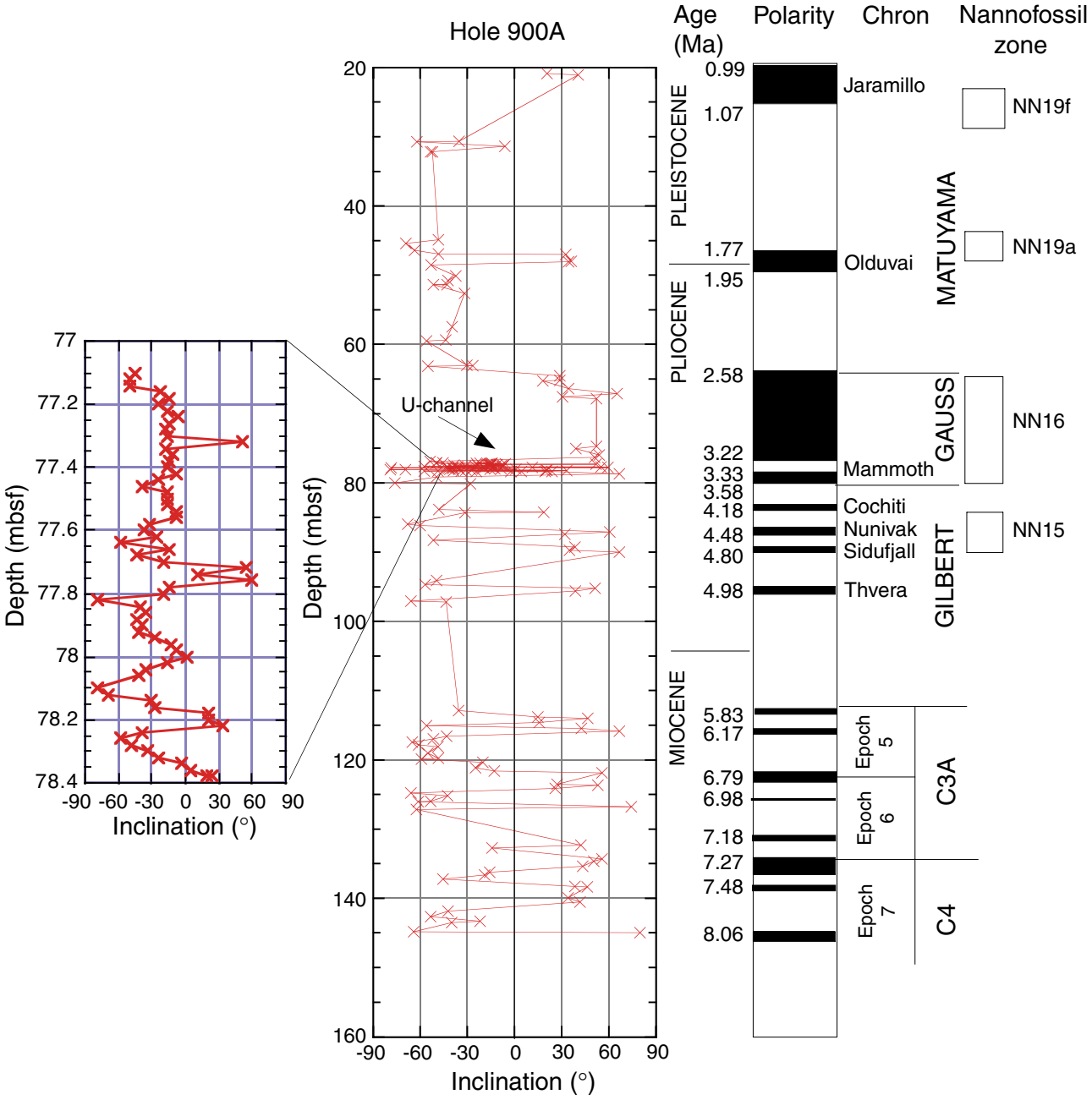

Figure F15. Depth vs. age curve for Hole 900A. The paleomagnetic data points are listed in Table T6, p. 63. At least two sedimentary hiatuses are inferred in this plot: one is close to the Pliocene/Pleistocene boundary in an identical position to that proposed at Sites 897 and 898, and the other is in the interval of 3.58–4.89 Ma at ~85 mbsf, which is close the Pliocene/Miocene boundary. It is important to note the absence of direct paleontological evidence for these hiatuses.

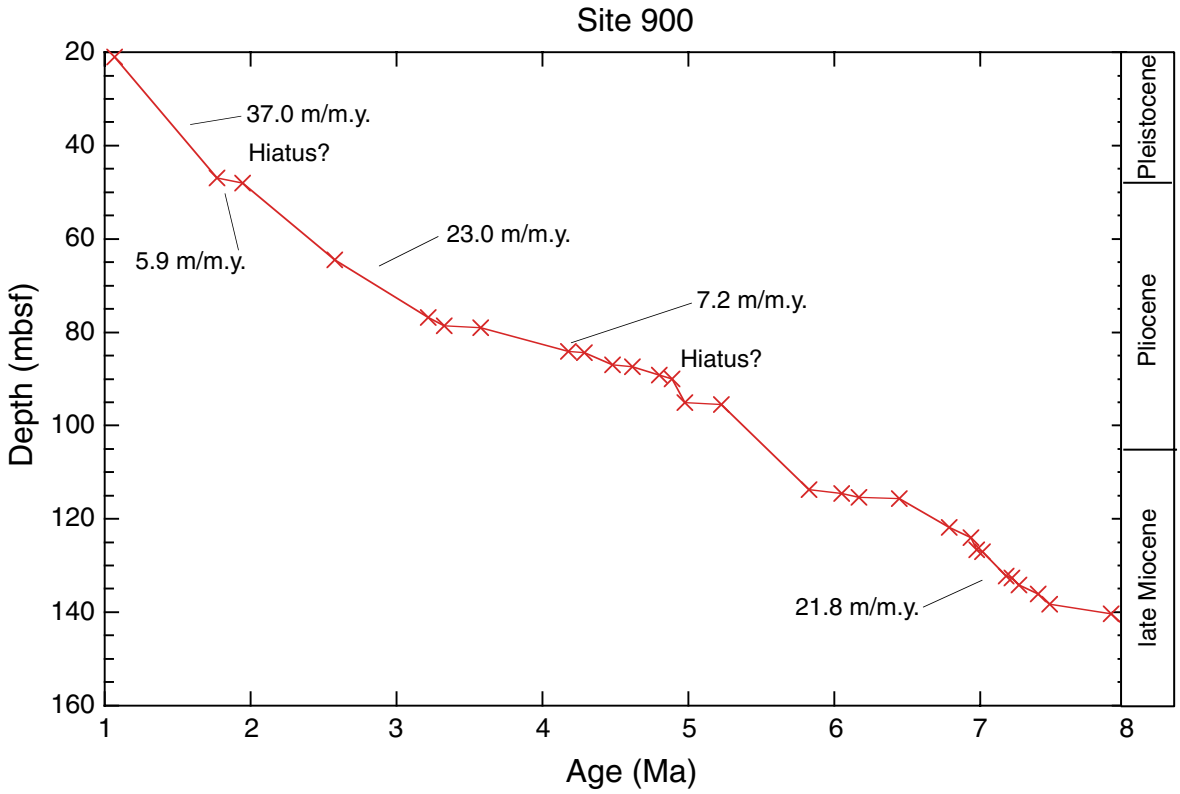

Figure F16. Representative vector end point diagrams showing the results of AF and thermal demagnetization for samples from Site 1067. Crosses and circles = projection of the magnetization vector end point on the horizontal and vertical planes, respectively. Samples (**A**) 173-1067A-10R-1, 113–115 cm, show reversed polarity of ChRM and (**B**) 173-1067A-5R-2, 86–88 cm, show normal polarity of ChRM.

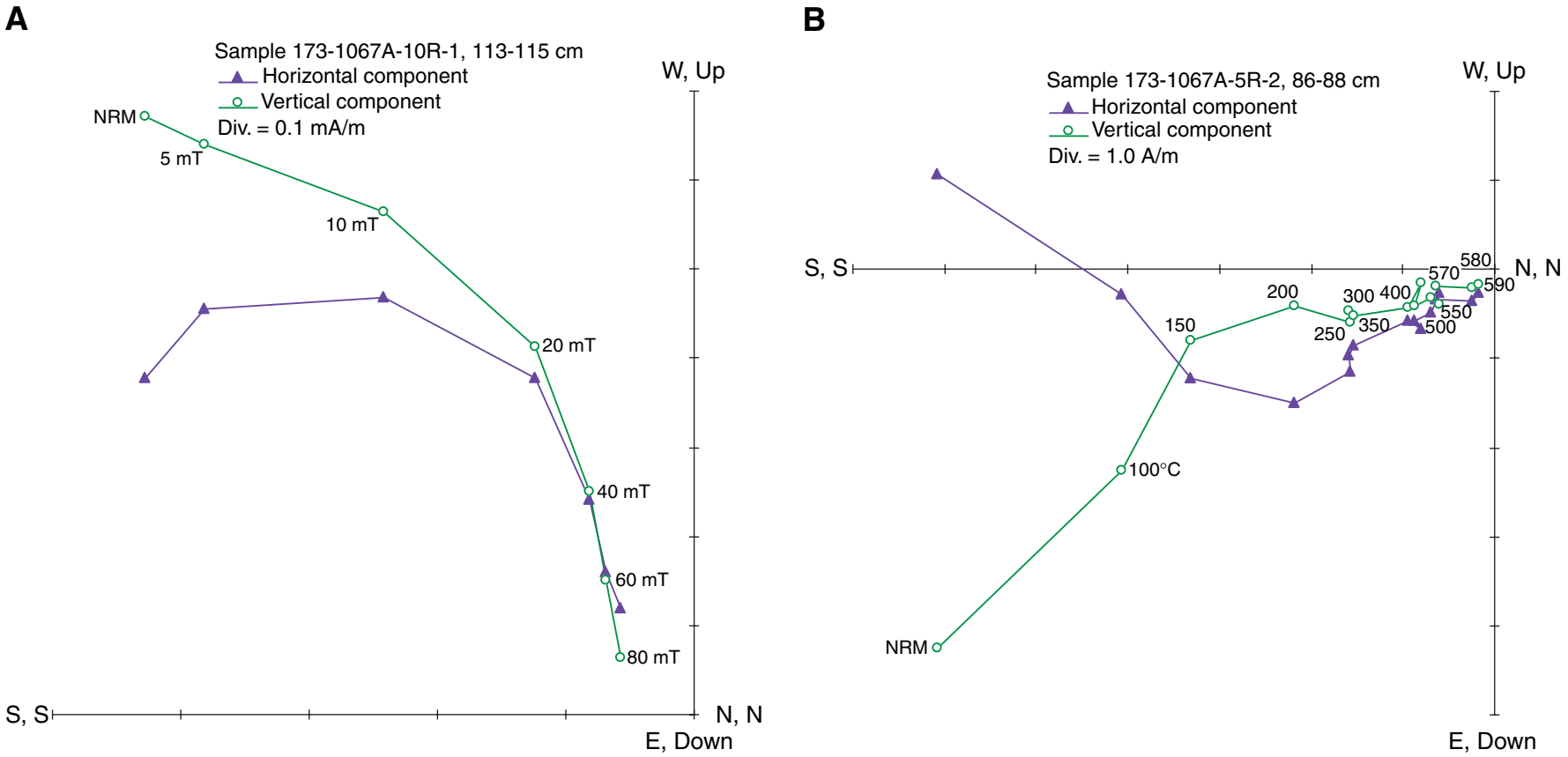

Figure F17. Downhole variation of stable magnetic inclination, inferred polarity, and biostratigraphic zones for Cenozoic sediments at Site 1067. Black bands = normal polarity, white bands = reversed polarity. Question marks = polarity changes are suggested by the pass-through measurements only.

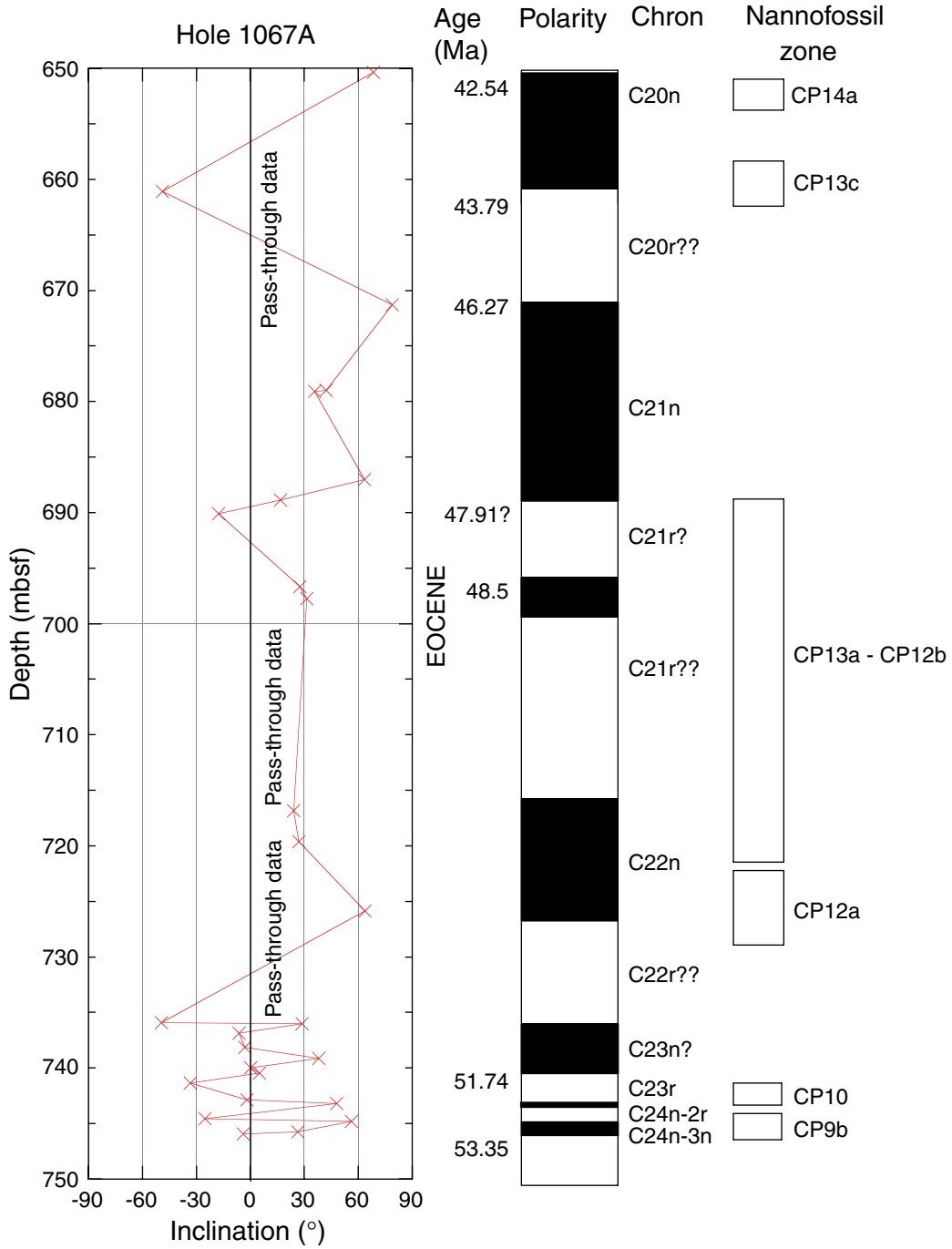

Figure F18. Depth vs. age curve for Hole 1067A. The paleomagnetic data points are listed in Table T9, p. 66. Note the short hiatus or a decrease in sedimentation rate inferred around the Paleocene/Eocene boundary (53 Ma).

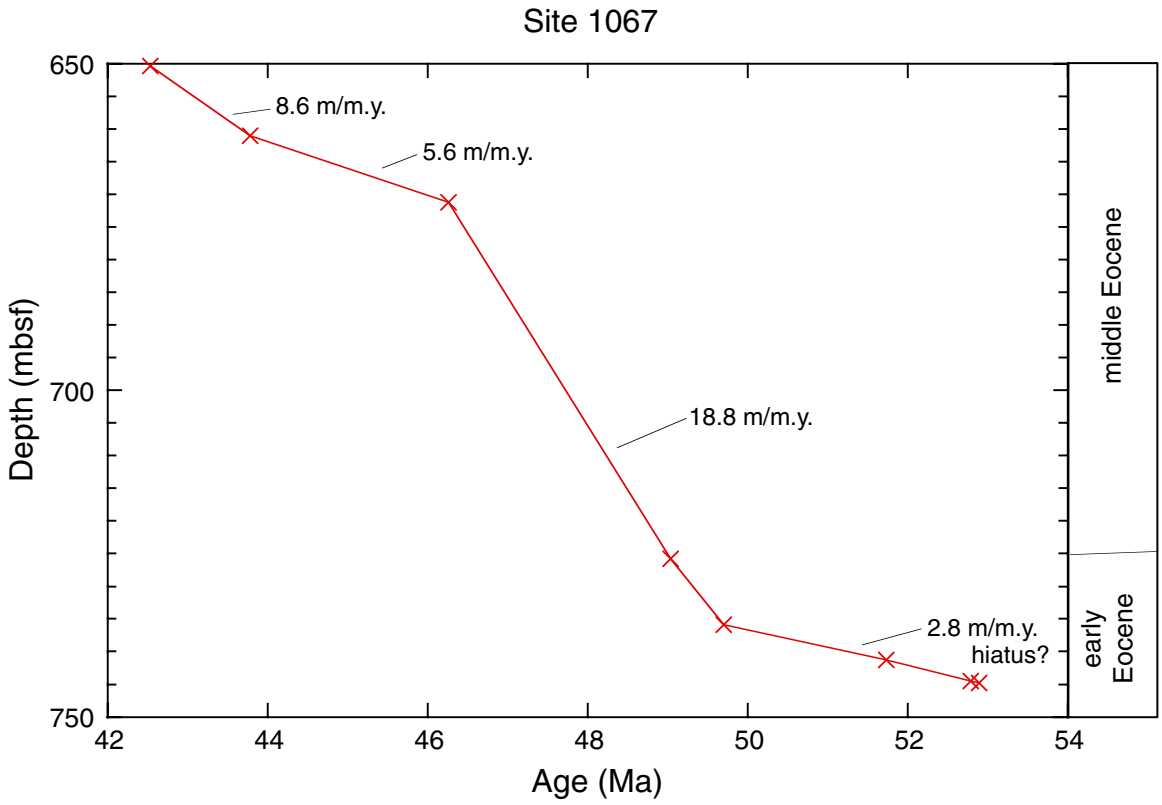

Figure F19. Representative vector end point diagrams showing the results of AF and thermal demagnetization for samples from Site 1068. Crosses and circles = projection of the magnetization vector end point on the horizontal and vertical planes, respectively. Samples (**A**) 173-1068A-6R-4, 60–62 cm, and (**B**) 173-1068A-14R-1, 67–69 cm, show normal polarity of ChRM. (Continued on next page.)

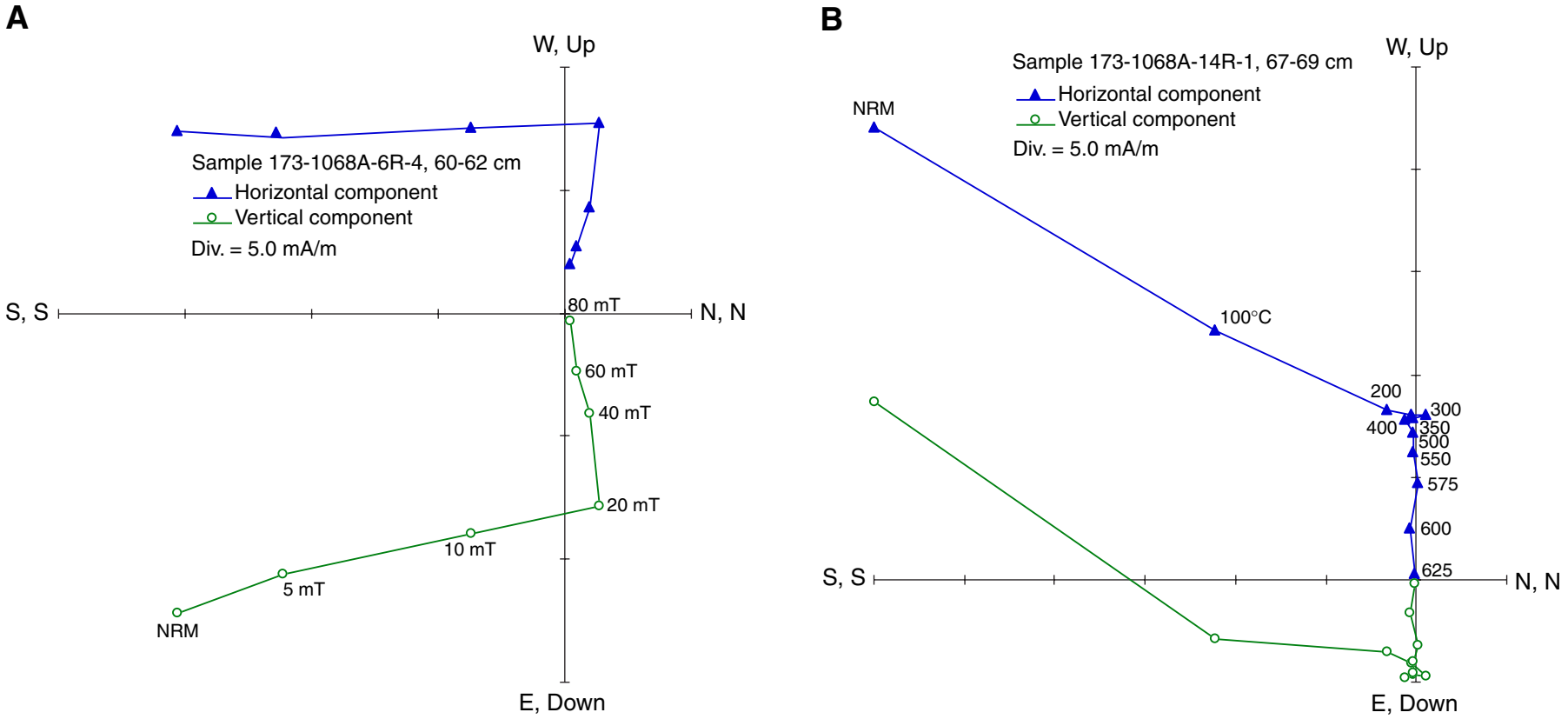

Figure F19 (continued). Samples (**C**) 173-1068A-8R-2, 101–103 cm, and (**D**) 173-1068A-14R -1, 106–108 cm, show reversed polarity of ChRM.

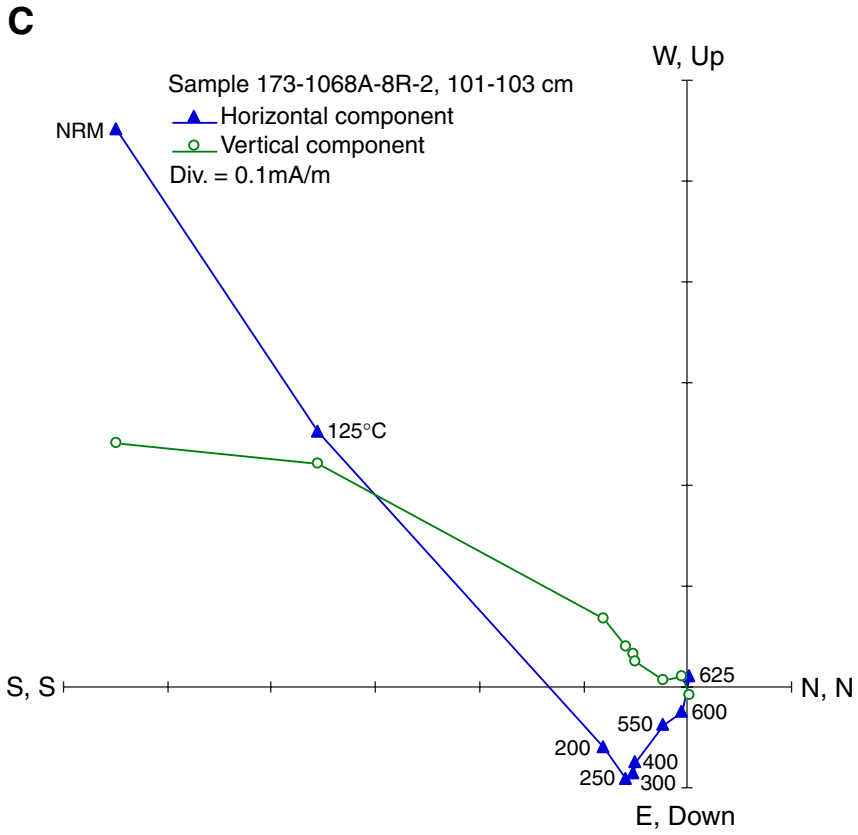

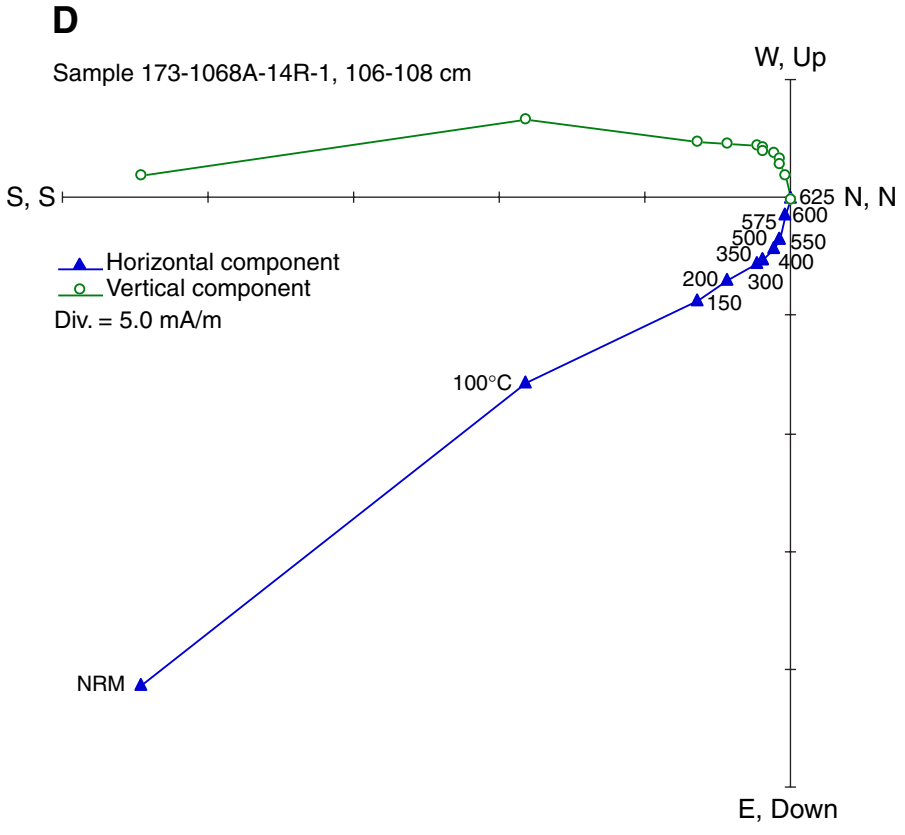

Figure F20. Downhole variation of stable magnetic inclination, inferred polarity, and biostratigraphic zones for Cenozoic sediments at Site 1068. Black bands = normal polarity, white bands = reversed polarity.

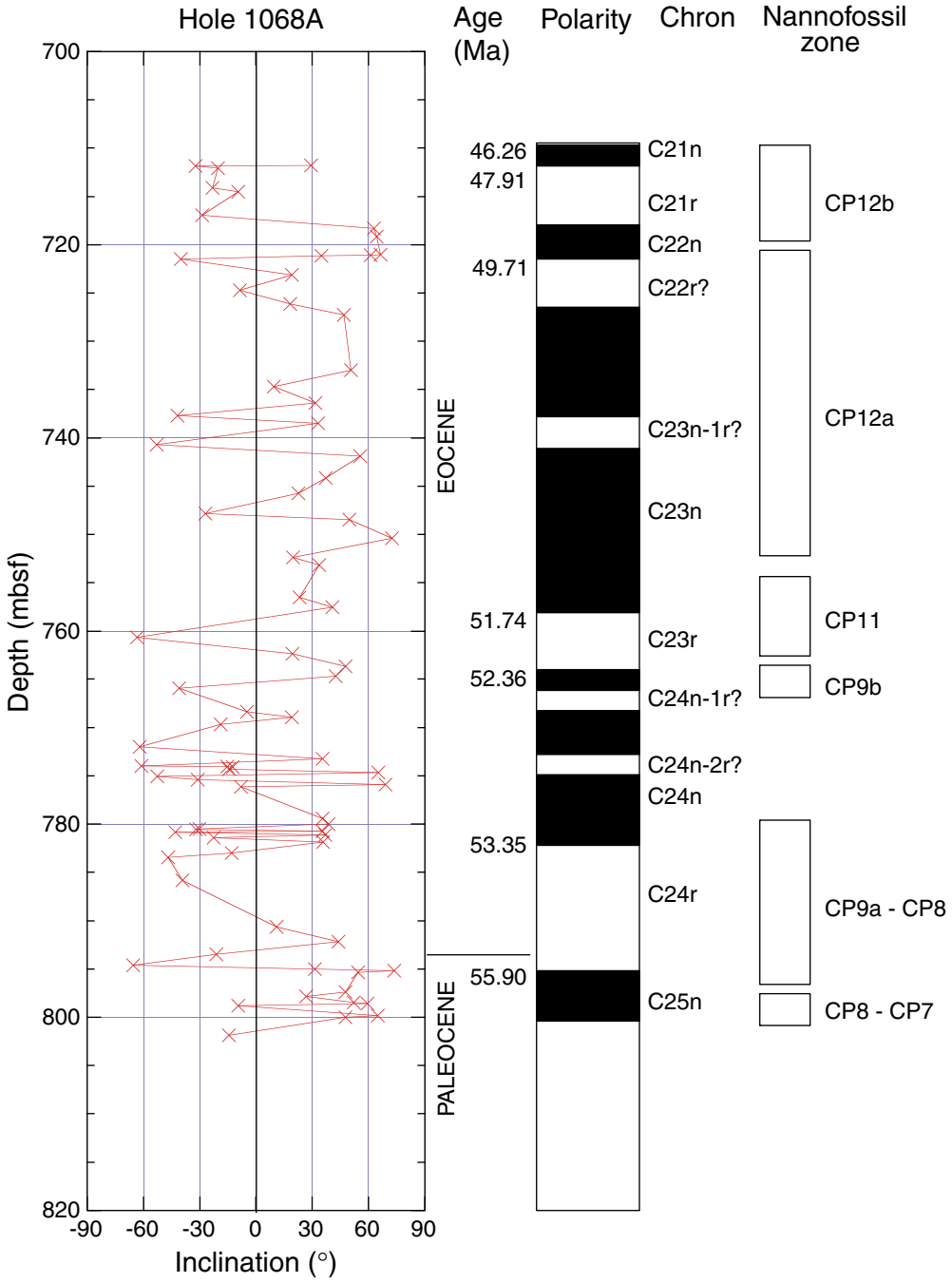

Figure F21. Depth vs. age curve for Hole 1068A. The paleomagnetic data points are listed in Table T11, p. 69. Note the short hiatus or a decrease in sedimentation rate again inferred around the Paleocene/Eocene boundary.

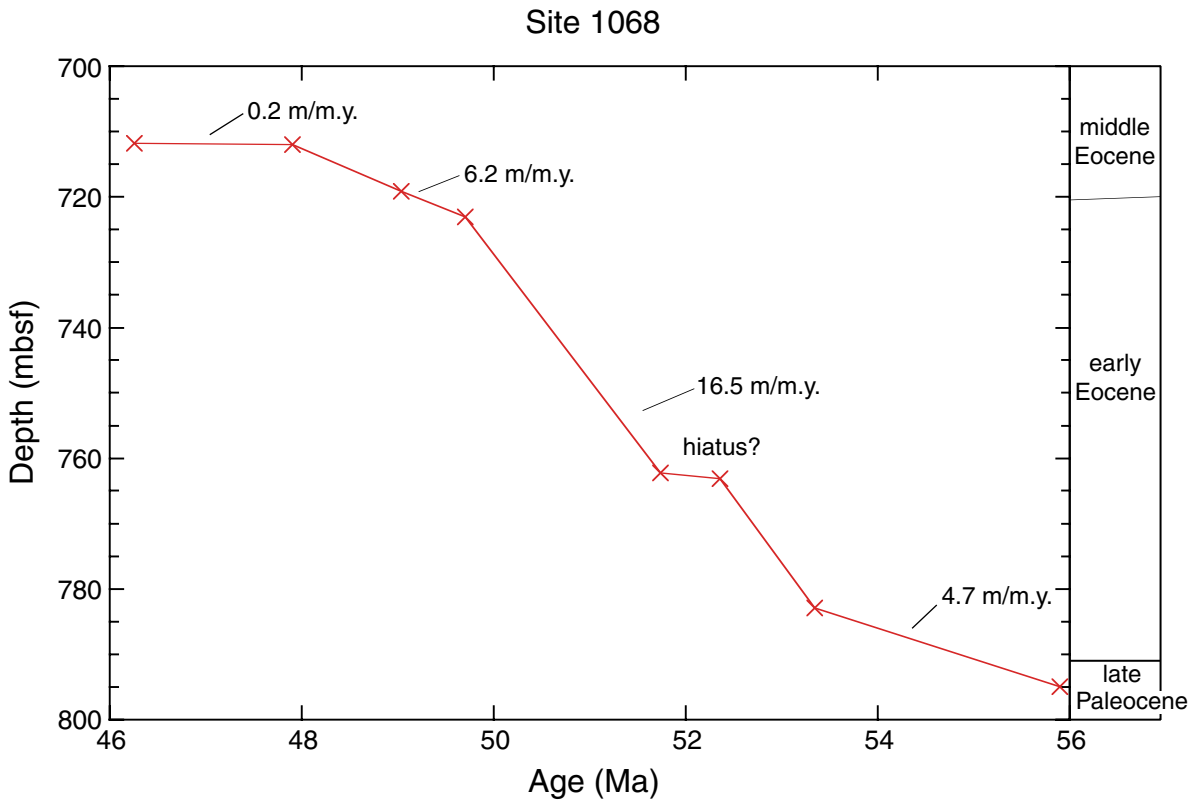

Figure F22. Representative vector end point diagrams showing the results of AF and thermal demagnetization for samples from Site 1069. Crosses and circles = projection of the magnetization vector end point on the horizontal and vertical planes, respectively. Samples (**A**) 173-1069A-2R-2, 116–118 cm, and (**B**) 173-1069A-7R-1, 100–102 cm, show normal polarity of ChRM. (Continued on next page.)

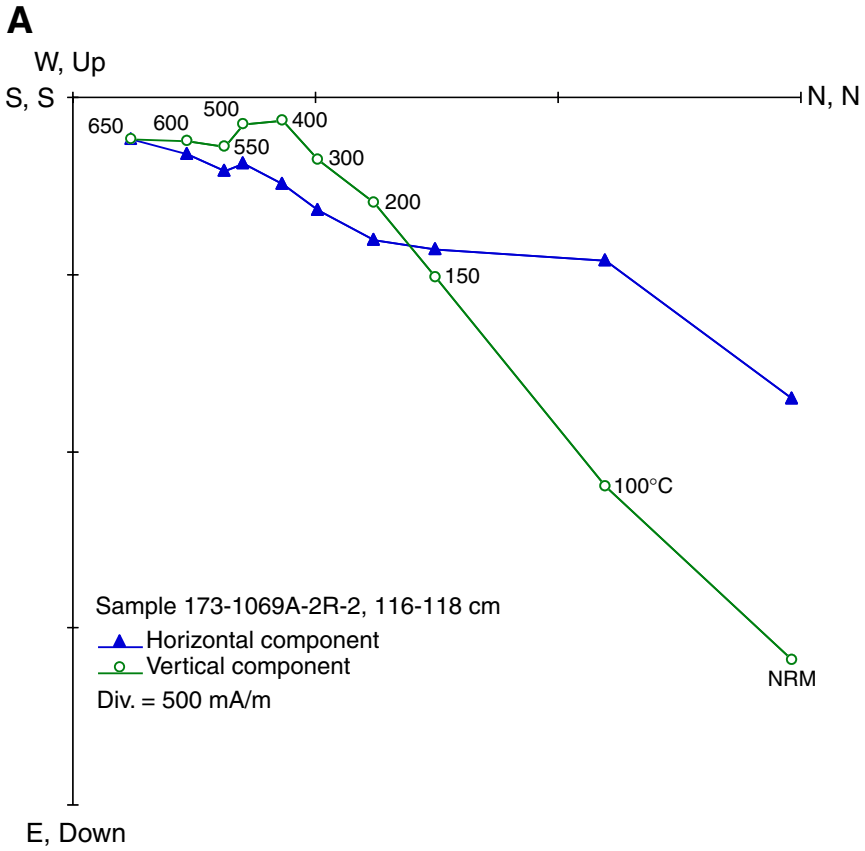

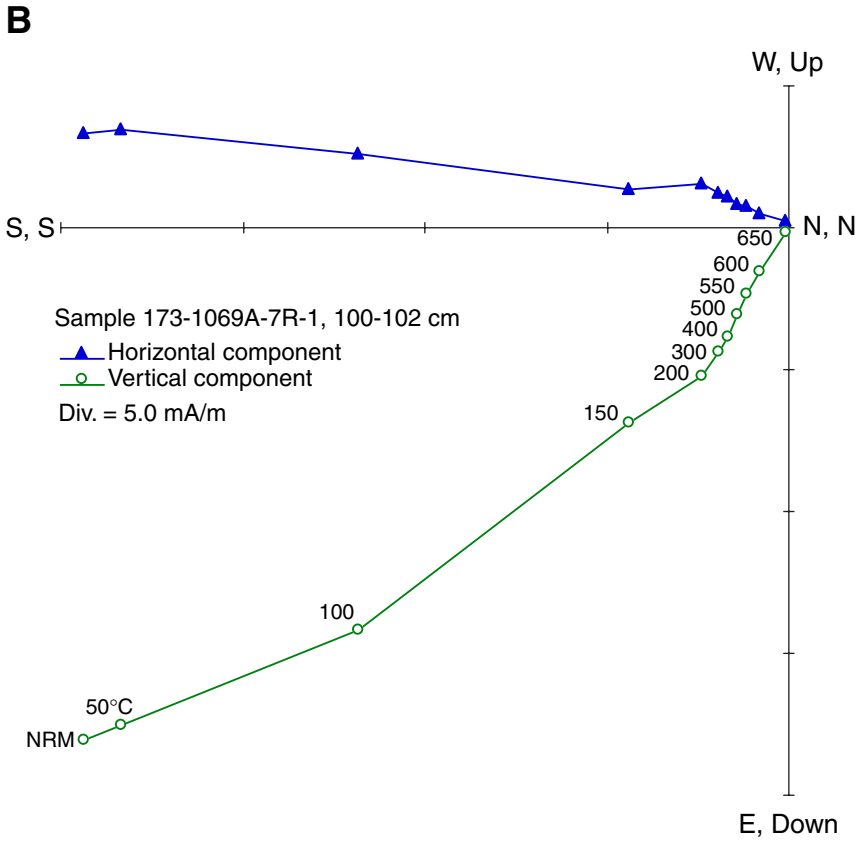

Figure F22 (continued). Samples (**C**) 173-1069A-7R-2, 29–31 cm, and (**D**) 173-1069A-7R-3, 60–62 cm, show reversed polarity of ChRM.

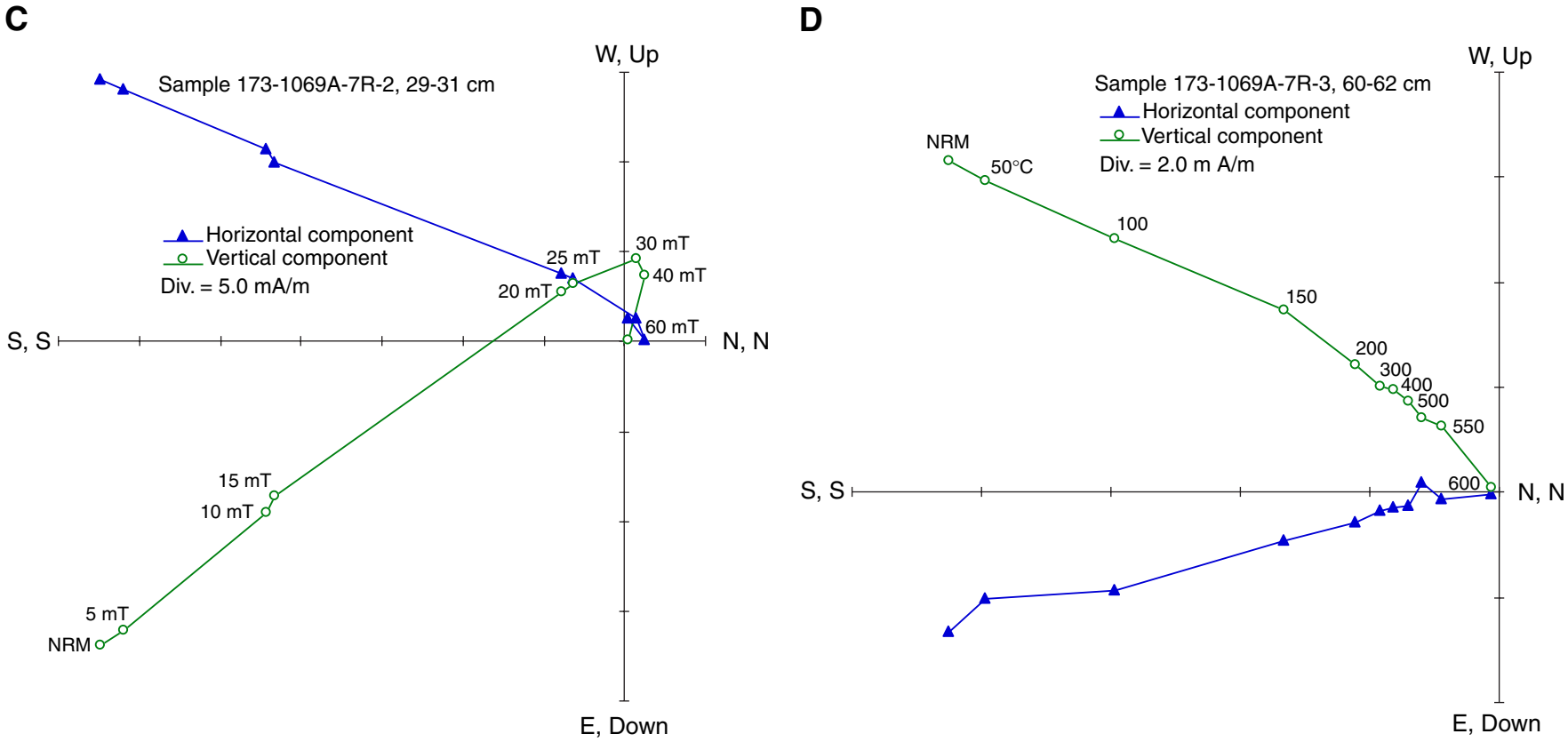

Figure F23. Downhole variation of stable magnetic inclination, inferred polarity, and biostratigraphic zones for Cenozoic sediments at Site 1069. Black bands = normal polarity, white bands = reversed polarity.

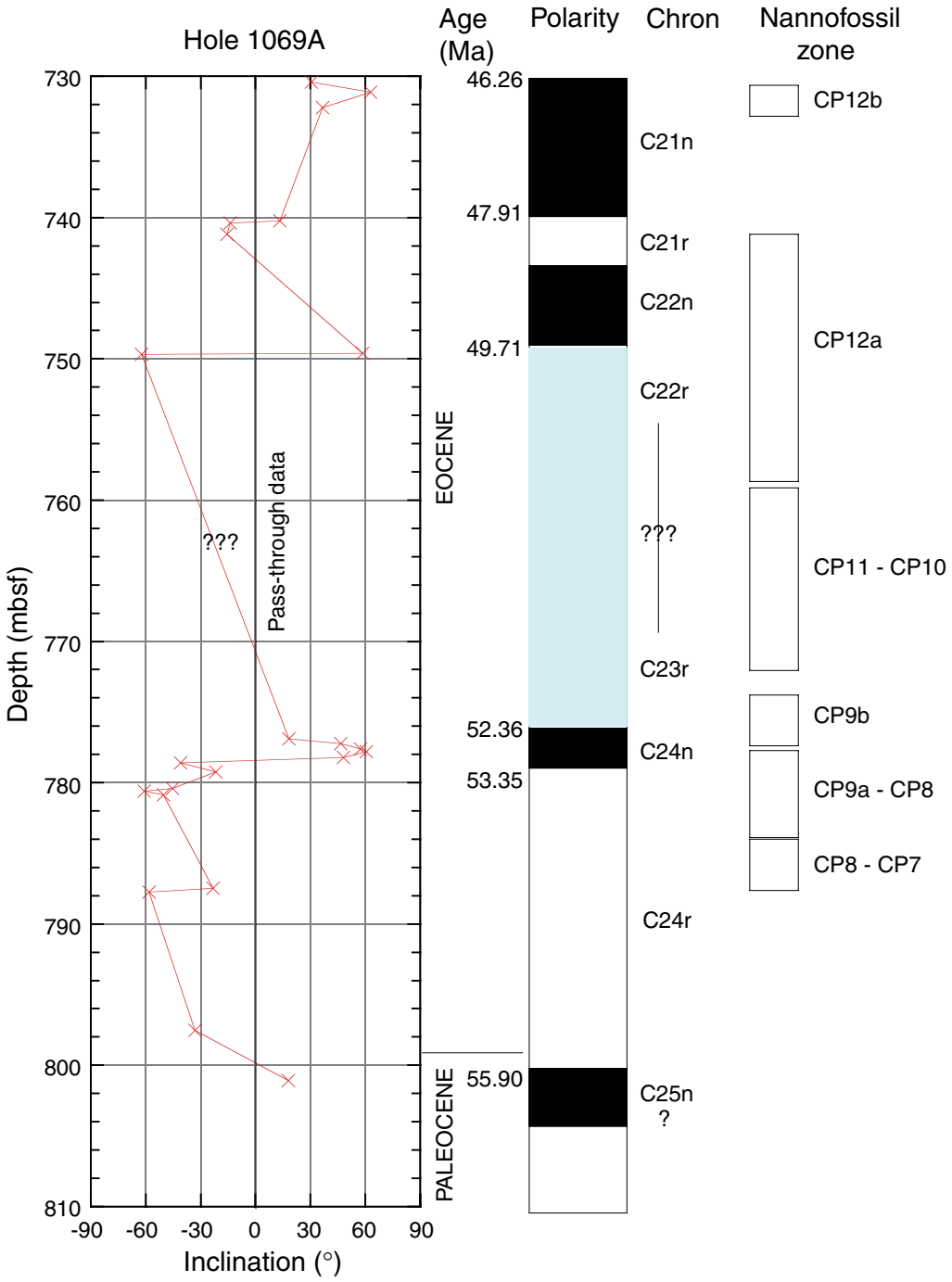

Figure F24. Depth vs. age curve for Hole 1069A. The paleomagnetic data points are listed in Table T13, p. 71. The short hiatus or a decrease in sedimentation rate is once again inferred around the Paleocene/Eocene boundary.

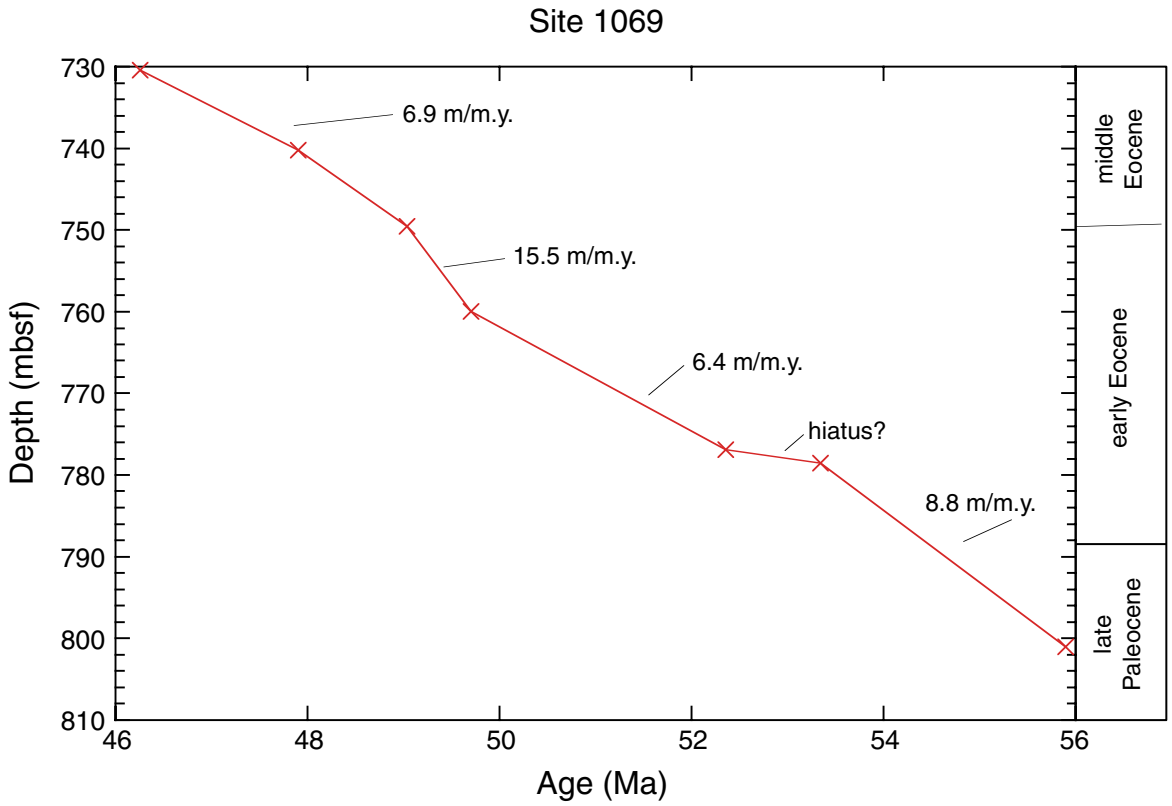

Table T1. Paleomagnetic results from Hole 897C used to determine magnetostratigraphy at Site 897.

Core, section, interval (cm)	Depth (mbsf)	NRM intensity (mA/m)	AF demagnetization step (mT)	Inclination (°)	Polarity
149-897C-					
1R-1, 102-104	50.92	0.87	50	55.1	N
1R-2, 61-64	52.01	0.05	20	41.3	N
2R-1, 88-90	60.78	0.295	70	33	N
2R-1, 121-123	61.11	0.88	80	39.2	N
2R-2, 7-9	61.47	7.41	50	61.6	N
3R-1, 83-85	70.43	2.91	70	57.7	N
4R-1, 34-36	79.54	0.812	60	50.7	N
5R-1, 27-30	89.17	1.98	85	33.5	N
5R-2, 27-69	91.07	4.13	60	41.8	N
6R-1, 27-30	98.77	1.19	60	34.2	N
6R-1, 58-61	99.08	1.05	60	46.9	N
6R-2, 96-98	101.88	21.67	50	49.1	N
7R-1, 54-57	108.7	1.36	50	28.7	N
7R-1, 62-65	108.8	0.29	50	42.2	N
8R-1, 103-105	118.9	6.77	99	–50.3	R
8R-1, 123-125	119.1	4.75	99	–46.7	R
8R-2, 81-83	120.2	0.09	80	–52.8	R
8R-2, 110-112	120.5	0.05	80	–55.2	R
8R-3, 20-22	121.1	0.08	80	–50.2	R
8R-3, 79-81	121.7	0.08	80	–52.6	R
9R-2, 19-21	128.7	0.07	20	38.6	N
9R-2, 53-55	129.1	0.03	70	36.8	N
10R-1, 20-22	137.4	1.93	80	–40.5	R
10R-1, 62-64	137.8	0.02	50	–56.7	R
10R-1, 121-123	138.4	0.03	40	–55	R
11R-2, 28-30	147.4	3.2	70	–53.3	R
11R-2, 31-33	147.4	0.89	60	–51.8	R
11R-3, 52-54	148.8	0.32	60	–62.1	R
11R-3, 125-127	149.6	0.65	60	–63.6	R
11R-4, 14-16	150	1.23	60	–64.1	R
11R-4, 66-68	150.5	0.08	60	–53.6	R
12R-6, 31-33	164.4	0.49	40	–55.8	R
12R-6, 37-39	164.5	0.13	99	–57.9	R
14R-1, 44-46	176.2	0.34	60	–49.8	R
14R-1, 69-71	176.5	0.52	70	–48.7	R
14R-2, 6-8	177.4	0.06	70	–72.8	R
14R-2, 15-17	177.5	0.19	80	–49.3	R
14R-2, 29-31	177.6	0.24	60	–47.4	R
14R-3, 6-8	178.9	0.11	60	–24.6	R
14R-3, 18-20	179	0.02	30	–9.4	R
14R-3, 123-125	180	0.03	30	–51.6	R
14R-4, 3-5	180.3	0.36	30	–21.4	R
14R-4, 70-72	181	0.38	30	–40.2	R
14R-4, 110-112	181.4	0.02	30	–52.9	R
15R-1, 26-29	185.7	3.76	60	–13.2	R
15R-1, 134-136	186.7	0.09	50	–53.5	R
15R-2, 11-13	187	0.08	40	–52.8	R
15R-2, 85-87	187.8	0.18	40	–59.1	R
15R-3, 71-74	189.1	2.57	60	–51.4	R
15R-3, 121-123	189.6	5.69	80	–39.5	R
15R-4, 24-27	190.1	2.67	50	–60	R
16R-1, 36-38	195.5	0.07	80	–73.5	R
16R-1, 57-59	195.7	0.09	80	–66	R
16R-2, 57-59	197.2	0.09	80	–38.3	R
16R-2, 93-95	197.5	0.09	80	–65.7	R
16R-3, 10-12	198.2	0.07	60	30.6	N
16R-3, 69-71	198.8	0.48	50	52.5	N
16R-4, 35-37	200	0.63	40	44.8	N
17R-1, 20-22	204.9	0.02	30	20.9	N
17R-1, 42-44	205.1	0.22	40	11.9	N
17R-1, 132-134	206	0.02	20	46.1	N
17R-2, 24-26	206.4	0.07	40	48.8	N
17R-2, 113-115	207.3	0.03	40	–12.5	R
18R-1, 33-35	214.7	0.54	60	–47.7	R
18R-1, 38-40	214.8	0.07	50	–35.8	R
19R-1, 36-38	224.5	25.1	80	–52.6	R
19R-2, 38-40	226	20.5	80	–59.5	R
19R-2, 74-76	226.34	8.9	60	–60	R
19R-2, 99-101	226.6	16.3	60	–53.7	R
19R-3, 73-75	227.8	9.57	80	–58.4	R
19R-3, 114-116	228.2	1.32	70	–57.5	R
19R-4, 52-54	229.1	0.17	60	–71.8	R
19R-4, 68-70	229.3	0.07	60	–59.4	R
20R-1, 34-36	234.1	0.04	30	–55.9	R
20R-1, 51-53	234.3	0.04	30	63.5	N
20R-1, 93-95	234.7	0.1	45	46.4	N
20R-2, 36-38	235.7	0.11	60	–45.5	R
20R-2, 45-47	235.8	0.04	40	–65	R
20R-2, 69-71	236	3.5	80	–56.1	R
20R-2, 90-92	236.2	2.96	60	–65.8	R
21R-1, 18-21	243.6	2.44	60	–57.8	R
21R-1, 69-71	244.1	3.88	60	–52.9	R
21R-1, 109-111	244.5	1.18	50	–49.8	R
22R-1, 87-89	253.9	0.65	70	–62.8	R
22R-1, 100-102	254	1.81	60	–54.8	R
22R-1, 120-122	254.2	0.19	60	–63.2	R
22R-2, 107-109	255.6	0.56	40	–56.2	R
22R-2, 140-142	255.9	5.15	50	–57.4	R
22R-5, 11-13	259.1	4.49	70	–63.9	R
22R-5, 26-28	259.3	6.08	70	–47.2	R
23R-1, 63-65	263.3	0.13	60	–55.1	R
23R-1, 132-134	264	0.15	60	–5.4	R
23R-2, 39-41	264.6	0.04	30	–41.4	R
23R-2, 41-43	264.6	0.05	50	–31.6	R
23R-3, 45-47	266.2	0.06	60	–53.2	R
23R-3, 47-49	266.2	0.08	40	–20.4	R
24R-1, 90-92	273.2	2.15	50	–65.6	R
24R-1, 124-126	273.5	2.64	50	–73.4	R
24R-2, 20-22	274	1.7	50	–72.8	R
24R-2, 20-24	274.02	2.7	50	–31.5	R
24R-2, 36-38	274.2	0.86	65	–67.6	R
25R-1, 21-23	282.2	6.88	50	–56.4	R
25R-2, 4-6	283.4	0.46	40	–63	R
25R-2, 49-51	283.8	0.21	40	–44.6	R
26R-1, 138-140	292.9	6.26	15	–14.4	R
26R-2, 91-93	293.9	3.89	15	–59.7	R
26R-2, 120-122	294.2	0.34	15	53.9	N
28R-1, 81-83	311.7	5.78	15	41.7	N
28R-1, 90-92	311.8	3.8	15	55.3	N
28R-2, 91-93	313.3	3.93	15	–30.1	R?
28R-2, 100-102	313.4	2.88	15	–31.2	R?
28R-2, 124-126	313.6	6.7	15	38.3	N
28R-3, 32-34	314.2	2.22	15	–42.8	R
28R-3, 42-44	314.3	3.66	15	–27.1	R
28R-4, 100-102	316.4	2.15	15	0.1	R?
29R-1, 27-29	320.79	4.92	15	26.7	N
29R-1, 81-83	321.31	7.27	15	–17.6	R
29R-2, 116-118	323.16	2.67	15	31.2	N
29R-3, 115-117	324.66	2.91	15	21.1	N
29R-4, 37-39	325.38	3.51	15	0.7	N?
29R-5, 75-77	327.26	1.63	15	22.9	N
29R-6, 43-45	328.44	1.12	15	12.2	N
30R-1, 56-58	330.76	3.65	15	4.1	N?
30R-2, 110-112	332.8	0.14	15	60.9	N
30R-3, 14-16	333.34	0.91	15	0.3	N?
30R-3, 75-77	333.95	0.5	25	10.6	N?

Notes: NRM = natural remanent magnetization, AF demagnetization step = highest peak field applied during progressive alternating-field demagnetization, inclination = stable inclination after demagnetization. N = normal polarity, R = reversed polarity.

Table T2. Paleomagnetic and biostratigraphic datums at Site 897.

Magnetic datum (chron or subchron)	Biostratigraphic datum (N, F)	Age (Ma)		Depth range (mbsf)		Sedimentation rate (m/m.y.)
		Magnetism	Biostratigraphy	Magnetism	Biostratigraphy	
Brunhes/Matuyama	NN19h, N23	0.78	0.48-0.83	108.2	50.35-109.26	138.71
Jaramillo	NN19f	0.99-1.07	0.89-1.06	128.72-137.4	127.5-137.20	108.5
Olduvai	NN19a, N22	1.77-1.95	1.66-1.91	198.20-207.33	181.18-207.17	50.72
Reunion(?)	NN18	2.14-2.15	1.95-2.36	234.14-235.66	207.87-263.83	152
Matuyama/Gauss	NN16	2.58		292.88	292.43	113.5

Note: N = nannofossil, F = foraminifer datum.

Table T3. Paleomagnetic results from Hole 898A used to determine the magnetostratigraphy at Site 898. (See table notes. Continued on next page.)

Core, section, interval (cm)	Depth (mbsf)	NRM intensity (mA/m)	AF demagnetization step (mT)	Inclination (°)	Polarity
149-898A-					
1H-6, 15-17	7.65	14.2	80	38	N
2H-4, 15-17	13.85	7.1	80	51.4	N
2H-4, 74-76	14.44	7.64	80	66.4	N
3H-3, 52-54	22.24	7.61	80	36.1	N
3H-4, 20-22	23.42	6.65	80	59.3	N
3H-6, 59-61	26.81	13.3	80	22.4	N
4H-1, 86-88	29.06	10.4	30	–53.2	R
4H-2, 108-110	30.78	24.3	80	–69.5	R
4H-4, 93-95	33.63	5.98	80	–55.9	R
4H-5, 121-123	35.41	24.3	80	–75.9	R
4H-6, 8-10	35.78	3.82	80	–73.6	R
4H-6, 89-91	36.59	12.3	80	–61.9	R
5H-1, 76-78	38.46	9.84	30	–30.8	R
5H-1, 143-145	39.13	14.4	70	–52.6	R
5H-2, 10-12	39.3	7.38	70	–45.7	R
5H-3, 129-131	41.99	4.16	99	–19.3	R
5H-3, 134-136	42.04	3.75	80	–40.3	R
5H-4, 59-61	42.82	2.11	60	–41	R
5H-5, 24-26	43.97	3.9	50	–16.5	R
5H-5, 57-59	44.3	3.77	80	–65.2	R
5H-6, 31-33	45.55	5.84	70	–61.9	R
5H-6, 56-58	45.8	4.36	60	–59.1	R
5H-7, 15-17	46.9	2.02	60	–60.3	R
6H-2, 10-12	48.81	5.3	60	–54.6	R
6H-2, 124-126	49.95	2.66	60	–58.2	R
6H-3, 69-71	50.9	0.49	60	–44.7	R
6H-4, 63-65	52.34	0.13	40	–3.4	R?
6H-4, 117-119	52.88	0.37	50	–47	R
6H-5, 27-29	53.49	1.02	50	–33.3	R
6H-6, 136-139	56.08	0.06	30	–36.5	R
6H-7, 17-19	56.39	0.4	40	–46.2	R
6H-7, 29-32	56.51	0.09	40	–30.6	R
7H-3, 62-64	60.32	0.11	80	–31.8	R
7H-7, 1-3	65.71	2.35	30	–10.2	R?
8H-3, 32-34	69.55	2.28	70	–43.3	R
8H-7, 16-18	75.42	22.1	90	–52.9	R
8H-7, 23-25	75.49	10	70	–48.4	R
9H-1, 40-42	76.1	0.19	65	–52.8	R
10H-3, 93-95	89.13	0.09	60	–63.5	R
10H-5, 31-33	91.51	0.23	60	–63.1	R
11H-1, 45-47	95.15	2.5	70	–56.6	R
11H-2, 43-45	96.65	5.58	50	–51.4	R
11H-3, 28-30	98	3.86	30	–20.2	R
11H-4, 43-45	99.65	5.02	80	–59.6	R
11H-5, 102-104	101.74	7.3	30	17.3	N
12H-1, 108-110	105.28	3.05	60	58.6	N
12H-1, 144-146	105.64	9.35	65	–12.9	N?
12H-2, 0	105.7	17.24	20	48.8	N
12H-2, 2	105.72	21.33	20	40.1	N
12H-2, 4	105.74	8.82	35	47.7	N
12H-2, 6	105.76	1	35	58.5	N
12H-2, 8	105.78	0.83	20	32.7	N
12H-2, 10	105.8	1.14	20	36.6	N
12H-2, 12	105.82	3	20	19.1	N
12H-2, 14	105.84	1.23	35	33.6	N
12H-2, 16	105.86	3.97	25	36	N
12H-2, 18	105.88	4.51	40	–8.3	N?
12H-2, 20	105.9	1.92	20	37.7	N
12H-2, 22	105.92	0.98	20	49.8	N
12H-2, 24	105.94	4.41	20	39.7	N
12H-2, 26	105.96	3.23	30	49.7	N
12H-2, 28	105.98	3.26	20	39.8	N
12H-2, 30	106	3.37	20	24.2	N
12H-2, 32	106.02	4.71	40	53.7	N
12H-2, 34	106.04	4.93	20	22.9	N
12H-2, 36	106.06	5.83	35	36.5	N
12H-2, 38	106.08	1.01	50	33.1	N
12H-2, 40	106.1	0.86	30	32.5	N
12H-2, 42	106.12	1.6	30	37.1	N
12H-2, 44	106.14	3.11	30	36.3	N
12H-2, 46	106.16	1.84	35	50.4	N
12H-2, 48	106.18	1.91	35	40	N
12H-2, 50	106.2	6.01	50	64.5	N
12H-2, 52	106.22	6.13	20	38.8	N
12H-2, 54	106.24	9.32	30	12.3	N
12H-2, 56	106.26	1.46	20	34.7	N
12H-2, 58	106.28	0.5	25	19.3	N
12H-2, 60	106.3	3.68	30	28.7	N
12H-2, 62	106.32	1.95	30	30.5	N
12H-2, 64	106.34	1.25	30	35.5	N
12H-2, 66	106.36	3.3	20	49.52	N
12H-2, 68	106.38	4.93	20	38.6	N
12H-2, 70	106.4	1.82	25	8.1	N
12H-2, 72	106.42	0.82	25	24.4	N
12H-2, 74	106.44	0.83	25	15	N
12H-2, 76	106.46	0.78	30	–23.5	R
12H-2, 78	106.48	2.09	30	–12.1	R
12H-2, 80	106.5	5.91	25	–20.2	R
12H-2, 82	106.52	3.35	25	–13.5	R
12H-2, 84	106.54	2.74	30	6	R?
12H-2, 86	106.56	1.09	30	4.1	R?
12H-2, 88	106.58	2.42	30	14.2	R?
12H-2, 90	106.6	9.13	35	–17.6	R
12H-2, 92	106.62	7.58	30	5.9	R?
12H-2, 94	106.64	1.39	30	–2.5	R?
12H-2, 96	106.66	2.08	30	–4.6	R
12H-2, 98	106.68	1.51	30	8.6	R?
12H-2, 100	106.7	5.06	35	–54.1	R
12H-2, 102	106.72	5.04	20	7.8	N?
12H-2, 104	106.74	8.03	20	11.3	N?
12H-2, 106	106.76	5.1	30	–28.1	R
12H-2, 108	106.78	8.76	30	–43	R
12H-2, 110	106.8	4.09	30	11.6	N?
12H-2, 112	106.82	6.78	30	–4.9	R?
12H-2, 114	106.84	1.07	25	3.6	N?
12H-2, 116	106.88	1.14	25	–6.2	R?
12H-2, 118	106.9	12.92	30	–12.1	R?
12H-2, 120	106.92	13	30	–29.6	R
12H-2, 122	106.94	5.45	30	–2.5	R?
12H-2, 124	106.96	2.59	20	–21	R
12H-2, 126	106.98	14.23	20	–58.2	R
12H-2, 128	107	2.79	20	–35.4	R
12H-2, 130	107.02	5.54	20	–11.1	R
12H-2, 132	107.04	4	30	–49.1	R
12H-2, 134	107.06	3.96	20	–41.6	R
12H-2, 136	107.08	9.69	25	–49.8	R
12H-2, 138	107.1	23.16	30	–50.7	R
12H-2, 140	107.12	4.53	25	–55.3	R
12H-2, 142	107.14	3.36	25	–46.4	R
12H-2, 144	107.16	2.96	25	–70.9	R
12H-2, 146	107.18	5.39	25	–60.2	R
12H-2, 148	107.2	5.81	25	–61.9	R
12H-3, 15-17	107.37	6.39	80	–58.8	R
12H-3, 28-30	107.5	5.93	70	43	N
12H-4, 73-75	109.45	0.29	40	–49.6	R
12H-4, 81-83	109.53	0.39	80	–60.2	R
12H-6, 66-68	112.4	2.89	40	–20.9	R
12H-6, 91-93	112.65	0.11	60	–48.4	R
13H-1, 32-34	114.02	15.8	30	–19.4	R
13H-1, 121-123	114.91	0.4	80	–42.5	R
13H-2, 74-76	115.94	12.1	90	–45.2	R
13H-2, 105-107	116.25	1.23	80	–44	R
13H-3, 94-96	117.64	12.1	30	–18.1	R

Table T3 (continued).

Core, section, interval (cm)	Depth (mbsf)	NRM intensity (mA/m)	AF demagnetization step (mT)	Inclination (°)	Polarity
13H-4, 65-67	118.85	0.08	80	–13	R
13H-5, 23-25	119.93	0.53	60	–58	R
13H-5, 82-84	120.52	0.39	90	–43.2	R
13H-6, 134-136	122.54	0.67	60	–40.7	R
13H-6, 136-138	122.56	0.27	80	–27	R
14H-1, 73-75	123.93	0.43	60	–39	R
14H-2, 139-141	126.1	0.06	40	–31.8	R
14H-3, 12-14	126.35	0.43	60	–52.1	R
14H-4, 84-86	128.6	0.75	40	–49	R
14H-4, 122-124	129.98	0.06	50	–56.6	R
14H-6, 42-44	131.23	0.08	30	–42.3	R
14H-7, 10-12	131.23	0.2	60	–20.4	R
15X-1, 88-90	133.58	0.13	60	–45.7	R
15X-1, 125-127	133.95	0.41	60	–51.2	R
15X-2, 84-86	135.04	0.3	50	–47.8	R
15X-2, 126-128	135.46	0.15	60	–44.3	R
15X-3, 15-17	135.85	0.1	70	–46.1	R
15X-3, 21-23	135.91	0.21	80	–65.6	R
15X-4, 33-35	137.53	0.23	55	2	R?
15X-4, 53-55	137.73	0.04	45	–34.5	R
15X-5, 7-9	138.77	0.12	65	–30.5	R
16X-1, 98-100	139.78	0.21	20	–53.3	R
16X-1, 113-115	139.93	0.21	50	–41.7	R
16X-2, 21-23	140.51	0.35	25	–59.9	R
16X-3, 18-20	141.98	0.07	60	–55.1	R
16X-3, 135-137	143.15	0.28	40	–54.2	R
16X-4, 55-57	143.85	0.09	30	39.8	N
16X-4, 132-134	144.62	0.05	30	–60.9	R
16X-5, 75-77	145.55	6.27	20	–22.6	R
16X-5, 90-92	145.7	0.2	60	–59.5	R
17X-1, 47-49	148.97	0.2	45	14.4	N?
17X-2, 32-34	150.32	0.18	45	–15.7	R
17X-3, 25-27	151.75	0.03	30	–34.9	R
17X-4, 29-31	153.29	0.16	80	–12.9	R?
17X-5, 80-82	155.3	0.3	40	–57.2	R
17X-6, 72-75	156.72	2.52	20	–69.1	R
18X-1, 129-131	159.39	0.28	40	–56.8	R
18X-2, 35-38	159.97	1.67	60	–10.9	R?
18X-2, 95-97	160.57	3.69	40	–44	R
18X-3, 70-72	161.82	4.53	40	17.5	N
18X-4, 25-29	162.87	2.05	60	–5.4	N?
18X-4, 114-116	163.76	0.18	40	6.4	N?
18X-5, 124-126	165.36	14.7	80	–74.2	R
18X-6, 34-36	165.96	16.6	20	–45.2	R
18X-6, 132-134	166.94	12.6	60	29.3	N
18X-7, 8-10	167.2	22.4	60	–53.5	R
19X-1, 23-25	168.03	8.57	60	–33.5	R
19X-1, 115-117	168.95	26.7	60	–66.3	R
19X-2, 58-60	169.88	18.5	60	–61.6	R
19X-2, 93-95	170.23	8.61	30	–40.8	R
19X-3, 33-35	171.13	30.2	60	–75.8	R
19X-4, 92-94	173.22	13.4	60	–56.8	R
19X-5, 34-36	174.14	8.62	40	–45.8	R
19X-5, 69-71	174.49	3.52	40	–75.4	R
19X-6, 58-61	175.88	2.53	40	–69.1	R
20X-1, 51-53	177.91	0.05	30	–46.7	R
20X-2, 94-96	179.84	2.35	20	–28.8	R
20X-2, 130-132	180.2	0.06	30	–55.1	R
20X-3, 104-106	181.44	0.08	30	–46.8	R
20X-3, 112-114	181.52	0.04	30	–37.6	R
20X-4, 52-54	182.42	0.03	30	–39.3	R
20X-4, 84-86	182.74	0.03	20	48.4	N
21X-1, 54-56	187.54	5.16	20	–15.8	N?
21X-1, 131-133	188.31	0.06	20	–20.3	R?
21X-2, 65-67	189.15	3.41	50	–35.2	R
21X-2, 93-95	189.43	1.96	20	1.8	R?
21X-3, 75-78	190.75	0.06	20	–31.6	R
21X-3, 133-135	191.33	0.05	30	1.9	R?
21X-4, 53-55	192.03	0.08	25	–11.6	R?
21X-4, 75-77	192.25	0.06	20	–15.6	R?
22X-1, 33-35	197.03	0.07	30	64.9	N
22X-2, 45-47	198.65	1.18	20	25.8	N
22X-3, 90-92	200.6	1.98	20	51.6	N
22X-4, 21-23	201.41	1.59	20	–0.2	N?
22X-4, 131-133	202.51	0.09	40	63.6	N
22X-5, 31-33	203.01	0.05	40	51.4	N
22X-6, 54-56	204.74	0.06	40	36.8	N
22X-6, 98-100	205.18	0.05	40	31	N
22X-7, 12-14	205.82	0.03	60	60.4	N
23X-1, 46-48	206.86	0.09	40	–39	R
23X-2, 40-42	208.3	0.09	20	–63.8	R
23X-2, 79-82	208.69	0.41	30	–60	R
23X-3, 31-33	209.73	0.1	40	–53.2	R
23X-3, 96-99	210.38	0.07	40	–53.6	R

Notes: NRM = natural remanent magnetization, AF demagnetization step = highest peak field applied during progressive alternating-field demagnetization, inclination = stable inclination after demagnetization. N = normal polarity, R = reversed polarity.

Table T4. Paleomagnetic and biostratigraphic datums at Site 898.

Magnetic datum (chron or subchron)	Biostratigraphic datums (N, F)	Age (Ma)		Depth range (mbsf)		Sedimentation rate (m/m.y.)
		Magnetism	Biostratigraphy	Magnetism	Biostratigraphy	
Brunhes/Matuyama	NN19h, N23/N22	0.78	0.48-0.83	29.06	20.34-47.20	37.26
Jaramillo	NN19f	0.99-1.07	0.89-1.06	101.74-106.88	54.69-59.77	64.25
Olduvai	NN19a	1.77-1.95	1.66-1.91	143.85-161.82	144.33-163.18	99.8
C5D?	N7/N6	17.31-17.65	E. Miocene	197.03-205.82	196.7-206.4	25.88

Note: N = nannofossil, F= foraminifer datum.

Table T5. Paleomagnetic results from Hole 900A used to determine the magnetostratigraphy at Site 900. (See table notes. Continued on next page.)

Core, section, interval (cm)	Depth (mbsf)	NRM intensity (mA/m)	AF demagnetization step (mT)	Inclination (°)	Polarity
149-900A					
4R-1, 7-9	20.87	2.7	80	20.6	N
4R-1, 28-30	21.08	14	90	40.5	N
5R-1, 27-29	30.67	5	70	–35.2	R
5R-1, 34-36	30.74	16	70	–62.1	R
5R-1, 96-98	31.36	4	60	–6	R
5R-2, 27-29	32.17	10	60	–53.3	R
5R-2, 30-32	32.2	16	70	–52.3	R
6R-4, 38-40	44.88	3.8	99	–48.4	R
6R-4, 95-97	45.45	10	60	–69.1	R
6R-5, 45-47	46.45	46	80	–63.7	R
6R-5, 95-97	46.95	3.1	65	–48.3	R
6R-5, 100-102	47	6.7	50	32.7	N
6R-6, 50-52	48	5.8	25	36	N
6R-6, 56-58	48.06	18.7	80	34.3	N
6R-6, 104-106	48.54	3.7	99	–53.1	R
7R-1, 51-53	50.11	7.2	70	–37.3	R
7R-1, 116-118	50.76	7.9	70	–42.3	R
7R-2, 28-30	51.38	10.9	70	–43	R
7R-2, 31-33	51.41	9.3	70	–51.7	R
7R-3, 4-7	52.64	12.7	80	–31.9	R
7R-6, 33-35	57.43	9	80	–39.7	R
8R-1, 9-11	59.39	18.1	70	–43.7	R
8R-1, 17-19	59.47	19	70	–56.1	R
8R-3, 72-74	63.02	5.9	60	–30.5	R
8R-3, 80-82	63.1	18	70	–26.5	R
8R-3, 83-85	63.13	13.5	70	–55.2	R
9R-1, 5-7	64.55	11.2	45	29	N
9R-1, 67-69	65.17	10.4	70	28.8	N
9R-1, 76-78	65.26	10.6	70	18.2	N
9R-2, 40-42	66.4	4.46	80	34.4	N
9R-2, 114-116	67.14	9.49	50	65.4	N
9R-3, 10-12	67.6	22	70	30.6	N
9R-3, 33-35	67.83	12	70	52.1	N
10R-1, 61-63	74.71	8.27	60	52.3	N
10R-1, 94-96	75.04	14.2	70	39	N
10R-2, 35-37	75.95	10.6	80	54.1	N
10R-2, 70-72	76.3	12	70	51.2	N
10R-2, 130-132	76.9	3.24	70	–53.8	R
10R-3, 1	77.1	7.82	35	–45.6	R
10R-3, 3	77.12	6.75	20	–49.5	R
10R-3, 5	77.14	11	20	–50	R
10R-3, 7	77.16	2.95	25	–21.8	R
10R-3, 11	77.18	5.29	25	–14.2	R
10R-3, 13	77.2	5.41	30	–24.1	R
10R-3, 15	77.22	3.18	20	–15.3	R
10R-3, 18	77.24	5.12	30	–5.8	R
10R-3, 20	77.26	4.65	20	–14.6	R
10R-3, 22	77.28	5.71	20	–16.9	R
10R-3, 25	77.3	7.73	35	–16	R
10R-3, 28	77.32	10.47	30	52	N
10R-3, 31	77.34	8.78	35	–17.8	R
10R-3, 34	77.36	7.71	20	–11	R
10R-3, 36	77.38	5.64	25	–14.8	R
10R-3, 38	77.4	5.6	35	–15.8	R
10R-3, 41	77.42	10.15	20	–7.4	R
10R-3, 43	77.44	8.63	20	–23.5	R
10R-3, 45	77.46	2.17	25	–38.6	R
10R-3, 49	77.48	5.46	25	–15.3	R
10R-3, 51	77.5	7.1	20	–15.3	R
10R-3, 53	77.52	7.9	20	–15.7	R
10R-3, 57	77.54	6.15	20	–8.4	R
10R-3, 60	77.56	8.26	20	–7.2	R
10R-3, 62	77.58	4.94	25	–31.3	R
10R-3, 64	77.6	4.56	35	–36.3	R
10R-3, 66	77.62	8.75	20	–24.9	R
10R-3, 68	77.64	4.71	20	–57.5	R
10R-3, 70	77.66	6.76	20	–14.1	R
10R-3, 72	77.68	17.52	35	–43.2	R
10R-3, 75	77.7	6.37	20	–19.9	R
10R-3, 78	77.72	4.58	20	55.3	N
10R-3, 82	77.74	4.94	20	11.2	N
10R-3, 84	77.76	6.09	30	59.4	N
10R-3, 86	77.78	6.11	20	–13.8	R
10R-3, 89	77.8	5.35	30	–19.5	R
10R-3, 92	77.82	4.28	25	–78.4	R
10R-3, 94	77.84	6.62	25	–39.4	R
10R-3, 96	77.86	5.67	25	–35.9	R
10R-3, 98	77.88	5.72	25	–43.1	R
10R-3, 100	77.9	5.97	25	–39	R
10R-3, 102	77.92	3.55	25	–42.2	R
10R-3, 104	77.94	7.28	20	–26.9	R
10R-3, 106	77.96	5.02	20	–12.5	R
10R-3, 108	77.98	7.53	20	–8.3	R
10R-3, 110	78	7.67	20	0.9	R?
10R-3, 112	78.02	6.7	20	–15.4	R
10R-3, 114	78.04	2.99	30	–35.4	R
10R-3, 116	78.06	3.52	25	–41.2	R
10R-3, 118	78.1	3.24	25	–79.1	R
10R-3, 120	78.12	2.46	25	–69.4	R
10R-3, 122	78.14	4.13	25	–30.8	R
10R-3, 124	78.16	4.86	25	–27.6	R
10R-3, 126	78.18	4.39	20	20.3	N
10R-3, 128	78.2	3.26	20	20.9	N
10R-3, 130	78.22	6.42	35	33.4	N
10R-3, 132	78.24	5.24	20	–38.7	R
10R-3, 134	78.26	6.84	20	–57.6	R
10R-3, 136	78.28	6.93	20	–48.7	R
10R-3, 138	78.3	3.13	20	–33.9	R
10R-3, 140	78.32	1.22	25	–24.2	R
10R-3, 142	78.34	2.4	34	–2.4	R
10R-3, 144	78.36	3.54	34	4.4	N
10R-3, 146	78.38	2.61	25	19.5	N
10R-3, 148	78.38	4.7	25	24	N
10R-4, 7-9	78.67	3.82	70	66.9	N
10R-4, 59-61	79.19	4.82	70	–49.6	R
10R-4, 139-141	79.99	3	70	–76.1	R
10R-5, 4-6	80.14	13	70	–28.1	R
11R-1, 14-16	83.84	16.2	80	–48.1	R
11R-1, 52-54	84.22	4.48	80	18.6	N
11R-1, 65-67	84.35	7.99	80	–31.5	R
11R-2, 79-81	85.99	11.1	80	–68.1	R
11R-2, 98-100	86.18	10.4	80	–60.3	R
11R-3, 40-42	87.1	11	80	60.6	N
11R-3, 75-77	87.45	6.93	95	32	N
11R-4, 10-12	88.3	5.9	80	–51.6	R
11R-4, 110-112	89.3	13.2	80	38.6	N
11R-5, 2-4	89.72	7	80	35	N
11R-5, 29-31	89.99	30.8	80	66.7	N
12R-1, 71-73	94.11	12.8	99	–49.6	R
12R-1, 127-129	94.67	9.94	50	–56.8	R
12R-2, 32-34	95.22	8.86	75	51.4	N
12R-2, 70-72	95.6	7.04	80	38.7	N
12R-3, 69-71	97.09	11.1	70	–65.9	R
12R-3, 84-86	97.24	12.6	70	–43.4	R
14R-1, 15-17	112.85	19	80	–35.7	R
14R-1, 110-112	113.8	28.4	80	15	N
14R-1, 133-135	114.03	18.7	80	46.8	N
14R-2, 39-41	114.59	4.41	70	15.6	N
14R-2, 87-89	115.07	5.49	80	–56.1	R
14R-2, 126-128	115.46	13.6	80	42.6	N
14R-3, 13-15	115.83	14.4	80	66.9	N
14R-3, 89-91	116.59	16.3	99	–43.2	R
14R-3, 126-128	116.96	6.91	80	–51.8	R

Table T5 (continued).

Core, section, interval (cm)	Depth (mbsf)	NRM intensity (mA/m)	AF demagnetization step (mT)	Inclination (°)	Polarity
14R-4, 24-26	117.44	5.09	80	–65	R
14R-4, 67-69	117.87	10.3	70	–61.1	R
14R-4, 91-93	118.11	8.31	80	–48.7	R
14R-5, 32-34	119.02	19.6	90	–55.1	R
14R-5, 107-109	119.77	19.4	80	–48.6	R
14R-5, 119-121	119.89	13.1	80	–59.2	R
14R-6, 14-16	120.34	8.87	70	–20.2	R
14R-6, 92-94	121.12	5.77	70	–24.7	R
14R-6, 140-142	121.6	1.7	80	–12.7	R
14R-7, 19-21	121.89	1.12	80	55.9	N
15R-1, 113-115	123.53	15.2	80	27.2	N
15R-1, 128-130	123.68	6.72	80	53.1	N
15R-2, 26-28	124.16	8.98	80	25.8	N
15R-2, 87-89	124.77	4.62	70	–66	R
15R-2, 128-130	125.18	8.31	99	–42.7	R
15R-3, 56-58	125.96	7.06	90	–53.5	R
15R-3, 65-67	126.05	8.08	90	–61.3	R
15R-3, 137-139	126.77	3.12	80	74.5	N
15R-4, 25-27	127.15	8.8	60	–62.6	R
16R-1, 33-35	132.33	0.05	20	42.4	N
16R-1, 72-74	132.72	5.97	70	–14.2	R
16R-2, 79-81	134.29	0.05	30	55.7	N
16R-2, 115-117	134.65	4.26	80	50.5	N
16R-3, 38-40	135.38	0.06	40	43.3	N
16R-3, 120-122	136.2	0.19	60	–15.7	R
16R-4, 14-16	136.64	0.87	95	–18.9	R
16R-4, 76-78	137.26	3.83	60	–45.7	R
16R-5, 27-29	138.27	11.7	60	38.6	N
16R-5, 39-41	138.39	2.02	80	46.3	N
16R-6, 42-44	139.92	7.53	80	34.2	N
16R-6, 101-103	140.51	0.19	55	41.7	N
17R-1, 25-27	141.85	2.41	80	–42.3	R
17R-1, 107-109	142.67	2.39	40	–53.4	R
17R-2, 24-26	143.34	0.06	15	–21.9	R
17R-2, 37-39	143.47	4.52	70	–40	R
17R-3, 20-22	144.8	4.43	90	–64.2	R
17R-3, 36-38	144.96	0.09	15	80	N?

Notes: NRM = natural remanent magnetization, AF demagnetization step = highest peak field applied during progressive alternating-field demagnetization, inclination = stable inclination after demagnetization. N = normal polarity, R = reversed polarity.

Table T6. Paleomagnetic and biostratigraphic datums in Hole 900A.

Magnetic datum (chron or subchron)	Biostratigraphic datum (N, F)	Age (Ma)		Depth range (mbsf)		Sedimentation rate (m/m.y.)
		Magnetism	Biostratigraphy	Magnetism	Biostratigraphy	
Jaramillo	NN19f	0.99-1.07	0.89-1.06	21.08	21.76-26.62	263.5
Olduvai	NN19a, N23/N22	1.77-1.95	1.66-1.91	47.00-48.06	43.86-47.96	5.9
Matuyama/Gauss	NN16	2.58		64.55	64.95-79.29	25.02
Mammoth		3.22-3.33		76.9-78.7		16.36
Gauss/Gilbert	NN15, N19	3.58		79.19	84.42-89.39	22.1
Cochiti		4.18-4.29		84.2-84.4		1.8
Nunivak		4.48-4.62		87.1-87.5		2.8
Sidutjall		4.8-4.89		89.3-90.0		7.8
Thvera		4.98-5.23		95.2-95.6		1.6
C3An,1n		5.83-6.05		113.8-114.6		3.6
C3An, 2n		6.17-6.45		115.4-115.8		1.5
C3Bn		6.79-6.94		121.9-124.2		15.3
C3Br, 1n		6.98-7.02		126.8-127.2		10
C3Br, 2n		7.18-7.22		132.3-132.7		10
C4n, 1n		7.27-7.4		134.3-136.2		14.61
C4n, 2n		7.48-7.9		138.3-140.5		5.24
C4r, 1n		8.06-8.09		144.9-?		17.98?

Note: N = nannofossil, F= foraminifer datum.

Table T7. Observations for the Eocene marker bed in the Ocean–Continent Transition Zone, Iberia.

Marker	Leg 173			Leg 149
	Site 1067	Site 1068	Site 1069	Site 900
Core, section:	12R-1	8R-1	7R-1	77R-1
Onset depth (mbsf):	744.5	778.9	776.9	720.0
Color:	Reddish brown (5Y 4/4)	Reddish brown (5Y 4/4)	Reddish brown (5Y 4/4)	Reddish brown (5Y 4/4)
Age:	early Eocene (NP11)	early Eocene (NP11)	early Eocene (NP11)	early Eocene (NP11)
NRM peak (A/m):	10^{-2}	10^{-2}	10^{-2}	10^{-2}
Downhole susceptibility peak (10^{-5} SI):	>100	>123	>148	>100
Polarity:	N-R	N-R	R	R

Note: N = normal, R = reversed polarity.

Table T8. Paleomagnetic results from Hole 1067A used to determine the magnetostratigraphy at Site 1067.

Core, section, interval (cm)	Depth (mbsf)	NRM (A/m)	NRM Inc (°)	ChRM Inc (°)	χ (10^{-5} SI)	Q-ratio	MDF/T_b (mT/°C)	Polarity
173-1067A-								
1R-2, 89-91	650.39	1.67E–4	62.6	68.5	12.9	0.04	(270)	N
2R-3, 50-52	661.10	1.03E–4	43.1	–48.7	18.8	0.12	(400)	R
3R-3, 100-102	671.30	1.93E–4	89.7	79.1	27.4	0.03	(400)	N
4R-2, 61-63	679.01	9.89E–5	58.8	42.2	16.8	0.02	30	N
4R-2, 73-75	679.13	1.16E–4	81.0	35.8	21.9	0.01	(400)	N
5R-1, 53-55	687.03	9.03E–5	66.5	63.4	11.8	0.02	20	N
5R-2, 86-88	688.86	7.49E–3	34.5	16.7	41.3	0.64	(250)	N
5R-3, 49-51	690.11	1.37E–3	81.0	–17.7	14.0	0.27	15	R
6R-1, 57-59	696.67	7.43E–4	46.2	27.5	14.6	0.14	45	N
6R-2, 14-16	697.74	1.77E–4	59.2	31.5	6.6	0.07	45	N
8R-1, 136-138	716.86	1.11E–4	64.3	24.2	2.4	0.13	15	N
8R-3, 115-117	719.65	9.65E–5	39.4	27.1	14.2	0.02	20	N
9R-1, 68-70	725.88	2.72E–3	67.2	63.9	19.6	0.39	35	N
10R-1, 113-115	735.93	5.76E–3	–35.7	–49.5	23.8	0.68	25	R
10R-1, 122-124	736.02	1.39E–2	62.0	28.9	24.2	1.60	10	N
10R-2, 58-60	736.88	2.07E–3	20.4	–6.2	22.8	0.25	40	R?
10R-3, 38-40	738.18	1.56E–3	–2.3	–3.1	18.0	0.24	100	R?
10R-4, 36-38	739.16	1.93E–3	47.2	38.0	21.2	0.25	60	N
11R-1, 39-41	739.99	8.60E–4	–31.7	0.2	21.6	0.11	80	N?
11R-1, 89-91	740.49	5.94E–3	45.1	5.3	27.8	0.60	30	N?
11R-2, 25-27	741.35	1.25E–2	–35.0	–33.5	32.6	1.07	40	R
11R-3, 26-28	742.86	3.23E–3	–2.4	–1.9	19.6	0.46	100	R?
11R-3, 61-63	743.21	1.46E–3	69.4	48.1	20.6	0.20	20	N
12R-1, 8-10	744.58	2.85E–2	9.1	–25.2	39.6	2.01	40	R
12R-1, 33-35	744.83	3.85E–2	63.9	56.3	87.8	1.22	15	N
12R-2, 25-27	745.75	2.10E–2	69.9	26.5	39.2	1.50	25	N
12R-2, 43-45	745.93	4.52E–2	–3.7	–4.0	55.4	2.28	40	R?

Notes: NRM = natural remanent magnetization intensity, NRM Inc = NRM inclination, ChRM Inc = characteristic or stable remanent magnetization inclination after demagnetization, χ = low-field magnetic susceptibility, Q-ratio = Koenigsberger ratio, MDF/T_b = median demagnetizing field/unblocking temperature. N = normal polarity, R = reversed polarity.

Table T9. Paleomagnetic and biostratigraphic datums in Hole 1067A.

Magnetic datum (chron or subchron)	Biostratigraphic datums (N, F)	Age (Ma)		Depth range (mbsf)		Sedimentation rate (m/m.y.)
		Magnetism	Biostratigraphy	Magnetism	Biostratigraphy	
C20n	CP14a, P11	42.54-43.79	40.5-43.7	650.39-661.10	648.37-653.53	8.57
C20r	CP13c, P11	43.79-46.27	43.7-44.5	661.10-671.30	658.81-661.39	4.11
C21n	CP13a-12b, P10	46.26-47.91	46.2-47.3	671.3-725.88	689.76-720.30	33.08
C22n	CP12a, P9	49.04-49.71	48.5-49.7	725.88-735.93	720.73-728.57	15.0
C22r-C23n	CP11, P8	49.71-51.74	49.87-51.5	735.93-740.49	729.41-739.96	2.25
C23r	CP10	51.74-52.36	51.5-52.8	741.35-743.21	740.79-742.31	3.00
C24n-2r	CP9b, P7	52.80-52.90	52.8-53.5	744.58-744.83	743-746.34	2.50
C24n-3n	CP9b, P6	52.90-53.35	52.8-53.5	744.83-745.93	743-746.34	2.44

Note: N = nannofossil, F = foraminifer datums.

Table T10. Paleomagnetic results from Hole 1068A used to determine the magnetostratigraphy at Site 1068. (**See table notes.** Continued on next page.)

Core, section, interval (cm)	Depth (mbsf)	NRM (A/m)	NRM Inc (°)	ChRM Inc (°)	χ (10^{-5} SI)	Q-ratio	MDF/T_b (mT/°C)	Polarity
173-1068A-								
1R-1, 51-53	711.81	1.36E–2	47.8	29.3	40.2	0.94	30	N
1R-1, 59-61	711.88	9.98E–4	58.9	67.2	22.2	0.13	15	N
1R-1, 76-78	712.06	2.55E–4	–26.4	–32.2	14.4	0.05	40	R
1R-2, 129-131	714.09	2.57E–4	–21.1	–20.3	15.4	0.05	20	R
1R-3, 19-21	714.49	3.24E–4	–14.7	–23.2	17.6	0.05	50	R
1R-4, 116-118	716.96	8.99E–5	10.2	–9.3	10.2	0.02	20	R?
1R-5, 103-105	718.33	1.23E–4	–14.0	–28.7	14.6	0.02	55	R
2R-1, 13-15	721.03	5.01E–4	28.6	64.5	22.5	0.06	15	N
2R-1, 23-25	721.13	1.44E–4	27.8	61.2	5.3	0.08	20	N
2R-1, 58-60	721.48	8.81E–5	36.1	34.9	16.8	0.01	40	N
2R-2, 74-76	723.14	6.88E–4	–34.6	–40.0	15.0	0.13	45	R
2R-3, 85-87	724.75	5.95E–5	24.2	19.1	16.8	0.01	10	N
2R-4, 72-74	726.12	7.70E–5	–13.0	–8.7	14.8	0.01	20	R?
2R-5, 38-40	727.28	4.83E–5	15.1	18.3	14.6	0.01	20	N
3R-2, 139-141	732.99	1.44E–4	44.1	47.0	19.4	0.02	(500)	N
3R-4, 12-14	734.72	1.11E–4	56.3	50.6	19.9	0.02	(500)	N
3R-5, 28-30	736.38	7.40E–5	25.8	9.4	20.4	0.01	30	N?
3R-6, 8-10	737.68	1.12E–3	35.8	31.7	22.9	0.14	(400)	N
3R-6, 87-89	738.47	1.01E–4	–3.7	–41.9	17.3	0.02	(300)	R
4R-1, 42-44	740.72	1.34E–4	41.9	33.1	19.9	0.02	(200)	N
4R-2, 12-14	741.92	1.68E–4	–73.0	–52.8	11.0	0.04	(300)	R
4R-3, 85-87	744.15	1.96E–4	67.9	55.7	16.6	0.03	(200)	N
4R-4, 95-97	745.75	7.63E–5	32.4	37.3	19.7	0.01	(300)	N
4R-6, 2-4	747.82	7.65E–5	51.5	22.7	21.7	0.01	(150)	N
4R-6, 69-71	748.49	1.36E–3	55.0	–27.0	32.5	0.12	(300)	R
5R-1, 47-49	750.37	1.21E–2	40.1	49.9	42.9	0.79	(400)	N
5R-2, 98-100	752.38	4.86E–2	76.3	72.6	40.6	3.34	(200)	N
5R-3, 25-27	753.15	2.43E–2	34.5	19.8	62.1	1.09	(200)	N
5R-5, 62-64	756.52	1.92E–2	44.0	33.9	43.7	1.23	(300)	N
5R-6, 64-66	757.54	1.05E–2	36.8	23.3	29.2	1.00	(200)	N
6R-1, 108-110	760.68	1.33E–5	35.6	40.7	32.8	0.001	20	N
6R-2, 126-128	762.36	4.76E–5	–25.8	–63.5	14.4	0.01	20	R
6R-3, 62-64	763.22	1.90E–4	49.2	19.4	12.6	0.04	25	N
6R-3, 108-110	763.68	2.41E–4	69.1	47.9	12.4	0.05	30	N
6R-4, 60-62	764.70	2.09E–2	35.6	42.5	58.6	0.99	20	N
6R-5, 32-34	765.92	1.69E–2	–7.0	–41.0	49.0	0.96	20	R
6R-6, 126-128	768.36	6.47E–4	13.1	–4.8	13.6	0.13	10	R?
6R-7, 36-38	768.96	5.25E–3	–6.4	19.0	25.6	0.51	(350)	N
7R-1, 34-36	769.64	8.59E–3	–20.0	–18.7	28.8	0.83	10	R
7R-2, 120-122	772.00	4.68E–2	4.8	–62.0	85.4	1.53	10	R
7R-3, 96-98	773.26	1.01E–2	34.2	35.6	27.8	1.01	10	N7
7R-18-20	773.98	8.91E–3	–16.1	–61.2	39.6	0.63	15	R
7R-4, 23-25	774.03	1.62E–2	–13.7	–15.2	26.8	1.69	10	R
7R-4, 32-34	774.12	5.26E–2	26.8	–12.3	55.6	2.64	10	R
7R-4, 51-53	774.31	3.01E–2	–11.0	–14.5	35.6	2.36	20	R
7R-4, 86-88	774.66	7.86E–2	74.2	65.2	572.7	0.38	25	N
7R-4, 124-126	775.04	6.05E–2	–8.0	–52.6	62.4	2.71	40	R
7R-5, 9-11	775.39	2.02E–2	–3.4	–31.0	47.6	1.18	50	R
7R-5, 64-66	775.94	7.35E–2	62.0	69.1	—	—		N
7R-5, 83-85	776.13	5.11E–2	–1.9	–8.1	63.6	2.24	15	R?
8R-1, 55-57	779.45	7.67E–2	46.1	35.5	122.8	1.74	(200)	N
8R-1, 108-110	779.98	9.54E–2	47.5	38.9	87.4	3.05	20	N
8R-2, 9-11	780.49	2.51E–2	–8.5	–30.2	71.0	0.99	(300)	R
8R-2, 19-21	780.59	4.66E–2	–4.7	–32.1	115.2	1.13	(300)	R
8R-2, 30-32	780.70	1.05E–1	–54.0	35.5	115.8	2.53	10	R
8R-2, 43-45	780.83	4.04E–2	–24.0	–43.0	98.4	1.15	10	R
8R-2, 72-74	781.12	9.34E–2	49.5	37.0	145.4	1.79	(400)	N
8R-2, 101-103	781.41	6.62E–2	–21.5	–22.6	67.4	2.74	(250)	R
8R-2, 143-145	781.83	3.05E–2	33.4	35.9	65.6	1.30	10	N
8R-3, 112-114	783.02	2.14E–2	79.4	–12.9	77.5	0.77	(400)	R
8R-4, 7-9	783.47	3.92E–2	62.3	–46.8	75.9	1.44	(550)	R
8R-5, 95-97	785.85	1.16E–3	74.2	–39.3	26.6	0.12	(400)	R
9R-2, 63-65	790.63	3.72E–4	–5.2	11.1	11.8	0.09	(250)	N
9R-3, 65-67	792.15	2.66E–4	23.6	43.8	13.4	0.06	(400)	N
9R-4, 49-51	793.49	3.20E–3	–32.1	–21.2	10.6	0.84	60	R

Table T10 (continued).

Core, section, interval (cm)	Depth (mbsf)	NRM (A/m)	NRM Inc (°)	ChRM Inc (°)	χ (10^{-5} SI)	Q-ratio	MDF/T_b (mT/°C)	Polarity
9R-5, 11-13	794.61	4.21E–4	–46.6	–65.4	10.4	0.11	60	R
9R-5, 53-55	795.03	9.81E–4	49.9	31.6	18.4	0.15	30	N
9R-5, 67-69	795.17	3.72E–4	88.0	73.8	10.6	0.10	25	N
9R-5, 87-89	795.37	7.02E–4	63.8	54.5	7.4	0.26	25	N
9R-6, 141-143	797.41	1.63E–4	–9.8	47.7	8.4	0.05	15	N
9R-7, 35-37	797.85	2.06E–4	19.3	26.8	8.8	0.07	20	N
10R-1, 40-42	798.50	5.25E–4	37.8	52.1	16.0	0.09	25	N
10R-1, 50-52	798.60	1.12E–3	58.3	59.4	10.4	0.30	40	N
10R-1, 71-73	798.81	2.16E–4	–12.7	–9.5	8.0	0.08	30	R?
10R-2, 27-29	799.87	1.91E–4	45.2	65.1	7.8	0.07	60	N
10R-2, 38-40	799.98	2.05E–4	63.3	47.9	8.0	0.07	15	N
10R-3, 79-81	801.89	1.67E–4	–16.9	–14.5	17.4	0.03	100	R

Notes: NRM = natural remanent magnetization intensity, NRM Inc = NRM inclination, ChRM Inc = characteristic or stable remanent magnetization inclination after demagnetization, χ = low-field magnetic susceptibility, Q-ratio = Koenigsberger ratio, MDF/T_b = median demagnetizing field/unblocking temperature. N = normal polarity, R = reversed polarity.

Table T11. Paleomagnetic and biostratigraphic datums in Hole 1068A.

Magnetic datum (chron or subchron)	Biostratigraphic datums (N, F)	Age (Ma)		Depth range (mbsf)		Sedimentation rate (m/m.y.)
		Magnetism	Biostratigraphy	Magnetism	Biostratigraphy	
C21n	CP12b	46.26-47.91	47.2-48.3	711.81-712.06	711.65-719.16	0.15
C21r	CP12a	47.91-49.04	48.5-49.7	712.06-719.18	719.55-751.11	6.30
C22n	CP12a	49.04-49.71	48.5-49.7	719.18-723.14	719.55-751.11	5.91
C22r-C23n	CP11, P9	49.71-51.74	49.8-51.5	723.14-762.36	751.75-762.93	0.52
C23r	CP10	51.74-52.36	51.5-52.8	762.36-763.22	763.81-766.82	1.39
C24n	CP9b	52.36-53.35	52.8-53.5	763.22-783.02	767.48-778.94	20.0
C24r	CP9a-CP8	53.35-55.90	53.7-56.2	783.02-794.61	779.20-796.28	4.55
C25n	CP8-CP7, P4	55.90-56.39	55.9-56.2	795.03-801.89	797.21-802.33	14.0

Note: N = nannofossil, F = foraminifer datums.

Table T12. Paleomagnetic results from Hole 1069A used to determine the magnetostratigraphy at Site 1069.

Core, section, interval (cm)	Depth (mbsf)	NRM (A/m)	NRM Inc (°)	ChRM Inc (°)	χ (10^{-5} SI)	Q-ratio	MDF/T_b (mT/°C)	Polarity
173-1069A-								
2R–2, 116-118	730.44	2.33E–3	42.9	30.5	18.6	0.35	(150)	N
2R-3, 22-24	731.00	8.34E–4	53.5	–3.0	14.0	0.17	(300)	N?
2R-3, 36-38	731.14	9.15E–4	62.7	63.0	18.2	0.04	70	N
2R-3, 40-42	731.19	8.88E–5	45.9	—				
2R-3, 47-49	732.25	1.39E–4	36.7	—				
3R-2, 66-68	740.26	6.42E–4	13.4	—				
3R-2, 73-75	740.33	6.70E–5	–55.3					
3R-2, 78-80	740.38	9.33E–5	26.3	–13.7	7.6	0.03	70	R
3R-3, 9-11	741.19	4.61E–4	43.6	–15.5	6.7	0.19	(500)	R
4R-2, 40-42	749.60	6.78E–4	58.4					
4R-2, 53-55	749.67	8.92E–5	–62.3					
7R-1, 12-14	776.92	3.52E–2	24.7	18.3	59.2	1.66	(300)N	N
7R-1, 23-25	777.03	1.77E–2	34.8	—	148.4	0.33		
7R-1, 45-47	777.25	3.99E–2	43.1	46.7	86.4	1.29	(200)	N
7R-1, 74-76	777.54	3.90E–2	42.1	—	37.0	2.94		
7R-1, 82-84	777.62	5.19E–2	44.0	57.4	37.4	3.87	(200)	N
7R-1, 100-102	777.80	2.67E–2	42.5	60.7	31.2	2.39	(200)	N
7R-1, 144-146	778.24	2.84E–2	55.8	48.0	38.2	2.07	(550)	N
7R-2, 19-21	778.49	2.30E–2	41.9	—	29.2	2.20		
7R-2, 29-31	778.59	2.58E–2	40.7	–40.9	50.0	1.44	(250)	R
7R-2, 95-97	779.25	3.13E–2	–44.6	–21.6	50.2	1.74	(200)	R
7R-3, 60-62	780.40	1.09E–2	–35.3	–45.4	32.4	0.94	(300)	R
7R-3, 76-78	780.56	5.79E–4	30.4	—	28.6	0.06		
7R-3, 79-81	780.59	8.58E–3	–21.7	–60.8	31.8	0.75	(100)	R
7R-3, 107-109	780.87	1.96E–2	–21.0	–50.3	28.2	1.94	(500)	R
8R-1, 110-112	787.51	9.28E–4	53.4	–23.0	20.4	0.13	(400)	R
8R-1, 136-138	787.76	3.37E–4	72.4	–58.2	22.0	0.04	(400)	R
9R-2, 5-7	797.54	1.02E–3	57.0	–33.0	30.2	0.09	(300)	R
9R-4, 59-61	801.09	4.86E–4	54.9	17.9	85.6	0.02	5	N

Notes: NRM = natural remanent magnetization intensity, NRM Inc = NRM inclination, ChRM Inc = characteristic or stable remanent magnetization inclination after demagnetization, χ = low-field magnetic susceptibility, Q-ratio = Koenigsberger ratio, MDF/T_b = median demagnetizing field/unblocking temperature. N = normal polarity, R = reversed polarity.

Table T13. Paleomagnetic and biostratigraphic datums in Hole 1069A.

Magnetic datum (chron or subchron)	Biostratigraphic datum (N, F)	Age (Ma)		Depth range (mbsf)		Sedimentation rates (m/m.y.)
		Magnetism	Biostratigraphy	Magnetism	Biostratigraphy	
C21n	CP12b	46.26-47.91	47.2-48.5	730.44-740.26	718.8-731.89	5.95
C21r	CP12a	47.91-49.04	48.5-49.7	740.3-749.6	740.80-759.19	8.23
C22n	CP12a	49.04-49.71	48.5-49.7	749.6-?	740.80-759.19	15.28
C22r-C23r	CP11-CP10	49.71-52.36	49.7-52.8	760-772*	759.42-772.05	4.53
C24n	CP9b	52.36-53.35	52.8-53.5	776.92-778.49	773.97-778.03	1.58
C24r	CP9a-CP8	53.35-55.90	53.7-56.2	778.59-797.04	778.27-784.58	7.24
C25n	CP8-CP7	55.90-56.39	55.0-57.0	801.09-?	784.6-786.7	14.33?

Notes: N = nannofossil, F = foraminifer datums. * = data from the pass-through measurements.

Table T14. Paleolatitudes for Iberian drilled sites.

Site	Age interval (Ma)	*N*	Paleolatitude	α_{95} (°)
897	0.78-2.58	62	28.2	4.6
898	0.78-1.95	86	27.0	4.4
900	0.99-8.06	14	25.1	12.3
1067	42.54-53.35	22	24.4	8.5
1068	46.26-56.39	71	23.8	5.1
1069	46.26-56.39	19	24.1	7.3

N = number of samples used in statistical analysis; α_{95} = radius of circle of 95% confidence about the mean inclination.

Table T15. Results of reversal tests using inclination-only statistics.

Site	Polarity	*N*	I	α_{95} (°)	k	*R*	λ_o	λ_c	f (1, *N* – 1) {0.975}
897	N	23	41.2	6.0	23.9	22.0774			~5.79
	R	39	50.5	5.8	16.7	36.7181			~5.45
	M	62	47.0	4.6	17.0	58.4128	13.5	8.9	~5.29
898	N	13	46.9	8.6	22.6	12.4668			~6.55
	R	73	45.3	4.9	13.4	67.6047			~5.26
	M	86	45.6	4.4	14.3	80.0712	1.2	11.6	~5.23
900	N	5	32.8	11.6	59.7	4.9329			~12.22
	R	9	49.1	18.3	9.1	8.1163			~7.57
	M	14	43.1	12.3	10.9	12.8093	22.7	24.2	~6.41
1067	N	17	40.0	12.9	8.0	15.0055			~6.12
	R	5	–34.9	22.3	16.5	4.7576			~12.22
	M	22	38.9	10.3	9.3	19.7414	6.8	25.8	~5.83
1068	N	43	41.6	6.2	12.8	39.7291			~5.41
	R	28	–34.4	7.8	11.9	25.7377			~5.63
	M	71	38.8	5.1	12.1	65.1913	10.8	10.0	~5.27
1069	N	8	42.9	19.2	9.6	7.2712			~8.07
	R	11	–36.6	13.5	12.0	10.1632			~6.94
	M	19	39.3	7.3	20.1	17.3847	8.8	21.8	~5.98

Notes: N = normal, R = reversed, M = both N and R. *N* = number of samples exhibiting the ChRM inclinations and used in statistical analysis, I = estimated mean inclination using the method of McFadden and Reid (1982), α_{95} = radius of circle of 95% confidence about the mean inclination, k = Fisher (1953) precision parameter for the mean inclination, *R* = length of resultant vector. λ_o = observed and λ_c = critical (at the 95% confidence level) angles between the normal and reversed mean inclinations (McFadden and McElhinny, 1990). f (1, N – 1) {0.975} = critical value of the F distribution with 1 and (*N* – 1) degrees of freedom and with probability = 0.025. If $\lambda_o > \lambda_c$, then the hypothesis of a common mean direction may be rejected at the 95% confidence level. Otherwise, the reversal test is considered to be positive.